Master's thesis

NTNU
Norwegian University of Science and Technology
Faculty of Natural Sciences
Department of Biology

Thea Johanna Aandstad Hettasch

Effect of Calibration Data Subsetting on Boolean Model Calibration and Drug Synergy Predictions

Master's thesis in Biotechnology
Supervisor: Åsmund Flobak
Co-supervisor: Martin Kuiper, Eirini Tsirvouli
May 2023

NTNU
Norwegian University of
Science and Technology

Thea Johanna Aandstad Hettasch

Effect of Calibration Data Subsetting on Boolean Model Calibration and Drug Synergy Predictions

Master's thesis in Biotechnology
Supervisor: Åsmund Flobak
Co-supervisor: Martin Kuiper, Eirini Tsirvouli
May 2023

Norwegian University of Science and Technology
Faculty of Natural Sciences
Department of Biology

NTNU
Norwegian University of
Science and Technology

Sammendrag

Kreft er et samlebegrep for en rekke sykdomstilstander som kjennetegnes av unormal og ukontrollert celledeling, og forårsakes av avvikende regulering av ulike cellulære signalveier knyttet til cellevekst og celledød. Med Boolske nettverksmodeller kan en gi både en strukturell og dynamisk fremstilling av kreftsystemet på molekylnivå, samt at de kan tilpasses slik, at de gjengir den molekylære profilen og behandlingsresponsen som er observert i en spesifikk kreftcellelinje eller kreftpasient.

Formålet med dette prosjektet var å identifisere en strategi som bedrer evnen en Boolsk nettverksmodell har til både å representere den molekylære profilen til en kreftcelle og gjengi kreftcellens respons til kombinasjoner av medikamenter med synergistisk effekt. Forskningsgruppen NTNU DrugLogics har utviklet en *pipeline* som inkluderer en programvaremodul for kalibrasjon av Boolske nettverksmodeller. Et *kalibrasjonsdatasett* gis som input, og beskriver en måltilstand som den kalibrerte versjonen av inputmodellen skal gjengi. Hypotesen, som dette prosjektet bygger på, antar at det kun er måltilstanden til et *driversett* med noder som er nødvendig å inkludere i kalibrasjonsdatasettet for å oppnå en kalibrert modell som gjenspeiler den fullstendige måltilstanden, da tilstanden til et driversett av noder er bestemmende for tilstanden til hele den Boolske nettverksmodellen.

Denne driver-orienterte kalibrasjonsstrategien ble i dette prosjektet anvendt på tre Boolske kreftmodeller, men synes ikke å garantere de kalibrerte modellenes evne til å gjenspeile den molekylære profilen til en cellelinje. Resultatene indikerer at visse topologiske begrensninger, forårsaket av ulikheter i topologisk fleksibilitet, forhindrer modellene i å oppnå en tilstand som er i overenstemmelse med måltilstanden.

Pipelinen inneholder også en programvaremodul for *in silico* prediksjon av synergistiske medikamentkombinasjoner. De kalibrerte modellene ble gitt som input til modulen for å undersøke hvordan den driver-orienterte kalibrasjonsstrategien påvirker modellenes evne til å riktig kunne gjengi hvilke kombinasjoner av kreftmedikamenter som har en synergistisk effekt og ikke. Strategien bedrer prediksjonsytelsen til én av de tre Boolske kreftmodellene. Økt prediksjonsytelse er ikke observert hos de resterende to modellene, og indikerer at modellenes nettverkstopologi ikke gjengir den synergistiske responsen til kombinasjonene av medikamenter som er observert i cellelinjene. Større topologiske endringer må gjøres i disse modellene, utover det som er mulig med den anvendte kalibrasjonsmetoden, hvis en skal bedre prediksjonsytelsen.

Abstract

Cancer is a condition characterised by abnormal and uncontrolled proliferation of cells, caused by a complex disease system, involving the dysregulation of a variety cellular signalling pathways. A Boolean modelling framework is able to give both a structural and dynamical representation of a cancer system, and can be adapted to represent the specific molecular profile and treatment response observed in a cancer cell line or patient.

In this project, a strategy for improved computational calibration of Boolean cancer models and subsequent drug synergy predictions was investigated. Such a strategy could improve the construction of cell line specific – or even personalised – Boolean cancer models, as well as the identification of drug synergies for effective treatment of cancer.

The DrugLogics pipeline includes a software module for ensemble-wise calibration of Boolean models, through the modification of logical rule. One of the pipeline's main inputs is a *calibration dataset* specifying an experimentally observed target state which guides model calibration. It is hypothesised, that including the target state for a *driver set* of nodes should be sufficient to obtain a calibrated model ensemble reflecting the target state, as a driver set of nodes is thought to determine the stable state of a Boolean model.

This driver-based calibration strategy was applied for cell line specific calibration of one Boolean cancer model, representing the AGS cell line, and two Boolean cancer models representing Colorectal Cancer (CRC), with the goal of obtaining a set of calibrated models representing the baseline activity of a selection of cell lines. The strategy did not ensure calibrated model ensembles with stable states compliant with the target state, as some stable state heterogeneity was observed across all calibrated models. The ability to reach an overall baseline compliant state seems to be restricted by topological limitations in the input Boolean models, caused by canalising logical functions and differences in topological flexibility.

The DrugLogics pipeline further includes a software module for *in silico* combinatorial drug perturbation simulations. All calibrated model ensembles were further given as input to the synergy prediction module, in order to assess the ability to correctly predict a set of experimentally verified gold standard synergies. A driver-based calibration strategy did improve the predictive performance of the AGS model, but could not be generalised across the CRC models.

Acknowledgements

This master's thesis in biotechnology was conducted at the Department of Biology, Norwegian University of Science and Technology (NTNU), in the period January 2022 to May 2023.

The work was done in collaboration with the DrugLogics Initiative and aimed to investigate how calibration datasets should be constructed, in order to improve Boolean model calibration and drug synergy predictions, using the DrugLogics pipeline.

I want to thank my main supervisor, Åsmund Flobak, for his valuable encouragement and scientific guidance. I also want to thank my co-supervisors, Martin Kuiper and Eirini Tsirvouli, for always providing their scientific view, and helping me navigate the challenges I have faced during my project. Thank you for guiding me in the right direction, and at the same time giving me enough freedom to explore and develop my own scientific route.

Last, but not least, I want to thank my friends and family for their support and motivation. Thank you for filling my life outside the study hall with laughter, music, good conversations and fond memories.

Thea Johanna Aandstad Hettasch
Trondheim, May 2023

Contents

List of Figures

List of Tables

Abbreviations

AUC Area Under the Curve.

CRC Colorectal Cancer.

DP Determinative Power.

FN False Negatives.

FP False Positives.

FVS Feedback Vertex Set.

GA Genetic Algorithm.

HSA Highest Single Agent.

IQR Interquartile Range.

MI Mutual Information.

RCL Random Chance Line.

ROC Receiver Operating Characteristic.

STG State Transition Graph.

TN True Negatives.

TP True Positives.

Chapter 1

Introduction

1.1 Systems Biology

Systems biology is both a conceptual understanding and a methodological approach to biological investigation.

The theoretical concept of systems biology builds on the understanding that biological entities, such as cells or organisms, are complex systems of interacting parts, and that the behaviour of such a system is caused by *emergent properties* that arise from the complex interplay between all system components. The development of systems biology as a scientific field constitutes a paradigmatic shift, from a reductionist to a more holistic approach to biological inquiry. In a systems view, a cell is not a mere collection of genes, proteins, and metabolites, and cannot be fully understood by simply listing up all these components. The phenotype of the cell is caused by a complex interplay between different hierarchical levels of interaction, where genes, proteins, metabolites, the cell's own phenotype, as well as the phenotype of neighbouring cells, control and constrain each other [73].

This conceptual understanding of biology is accompanied by a set of methodological principles, integrating technological tools, mathematics, computer science and experimental examination. The methodological paradigm of systems biology can be summarised by four steps [58]:

(1) *Measuring biological components*: All relevant biological components included in a biological system have to be identified and measured. Advances in high throughput technologies enable us to measure the amount of DNA, RNA, proteins and metabolites in a cell and its environment - so called *omics data*.

(2) *Reconstruction of networks*: The underlying interaction network, has to be reconstructed, from prior knowledge and experimental observations of the *in vivo* system. This provides a static representation of the complex interplay between all components in the system.

(3) *Mathematical modelling*: Advances in computer science and information technology provide tools for representing interaction networks in a mathematical format, as well as converting them to computational models. Such models will be more than a static representation of the components and interactions, and would make it possible to describe system dynamics and how the represented system develops over time under various conditions.

(4) *Hypothesis-driven discovery*: The mathematical model-representation of a biological system constitutes a central step in an iterative hypothesis-driven cycle, comparing model predictions and experimental observations. Such a model would represent the current understanding of the system under investigation. New hypotheses about the behaviour of the system can be tested by introducing perturbations to the model, and the validity of the predicted behaviour can be further experimentally verified in the lab.

1.2 Representing Biological Systems as Networks

Building network models that represent biological systems is a central part of the systems biology methodology.

Common for all biological networks is that biological entities are represented as *nodes*, and interactions between entities are represented as *edges*. Edges can be directional, to indicate how the information propagates through the network, and can be assigned as either positive or negative, to represent the activating or inhibitory effect of one entity on another [4]. In addition to nodes representing biomolecules, like genes and proteins, output nodes representing possible phenotypic outcomes are also included, to enable an interpretation of the global behaviour of the model [4]. Network models provide a way of visualising the system under investigation, as well as a way of representing the available information about system structure, using a format that can be further analysed both mathematically and computationally.

Networks are not only applied in biology, they are also used to represent social interactions between people, transportation systems, and power grids. Even though the nodes and edges comprising these networks represent very different things, these networks share some common organisational principles. An important consequence of this common organisation is the ability to apply general graph theoretical principles to analyse all these different networks [11]. This provides us with a tool box of mathematical and statistical concepts which we can use to identify essential network characteristics.

1.2.1 Static Network Measures Describe Network and Node Characteristics

Graph theoretical concepts can be applied to define the general structure of a network, unravel complex relationships between network components, and highlight network nodes

with certain characteristics.

Characterising Individual Nodes

Individual nodes in a network can be ranked based on certain centrality measures, such as *degree centrality* (number of edges), *closeness centrality* (the average shortest path length from one node to all other nodes in the network) and *betweenness centrality* (to what extent is a node located on the shortest path between all possible pairs of nodes in a network) [25, 61]. Centrality measures can be considered individually or in combination, to identify key nodes that act as central interaction points or communicators in the network. In a biological sense, highly ranked nodes – based on centrality – might represent key regulators of gene expression or signal amplification [78].

Characterising Dense Neighbourhoods

Graph theoretical analyses can and should extend beyond the characterisation of individual nodes, as nodes form local neighbourhoods. Hartwell et al. actually argues that biological systems are inherently modular and not nodular, as cellular functions are carried out by groups and not individual components [32]. The *clustering coefficient* is used to identify dense local neighbourhoods in a network [11]. The clustering coefficient of a node i is calculated as the number of edges connecting the first neighbours of i, divided by the possible number of edges between the first neighbours of i [61]. If the neighbours of i form a closely connected neighbourhood, then i has a high clustering coefficient. A *clique* is a group of nodes where all nodes are connected to each other and has the highest possible clustering coefficient of 1.

Characterising the whole network

In addition to graph measures describing nodes or local node neighbourhoods, there are measures used to describe the network as a whole.

One example is the *degree distribution* of a network. This measure is related to node degree, but instead of only looking at the degree of an individual node, the distribution of possible degree values in the network is considered [25]. The degree distribution can be represented as a histogram or a dot plot with node degree values on the x-axis and the number of nodes having a degree k on the y-axis. Most cellular networks are *scale-free*, characterised by a power-law degree distribution with a negative exponent (λ) (Eq. 1.1) [11].

$$P(k) = k^{-\lambda} \tag{1.1}$$

The scale-freeness of these networks indicates that there is no "typical" node with a typical average degree. In a scale-free network there are a large number of low-degree nodes connected to a few highly connected hubs [11].

The *clustering coefficient distribution* is a different measure, used to characterise whole networks. In addition to being scale-free, most cellular networks show hierarchical modularity, where highly interconnected modules are regulated by sparsely distributed hubs [5]. In the clustering coefficient distribution, this is recognised by high degree hubs having a low clustering coefficient, and low degree nodes having a high clustering coefficient. If this is the case, then the clustering coefficient distribution will follow a power law with a negative exponent (β) . (Eq. 1.2).

$$C(k) = k^{-\beta} \tag{1.2}$$

Due to the universality of graph theory, we are able to measure and quantify different network properties at different levels of the network – from individual nodes, to local neighbourhoods and the network as a whole. In a biological context, these measures can be used to identifying important hub nodes representing biologically crucial proteins and genes, or identifying node clusters representing protein complexes or tightly regulated genes. However, these static measures do not provide any information on how the system reacts to perturbations or other dynamic changes. At this stage, it is a static picture of the system we are investigating, and to enable any dynamic simulations we need extend from a static network representation to a dynamic model.

1.3 Dynamic Modelling of Biological Networks

The purpose of dynamic modelling of a network is to investigate how a system develops over time or how it reacts to different types of perturbations. It adds a dynamic layer to the static network representation of a biological system.

Modelling the dynamics of a network can be done using either a *continuous* or a *discrete* approach. Continuous dynamic modelling requires information about specific parameters – like reaction rates and initial concentrations of reactants – to be able to correctly represent the temporal dynamics of all biomolecular reactions. Measuring or estimating these parameters can be challenging and time consuming. Hence, continuous dynamical modelling is usually applied for modelling smaller systems with a sufficient amount of available kinetic data [4].

When modelling larger systems, a discrete and parameter-free dynamic modelling approach is preferred, enabling a dynamic representation of the system without the need of any kinetic data [79]. An example of such an approach is the *logical modelling* framework. In a logical model, each node is associated with a value representing the activity, or the relative concentration, of the entity the node represents. In addition to being associated with an activity value, each node is associated with a logical rule describing how the activity of the node is affected by the activity of its upstream regulators [1]. Even though the discrete system representation applied in the logical modelling framework is an approximation of the *in vivo* system, it has been successfully used to represent and

model large complex biological systems, such as the activation and differentiation of T lymphocytes and cell cycle control [1].

1.3.1 Boolean Modelling

Boolean modelling is a special case of logical modelling, where all network entities are assigned a binary value representing its activity (active = 1, inactive = 0). This binary state classification is of course an approximation, but it is in accordance with how biologists usually talk about genes being expressed or not, or signalling pathways being active or suppressed [3]. Furthermore, in continuous dynamic modelling, gene regulation is modelled by the Hill function, which can be approximated by a dichotomous step-function, which also supports a binary interpretation [67].

As for general logical models, every node in a Boolean model is associated with a logical rule, or a logical update function, determining how the activity of the network node changes over the course of a series of time steps, based on the activity of its regulators. Logical rules are expressed using the logical operators OR, AND an NOT in various combinations [4]. For instance, if node C is activated by node A, and inactivated by node B, the logical rule associated with node C would be:

$C = A \ AND \ NOT \ B.$

After each discrete time step (t = 1, 2, 3, 4, ..., n) the state of each node in the network is updated according to the logical rules. Over time, the state of the model will stabilise in a certain *attractor*, which can be either a single *stable state* of a set of reoccurring states (*complex attractor*) [4].

1.3.2 Attractor Calculation

The long term behaviour of a logical model is represented by an attractor state. Starting from an initial state, the model transitions from one state to another according to the logical transition rules, and after some time, the model will stabilise in an attractor state, which represents the long-term behaviour of the system [79]. The transition dynamics of a model can be represented by a *State Transition Graph (STG)*, where nodes represent model states, and edges represent possible transitions between states [4]. In some cases, the system will end up in a single stable state, where all node states remain unchanged after updating the system according to the logical rules. In other cases, the system will reach a complex attractor where the system oscillated among a certain set of states. In the STG a stable state will be represented by a state node without any outgoing edges, and a complex attractor is recognised as a closed node cycle [1].

The structure of the STG is determined by the chosen updating scheme [4]. There are two main updating schemes, the *synchronous* one and the *asynchronous* one. When applying the synchronous updating scheme, all model components are updated simultaneously, and each model state has only one possible successor state. However, in real biological

systems, changes in the state of system components happen at different time points, which the synchronous scheme is not able to represent. When following the asynchronous updating scheme, on the other hand, each node is updated individually, and each model state has several successor states. The order in which the nodes are updated can be either random or guided by knowledge about the relative timescale observed for activation or regulation of system components [4].

The attractor identified using either the synchronous or the asynchronous updating scheme usually represents a cellular phenotype. Taking a closer look at the activity of each node defined in the attractor can reveal some of the cellular mechanisms driving the phenotypic outcome, and measuring attractor changes due to component knock-outs or knock-ins can determine critical system components, and how the system reacts to perturbations [4].

1.4 Driver Nodes Control the Dynamics of a Network Model

Network control has become a hot topic in the field of biological network modelling, as it reflects the desire to not only understand the dynamics of a system, but also to control and predict its outcome [82]. Network control of logical models involves finding and applying a control strategy that will steer the temporal dynamics of the model into a desired attractor. It is usually not necessary to control all nodes in a logical network model to drive the system into a target state, as the dynamics of a complex network model is determined by a subset of *driver nodes* [46]. It is sufficient to steer each node in the driver set to its target state for the whole model to reach the target attractor [34].

Different measures have been proposed to identify network nodes that constitute a set of driver nodes. Simple static graph measures, such as the aforementioned degree centrality and closeness centrality, as well as variations or combinations of these measures, have been used to identify driver nodes [45]. Some measures used to identify driver nodes also take into account model features specific for a certain modelling approach. An example is the measure called *Determinative Power*, which is used to identify driver nodes in Boolean models, by taking into account the logical rules of the nodes [81].

1.5 The Heterogeneous Nature of Cancer

The term "cancer" covers a variety of different diseases, with some common characteristics, such as uncontrolled cell growth and invasion of healthy tissue [31]. These hallmarks are caused by dysregulation of signalling pathways related to cell division, cell growth, and cell death, involving a variety of different biomolecules.

Cancerous cells and tissue develop from genetically altered cells in the body of a patient. Genetic alterations due to inherited defects, or mutations caused by exposure to carcinogens, cause an accumulation of genetic damage [64]. The accumulation of such genetic

damage can reduce the ability of a cell to respond to external signals. If this unresponsiveness causes an increase in cell division, then the cell will replicate uncontrollably and develop into a mass of malignant cells [14].

Not all genetic mutations cause cells to develop into cancer. There are two main groups of genes, which are related to cancer development, namely the *oncogenes* and the *tumour suppressor genes* [14]. *Proto-oncogenes* – which are the normal versions of the cancer causing oncogenes – encode proteins which promote cell division. Proto-oncogenes become cancer driving oncogenes when so-called *gain-of-function* mutations cause an increase in activation. Tumour suppressor genes, on the other hand, encode proteins which inhibit cell replication and division. The loss of tumour suppressor genes, due to *loss-of-function* mutations, are also related to an increased risk of cancer [64].

The development of cancer can happen in different areas of the body, and cancers are usually classified by the tissue where the tumour arises. Even though different types of cancer show similar phenotypic properties – including hallmarks like sustained proliferative signalling, evasion of growth suppressors, and resistance to cell death – individual cancer types rarely share the same genetic mutations [57]. Genetic differences are observed across patients with the same type of cancer, and there are even significant intercellular variations between cells in the same tumour [31]. The heterogeneous nature of cancer poses a challenge to the development of effective cancer treatment, as one kind of treatment will not necessarily be effective for all patients or cancer sub-types.

1.6 Precision Cancer Medicine

Tailoring treatment to individual cancer patients goes under the notion of *precision cancer medicine* and is thought to be a necessary approach to improve the treatment of cancer [57]. This paradigmatic change in cancer therapy is characterised by a shift from a tumour-type centred to a gene centred focus. Cancer patients have usually been classified based on the type of tumour and the tissue-specific location of the cancer cells. However, due to major advances in high throughput technologies and systems medicine approaches, researchers and clinicians are able to look deeper into the genetic and proteomic profile of each individual patient, and use this knowledge to apply more specific treatment. This shift coincides with the development of targeted therapies directed at specific molecular targets [37]. Examples of successful targeted therapies are trastuzumab in patients with *HER2*-positive breast cancer and vemurafenib and dabrafenib in patients with advanced-stage melanoma with *BRAF*-mutations [53].

Developing a patient specific treatment involves analysing the genetic and proteomic information of the tumour, and selecting a drug or a combination of drugs that will target the patient's genetic or proteomic alterations, which cause the disease [57]. We are developing from a one-size-fits-all cytotoxic chemotherapy approach to a more specific approach targeting specific genes which drive cancer development [2]. Understanding

the variation of driver mutations between patient subgroups and individuals will lead us towards a more personalised treatment of cancer.

1.7 Drug Synergies

Several genes or pathways are usually altered in a cancer cell. Hence, in terms of treatment, it might be more effective to target more than one gene to increase the therapeutic effect. Drug combinations which have an overall larger effect than the sum of the effects of each drug independently, are considered *synergistic* drug combinations [44]. The advantage of using synergistic drug combinations in cancer treatment is that one can lower the drug dosage, while still maintaining the same therapeutic effect. The rationale for wanting to reduce the drug dosage is that it could avoid the toxic side effects of the drug treatment, and minimise the development of drug resistance [44].

Experimental identification and validation of synergistic drug combinations has some limitations. First, it is limited by the combinatorial explosion of possible drug combinations that have to be tested. Secondly, the molecular mechanisms causing the synergistic effects are not easily characterised [15]. Network-based modelling approaches offer a promising framework for synergy prediction, as they are able to overcome these limitations. The computational efficiency accelerates the analysis, and the underlying biomolecular network structure is able to reveal possible synergy mechanisms [15]. Hence, network-based synergy prediction can be used to identify the most promising drug combinations and guide further experimental validation.

1.8 Project Aim and Motivation

The motivation behind this project has been to contribute to the improvement of Boolean model calibration and *in silico* prediction of cell line specific drug synergies, using Boolean cancer models and the NTNU DrugLogics pipeline.

Two main functionalities are executed by the DrugLogics pipeline: *model calibration* and *drug synergy predictions*. The aim of model calibration is to modify the logical rules of a Boolean cancer model to obtain a calibrated model with a stable state, matching the observed baseline state of a cancer cell. The calibrated model is further used to predict synergistic combinations of targeted cancer drugs.

The experimentally observed baseline state of the cancer cell, which serves as an objective for model calibration, is defined in the input *calibration dataset*. The overall aim of this project was to investigate how the content of this calibration dataset affects initial model calibration and subsequent synergy predictions. The hope was to identify a principle which could guide calibration dataset construction, and thereby improve model performance.

1.9 Main Objective

The main objective of this work has been to investigate if Boolean model calibration – using the DrugLogics pipeline – can be improved, and if it would result in better drug synergy predictions through selection of specific subsets of calibration data. It has been hypothesised, that including the cell line specific baseline activity for a *driver set* of nodes in the calibration dataset, will ensure a calibrated model reflecting both the experimentally verified baseline activity and synergistic drug response observed in a cell line.

From network theory we know that some nodes drive the dynamics of a network model, and are able to control the target stable state of the model. Hence, if a model is calibrated with respect to the baseline activity of such a driver set, the calibrated model will be driven towards a baseline-compliant stable state. A calibrated model with a baseline-compliant stable state reflects the baseline activity of the cancer cell, and should also reflect how the cancer cell responds to drugs. Hence, such a baseline-compliant model should also be able to correctly predict synergistic drug combinations.

Three node measures, *degree Z-score*, *Determinative Power* and a *near-minimal Feedback Vertex Set*, are used to identify possible driver sets of nodes in three different Boolean cancer models. Calibration datasets, including cell line specific baseline data, are constructed based on these node measures, and provided as input for model calibration and synergy predictions.

Resulting analyses focus on two main questions:

- *Effect of calibration data subsetting on calibrated model stable state:* Does a calibration dataset, including the baseline activity of a driver set of nodes, ensure a calibrated model, whose stable state reflects the baseline activity of the cell line?
- *Effect of calibration data subsetting on synergy predictions:* Does a calibration dataset, including the baseline activity of a driver set of nodes, ensure a calibrated model, which is able to correctly predict cell line specific drug synergies?

Chapter 2

Materials and Methods

2.1 Workflow

The following steps of model and data retrieval, calibration dataset construction, and pipeline output analysis, were performed to investigate if calibration of a Boolean cancer model – with respect to a driver set of nodes – improves the ability to correctly represent a cell line specific baseline state, and make cell line specific synergy predictions.

- Identification of Boolean cancer models from the literature
- Collection of cell line specific baseline activity profiles and gold standard synergies from experimental data
- Identification of possible driver sets of nodes based on degree Z-score, DP, and a near-minimal FVS
- Construction of calibration datasets based on driver sets
- Running DrugLogics pipeline simulations with driver-based calibration datasets
- Investigating the effect of a driver-based calibration strategy on stable state of calibrated models
- Investigating the effect of a driver-based calibration strategy on synergy predictions

2.2 Code and Data Availability

All scripts and necessary files to reproduce the analyses of this project, are provided in a GitHub repository: `https://github.com/theahettasch/calibration_data_subsetting`. The pipeline input and output data was processed an visualised using R 3.6.3 and RStudio Version 2022.02.0+443.

Three R Markdown files are included in the GitHub repository and provide the following scripts:

- *calibration_dataset_construction.Rmd*: Calculation of degree Z-score and DP, construction of calibration datasets, and bash-file construction
- *stable_state_analysis.Rmd*: Visualisation of stable states in heatmaps and calculation of baseline compliance
- *predictive_performance_analysis.Rmd*: AUC ROC calculation and visualisation in boxplots

2.3 The NTNU DrugLogics Pipeline

The NTNU DrugLogics pipeline served as the core tool in this project. The pipeline includes four software modules: *Aomics*, *Atopo*, *Gitsbe* and *Drabme* (Figure 2.1). The research conducted in this report only involves the application of Gitsbe and Drabme modules. Gitsbe and Drabme execute two of the main pipeline functionalities: Boolean model calibration and combinatorial perturbation experiments. In this project these modules have been applied to calibrate Boolean cancer models to cell line specific baseline data and perform drug synergy predictions.

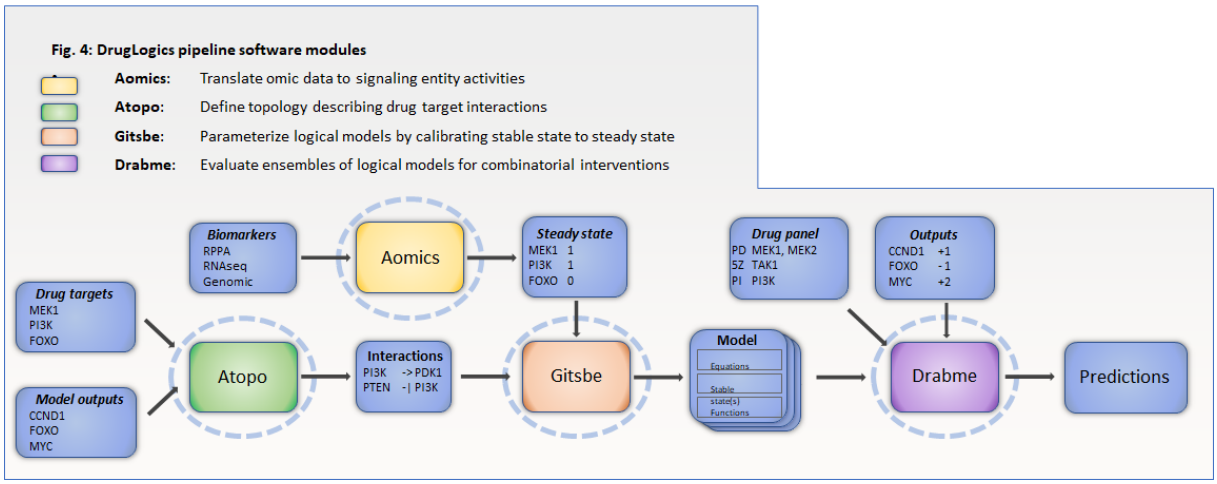

Figure 2.1. An overview of the DrugLogics pipeline including four different software modules: Aomics, Atopo, Gitsbe and Drabme. The figure is retrieved from the website of the DrugLogics initiative `https://druglogics.eu/projects/colosys/`

2.3.1 Model Calibration with Gitsbe

The aim of model calibration with Gitsbe is to obtain a model that is able to reflect a desired behaviour, such as an experimentally observed state or an experimentally observed response to perturbations. A Genetic Algorithm (GA) is applied to parameterise the topology or the logical rules of a Boolean network model, and thereby improve the compliance between model behaviour and the experimentally observed behaviour.

GA is considered a machine learning strategy, and is able to identify optimal solutions

in a large search space by modifying certain structures or parameters [26]. The approach is called a *genetic* algorithm, because it is based on how genetic material is combined between individuals during evolution, to increase the fitness of the offspring [18]. A parent generation of data structures or *chromosomes* is selected, and the parent generation's ability to solve a specific problem – *the fitness* – is calculated. Those structures with the highest fitness are selected for crossover, meaning that their features are combined into new offspring structures. In addition to the crossover, mutations are introduced to the new offspring generation. These mutations are usually introduced by inverting some of the chromosome features [38], hence, chromosome features should be binary, having two possible outcomes. The fitness of the offspring generation is calculated and a new crossover and mutation procedure is performed [38]. This will eventually lead to a set of data structures with high fitness and an optimal ability so solve a specific target problem.

The input of the Gitsbe module is a Boolean input model and a target state, defined in a *calibration dataset*. Based on the input model, a first generation of Boolean models is generated by introducing a number of random mutations to the logical rules of the model. A fitness score is calculated for each model based on the resemblance between the stable state of the model and the target state defined in the calibration dataset. A high fitness score means that the stable state reached by the Boolean model corresponds to the target state. Based on this fitness score, a set of the best performing models are selected for the next generation. Logical equations are exchanged between the best performing models, and new mutations are introduced to the logical rules before fitness calculation and model selection is repeated. The model calibration process is halted when a defined fitness threshold, or a defined upper number of generations, is reached. The output of the Gitsbe module is an ensemble of the top performing models based on fitness. All top performing models are described in a model summary file where model fitness values, model stable states and the logical rules of the parameterised models are defined.

In this project, the Gitsbe module was applied to calibrate a set of Boolean cancer models, representing gastric and colorectal cancer, to reflect the observed baseline activity of genes and proteins in a selection of gastric and colorectal cancer cell lines. Calibrated model ensembles were further used as input for prediction of cell line specific synergies with Drabme.

2.3.2 Synergy Predictions with Drabme

The main functionality of the Drabme module is to perform combinatorial perturbation simulations on calibrated models generated by Gitsbe. In this project, the functionality of Drabme is used to predict synergistic drug combinations in gastric and colorectal cancer cell lines. Given a panel of drugs and their molecular targets, the drug response is simulated for both single drug and drug combination perturbations. Based on simulated drug responses, drug synergies are identified.

Drabme provides both model-wise and ensemble-wise outputs. As the name suggests,

the model-wise output provides synergy results for each individual Gitsbe model, while the ensemble-wise output provides synergy results averaged across the model ensemble. Synergy prediction results are provided as *response excess* values for each drug combination tested. The response excess value indicates the response difference between the additive and the combination effect of each drug combination across the model ensemble, given a certain synergy calculation method (HSA or Bliss). Ensemble-wise synergy predictions were considered the main outputs in this project and were compared against cell line specific and experimentally verified gold standard synergies, to assess the predictive performance of the calibrated models.

Synergy calculation methods

Different methodologies have been proposed to assess and determine the synergistic effect of a drug combination. These methodologies differ in the way they determine the additive effect, and provide different ways of calculating the Combination Index (CI), which indicates a combination effect greater than (CI >1), lesser than (CI <1) or similar to (CI = 1) the expected additive effect [23].

Bliss Independence: According to the Bliss Independence model a drug combination is considered a synergy if the combination effect (E_{AB}) is larger than the additive effect given by the common formula for probabilistic independence:

$$E_A + E_B(1 - E_A) = E_A + E_B - E_A E_B$$

The CI can be calculated as:

$$CI = \frac{E_A + E_B - E_A E_B}{E_{AB}}$$

Highest Single Agent (HSA): According to HSA, a drug combination is considered a synergy if the combination effect (E_{AB}) is larger than the maximal effect of each drug individually: max(E_A, E_B).

The CI is calculated using the following formula:

$$CI = \frac{max(E_A, E_B)}{E_{AB}}$$

The threshold for considering a drug combination as synergistic is usually lower when using HSA compared to Bliss (Figure 2.2).

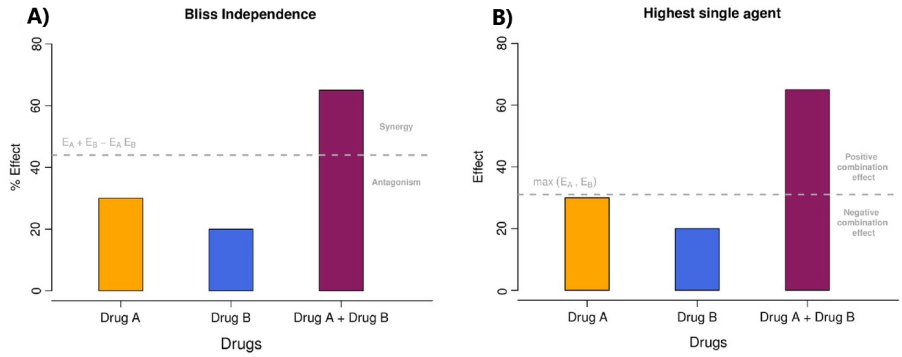

Figure 2.2. Illustration of two different synergy calculation methods. A) Bliss Independence and B) Highest Single Agent. $E_A = 30$, $E_B = 20$ and $E_{AB} = 65$. Adapted from Foucquier J, Guedj M. Analysis of drug combinations: current methodological landscape. Pharmacol Res Perspect. 2015 Jun;3(3):e00149. doi: 10.1002/prp2.149.

2.3.3 Pipeline Configurations

The pipeline configuration file includes global, Gitsbe-specific, and Drabme-specific parameter specifications. Configuration parameters were specified to perform analyses supporting the project objective. During model calibration with Gitsbe, only *balance* mutations, changing the link operators (AND, OR), were allowed, to avoid large topological changes to the models.

The BioLQM tool was applied for calculation of model stable states [54].

The synergy calculation method was set to either *HSA* or *Bliss* depending on the synergy calculation method applied in the *in vitro* synergy screens used to provide gold standard synergies. A complete list of all configuration parameters is provided in Appendix A.

2.4 Model and Data Collection

Three Boolean cancer models were retrieved from literature to serve as input models for model calibration and synergy prediction analyses. In addition, cell line specific baseline activity profiles and gold standard synergies were collected.

2.4.1 Model Selection, Modification, and Characterisation

A Boolean model, named CASCADE 1.0, representing the AGS cell line of gastric cancer, was retrieved from Flobak et al. [20]. In addition, two Boolean models representing Colorectal Cancer (CRC) were obtained from Lu et al. and Park et al. respectively [47,60].

Some model modifications were performed for the models to fit some common requirements. Firstly, all models should be self-contained to avoid the need to set any initial input conditions [20]. Secondly, the analysis was restricted to models mainly including nodes representing intracellular components in cancer related pathways. Hence, addi-

tional extracellular nodes were removed. The removal of nodes could have great impact on model dynamics, hence, each node removal was followed by a stable state calculation with Gitsbe. If no stable state was reached after node removal, the node was retained. Finally, all models should include two common output nodes representing *antisurvival* and *prosurvival* to obtain a common way of interpreting drug response. The combined antisurvival and prosurvival response is interpreted as a certain level of cell growth and is defined as the *global output* of a model and serves as a way of calculating the model response to perturbations. All nearest neighbours inhibiting the antisurvival node or activating the prosurvival node increase the level of growth (+1) and all nearest neighbours inhibiting the prosurvival node or activating the antisurvival node decrease the level of growth (-1). In the case of only one nearest neighbour, the second nearest neighbours were considered. Adding all values together gives a multi-levelled global growth output.

To assess the effect of model modifications on the network structure, the *degree distribution* and *average clustering coefficient distribution* was inspected statistically and graphically, both before and after model modifications, using the NetworkAnalyzer tool in Cytoscape (v.9.7) [69]. Large changes in degree- and clustering coefficient distribution would suggest that the original structure of the network was scrambled due to the applied model modifications.

2.4.2 Selection of Cell Lines

This project aimed to enhance cell line specific model calibration and synergy predictions. Since CASCADE 1.0 is an AGS cell line specific model, AGS was the only cell line used to calibrate CASCADE 1.0. The Lu- and Park-models, on the other hand, are specific for the CRC cancer type, allowing testing across different CRC cell lines. Information about the selection of cell lines used to perform cell line specific analyses is found in table 2.1.

Table 2.1. Overview of all gastric and CRC cell lines applied in this project. The origin of the sample is also provided.

Cell line	Disease	Sample origin
AGS	Gastric carcinoma	Stomach
COLO_205	Colorectal cancer	Derived from metastatic site: ascitic fluid
HCT_116	Colorectal cancer	Large intestine
SW_48	Colorectal cancer	Large intestine
SW_620	Colorectal cancer	Derived from metastatic site: lymph nodes

2.4.3 Cell Line Specific Baseline Activity Profiles

Baseline activity profiles were created for all cell lines and describes the experimentally observed activity of genes and proteins in the cell line. These profiles were further filtered for genes and proteins included in the selected Boolean models.

A binary baseline activity profile for the AGS cell line was retrieved from Niederdorfer et al. [56]. A subset of the AGS baseline activity profile had previously been collected from literature, by Flobak et al. [20]. Niederdorfer et al. completed the profile from cell line copy number variations and gene expression data data, using the pathway inference algorithm PARADIGM [77]. The AGS baseline activity profile was filtered for nodes included in the CASCADE 1.0 model.

For the CRC cell lines, baseline activity profiles were obtained by normalising gene expression data measurements. A gene expression dataset (*rnaseq_fpkm_20191101.csv*) was downloaded from the Sanger Cell Model Passport portal [74]. The dataset was filtered for the selected CRC cell lines, and expression values for all genes included in the Boolean CRC models were retrieved. All genes in the expression dataset are identified by their HGNC symbol [65], hence, a translation file was constructed for each Boolean model, mapping the name of each node to the corresponding HGNC symbol. All translation files are provided in the GitHub repository: *translation_files*.

For each CRC cell line, gene expression values for all model specific genes, were normalised using the normalisation section of the PROFILE framework [12]. All normalised gene expression values were subsequently binarised to fit the binary nature of the Boolean model framework. Normalised values below 0.5 were considered as 0 and normalised values above 0.5 were considered as 1. All normalised expression values equal to 0.5 were not binarised, due to their ambiguity.

2.4.4 Cell Line Specific Gold Standard Synergies

Cell line specific synergies from *in vitro* experiments were identified and used as gold standards against *in silico* predictions. Cell line specific gold standard synergies, for the AGS cell line, were obtained from Flobak et al. [20]. For the selected CRC cell lines, gold standard synergies were retrieved from a synergy screen performed by Jaaks et al. [35].

Jaaks et al. provide synergy data for breast, colon and pancreatic cancer, so the data was filtered for the four project relevant CRC cell lines. In addition, only synergies involving drugs targeting genes included in the applied CRC Boolean models were selected. Drugs with multiple targets were included if at least one target corresponded to a model node.

In the synergy screen performed by Jaaks et al., they use an *anchored* approach where one drug is considered the anchor drug, and the other one is considered the library drug [35]. For each combination, the anchor drug is tested at two fixed concentrations, while the library drug is tested at 7 different concentrations. Due to this screening method, each drug combination is tested twice, with drug A acting as the anchor drug in one screen, and drug B in the other. However, when doing synergy predictions using the DrugLogics pipeline, it is not possible to distinguish between these two combination orders. Hence, as long as one combination order was reported as synergistic in the screen, it was added as a gold standard synergy for comparison against *in silico* predictions.

2.5 Calculation of Degree Z-score, Determinative Power, and a Near-minimal Feedback Vertex Set

Degree Z-score, Determinative Power (DP) and a near-minimal Feedback Vertex Set (FVS) are all suggested as a possible basis for identification of driver sets of nodes in network models [55, 81]. In this project, these measures were used to identify possible driver sets guiding the construction of calibration datasets from cell line specific baseline activity profiles. Degree Z-score and DP was calculated for all nodes included in the Boolean models. In addition, a near-minimal FVS was identified for each Boolean model.

2.5.1 Calculation of Degree Z-score

Degree Z-score is a variation of the degree centrality measure which gives the absolute number of interactions with neighbouring nodes. The degree Z-score, on the other hand, provides the number of interactions relative to the average degree of all network nodes [81]. To calculate the degree Z-score of a node i (Z_i), the average degree of all network nodes ($\overline{k}$) is subtracted from the degree of node i (k_i) and divided by the standard deviation of node degrees in the network(σ) (Equation 2.1).

$$Z_i = \frac{k_i - \overline{k}}{\sigma} \tag{2.1}$$

The degree Z-score was calculated for all model nodes using an R-script provided by Weidner et al. [81]. The only necessary input is a text file including all logical rules included in the Boolean model. The script for calculating Z-score is provided in this R Markdown file: *Script for calculating Z-score*

2.5.2 Calculation of Determinative Power

Determinative Power (DP) is a measure used to identify driver nodes in logical models and is dependent on the logical rules of the model nodes [81]. A high DP indicates that the knowledge about the state of a node i yields a high level of information about the state of its output nodes [62].

Following the definition presented in Pentzien et al. [62], the sum of the information gained from knowing the state of node j, over all output nodes of nodes j, also called the DP of node j, is calculated as follows:

$$DP(j) = \sum_{i=1}^{n} MI(f_i(X); (X_j) \tag{2.2}$$

Mutual Information (MI) is a measure of the information gained about the state of all output nodes X = {X_1, X_2 ..., X_n}, given the logical equation of node X_i (f_i) and the

knowledge about the state of X_j. The calculation of DP is illustrated using an example from Pentzien et al. [62] in Appendix B.

The DP was calculated for all model nodes adapting an R-script provided by Weidner et al. [81]. The only necessary input is a text file including all logical rules included in the model. The script for calculating DP is provided in this R Markdown file: *Script for calculating DP*.

2.5.3 Identification of a Near-minimal Feedback Vertex Set

A *Feedback Vertex Set* (FVS) is a subset of network nodes including one node in each network cycle [55]. Fixing the state of a node in each cycle will cause acyclic behaviour and drive the network to a target state defined by the nodes in the FVS, as the ability to reach a variety of stable states is caused by the presence of cycles.

A minimal FVS is the smallest possible FVS in a network and is not necessarily a unique subset. Newby et al. provide a python code for identifying subsets of a near-minimal FVS given a network in *graphml* format and a specified subset size [55]. A near-minimal FVS was identified for all three Boolean cancer models, using the Newby et al. script.

Each network model was converted into a *graphml* format, and given as input to the `FindBestSubsets()` function. To identify the complete minimal FVS, the subset size (`numNodes`) was set to 1 and all one-node FVS subsets combined were considered a complete near-minimal FVS.

2.6 Calibration Dataset Construction

Possible driver sets identified based on Z-score, DP and a near-minimal FVS were used to construct calibration datasets from cell line specific baseline activity profiles. In addition, a collection of random sample calibration datasets were constructed as comparison against guided construction. A script for calibration dataset construction is provided in the following R Markdown file: *Script for calibration dataset construction*.

All calibration dataset are constructed using the format illustrated in Figure 2.3. This format can be used to defined model calibration both with respect to an experimentally observed target state (Figure 2.3b) and an experimentally observed perturbation response (Figure 2.3a).

In this project, Boolean cancer models were calibrated to reflect an unperturbed cell line specific cancerous state. The driver set or random sample of baseline data was defined as the target *Response*. The empty *Condition* translates to an unperturbed model, and the *Weight* indicates, that this is the only condition-response pair that has to be considered during model calibration and fitness calculation.

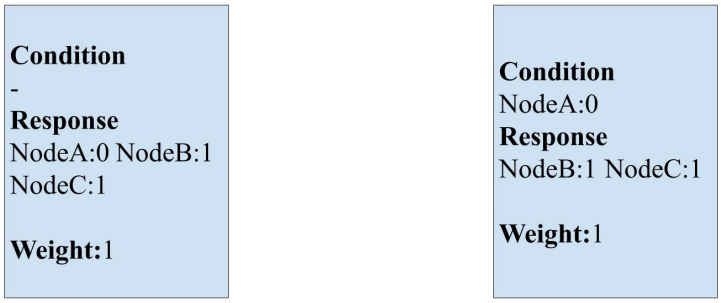

(a) Unperturbed target state.

(b) Perturbed response

Figure 2.3. Example of calibration dataset format. The ***Condition*** *defines if the model is perturbed or unperturbed and an experimentally observed target state is defined as a* ***Response****. In the case of several condition-response pairs, the* ***Weight*** *is used to calculate the weighted average fitness of a model across the selection of condition-response pairs. (a) Calibration data defining unperturbed target state. Translated to: Unperturbed model reaches stable state with NodeA inactive, NodeB active and NodeC active. (b) Calibration data defining perturbed response. Translates to: Knockout of NodeA gives a response state with NodeB active and NodeC active.*

2.6.1 Calibration Dataset Construction Guided by Z-score, DP, and a Near-minimal FVS

A collection of calibration datasets, including possible driver sets, were constructed based on Z-score, DP, and a near-minimal FVS. A near-minimal FVS constitutes a single possible driver set, hence the baseline activity of the near-minimal FVS was included in a single calibration dataset. Since Z-score and DP are continuous measures, several possible driver sets were selected and included in the collection of calibration datasets. All network nodes were subsequently ranked based on DP and Z-score, and the baseline activity for the top ∼10%, ∼20%, ∼30%, ..., ∼100% of all nodes were selected and included in 10 respective calibration datasets.

2.6.2 Random Sample Calibration Dataset Construction

A variety of random sample calibration datasets were constructed by randomly selecting a subset of data from the cell line specific baseline activity profiles.

First, the cell line specific baseline activity profile was imported as a dataframe in R. Random samples, of varying sample size (∼10, ∼20, ... ∼100%), were drawn from the baseline profile, using the `sample()` function. For each sample size, 20 random sample replicates were drawn. Every random sample was included in an individual calibration dataset.

2.7 Automation of DrugLogics Pipeline Simulations

All driver-based and random calibration datasets were sequentially given as input to the DrugLogics pipeline.

To automate the process of running the DrugLogics pipeline with different calibration datasets, bash scripts were created to initiate simulations and change the input calibration dataset between each run. Bash is the standard shell program for UNIX-based operating systems, such as Linux and Ubuntu. A bash script can be initiated from the terminal, and will execute all commands in the script [24]. A script for constructing bash-scripts i provided in this R Markdown file: *Script for constructing bash-scripts*.

A dedicated server was used to run the large number of sequential pipeline simulations. All necessary files for launching the pipeline, including bash scripts, were imported to the dedicated server and executed.

2.8 Stable State Analysis of Calibrated Models

The stable state of calibrated models were investigated in terms of visual inspection of stable state *consistency* and calculation of baseline *compliance*. Stable state consistency indicates to what extent all calibrated models in the ensemble reach the same stable state. The baseline compliance, on the other hand, indicates to what extent the stable state of the calibrated model is consistent with the state defined in the baseline activity profile. The following R Markdown file provides a script for stable state analyses: *stable_state_analysis.Rmd*.

2.8.1 Stable State Heatmaps

Stable state heatmaps were constructed to visually inspect the stable state homogeneity across one or several calibrated model ensembles.

A common ensemble-wise heatmap was constructed for all models calibrated to different possible Z-score or DP based driver-sets of baseline activity data. The stable state of each model, in the model ensemble, was extracted using the `get_stable_state_from_models_dir()` function from the *emba* (V0.1.8) R package. The average stable state across each calibrated ensemble was calculated and visualised together in a single heatmap.

A toy example is provided in Figure 2.4. Each column corresponds to the average stable state of a model ensemble calibrated to possible driver set and each row corresponds to the stable state activity of a certain model node. A graded colour scheme between blue (0) and red (1) indicates the average stable state activity of a node. A column with only blue and red cells indicates a consistent stable state across the ensemble, as is the case for the latter two columns in the figure. A row annotation indicating the baseline activity of each node was added as comparison against stable states. Hierarchical clustering – using

Euclidean distance as the distance metric – was applied to the heatmap row, grouping nodes with similar stable state activity.

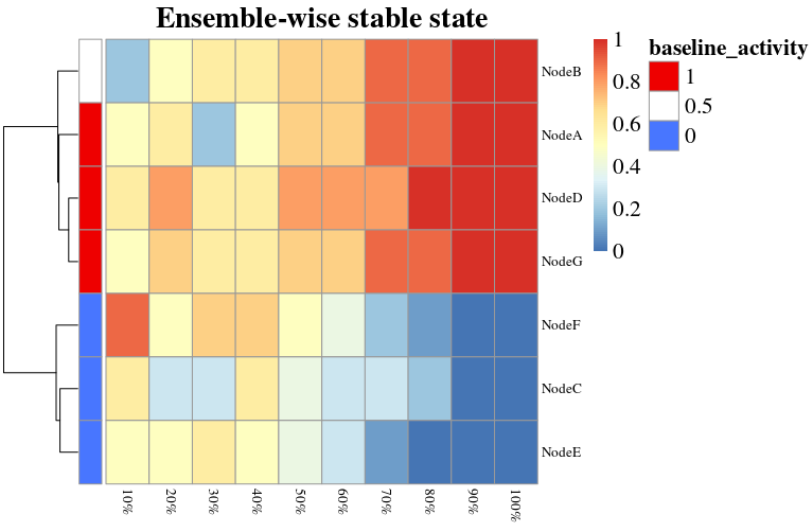

Figure 2.4. Toy example of an ensemble-wise, visually representing the stable state across models calibrated to possible driver sets. Each column corresponds to the average stable state of a calibrated model ensemble and each row represents the stable state activity of each node. Graded colouring from 0 (blue) to 1 (red) is applied and an annotation row with baseline activity is added.

Model-wise stable state heatmaps were constructed to visually inspect the stable state of models calibrated to a single driver set, based on a near-minimal FVS. The stable state of each model, in the model ensemble, was extracted using the `get_stable_state_from_models_dir()` function from the *emba* (V0.1.8) R package and visualised in a heatmap.

A toy example is provided in Figure 2.4. Each column corresponds to the stable state of a model in the model ensemble, and each row corresponds to the activity of a certain node. The baseline activity was added as an annotation row to the heatmap. Hierarchical clustering, using Euclidean distance as the distance metric, was applied to both rows and columns, grouping similar models and nodes together. If all models have the same stable state, then the stable state of the model ensemble is considered consistent, as in Figure 2.5b.

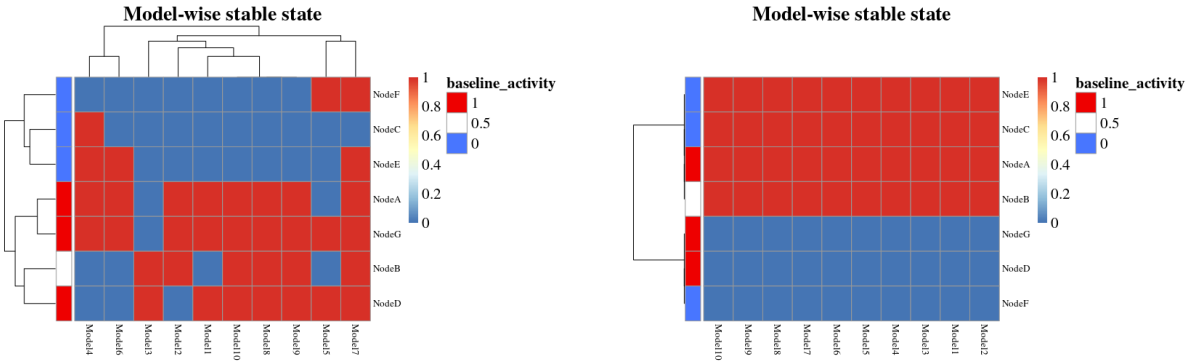

(a) Inconsistent stable states across model ensemble.

(b) Consistent stable state across model ensemble

Figure 2.5. Toy example of a model-wise stable state heatmap. Every column corresponds to the stable state of a single model in a model ensemble, and every row corresponds to the activity of a node

2.8.2 Compliance Between Stable State and Baseline Activity Profile

The similarity between the average stable state of a calibrated model ensemble and the baseline activity profile was assessed in terms of *compliance*.

For every node X_{ij}, where i is the number of nodes and j is the number of models in the ensemble, the average node activity across the model ensemble ($\overline{X_i}$) was calculated (eq. 2.3).

$$\overline{X_i} = \frac{\Sigma_{n=1}^{j} X_{in}}{j} \tag{2.3}$$

The absolute value of the difference between every average node value $\overline{X_i} = \{\overline{X_1}, \overline{X_2}, ..., \overline{X_i}\}$ and the node value defined in the baseline activity profile $G_i = \{G_1, G_2, ..., G_i\}$ was further calculated (eq. 2.4).

$$Y_i = |G_i - \overline{X_i}| \tag{2.4}$$

Finally, the compliance of a model ensemble was obtained by finding the average difference between the model ensemble and the baseline activity profile (eq. 2.5).

$$compliance = \frac{\Sigma_{n=1}^{i} Y_n}{i} \tag{2.5}$$

Compliance was calculated for all model ensembles calibrated to a possible driver set.

2.9 Synergy Prediction Analysis of Calibrated Models

The ability to correctly predict a set of cell line specific gold standard synergies was assessed for all calibrated models in terms of the Area Under the Curve (AUC) of the Receiver Operating Characteristic (ROC) curve. An R Markdown file is provided with necessary code for analysis of predictive performance:

predictive_performance_analysis.Rmd.

2.9.1 AUC ROC

AUC ROC is a performance metric for binary classification approaches [13]. Identifying drug combinations as either synergistic or non-synergistic is considered a binary classification problem. Hence, AUC ROC is applicable for assessing the ability of a calibrated model to correctly predict synergistic drug combinations.

Drabme provides an ensemble-wise response excess output for each drug combination. In this list of response excess values, there is no absolute decision boundary between which drug combinations are classified as synergies and non-synergies. The response excess value is a continuous measure, and synergy classification is dependent on the threshold we set as the decision boundary. The validity of the drug synergy prediction is compared to a set of experimentally confirmed gold standard synergies. Given the gold standard, the synergy classification output can be divided into four different categories: True Positives (TP), True Negatives (TN), False Positives (FP), and False Negatives (FN). The ROC curve is a graphical representation of the trade-off between the *True Positive Rate* (TPR), which translates to the test sensitivity (the ability to recognise true positives), and the *False Positive Rate* (FPR), which translated to 1 - test specificity (the probability of classifying false positives), across different classification measure thresholds [42] (eq. 2.6, 2.7).

$$\text{TPR (test sensitivity)} = \frac{TP}{TP + FN} \tag{2.6}$$

$$\text{FPR (1 - test specificity)} = \frac{FP}{FP + TN} \tag{2.7}$$

AUC is a way of quantifying the performance of the binary classifier given the ROC curve (Figure 2.6). AUC = 1 is the upper performance limit, and indicates that no FN or FP classifications are made by the classifier (Figure 2.6b). The diagonal line going from the coordinates (0,0) to (1,1) in the ROC plot, is called the Random Chance Line (RCL) [13]. If predictive performance follows this line, the AUC ROC value is equal to 0.5 and performance is no better than pure chance.

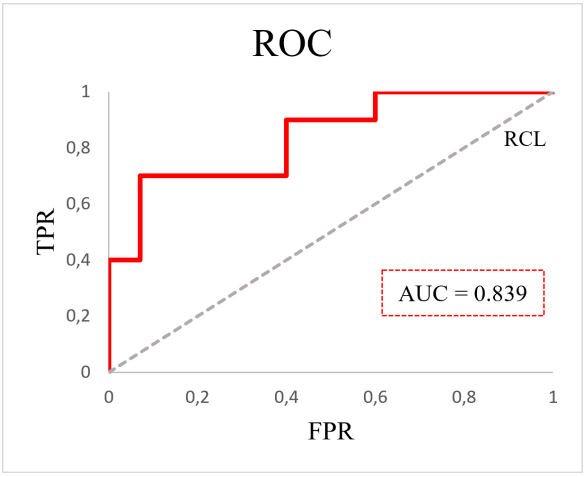

(a) ROC curve with AUC = 0.839

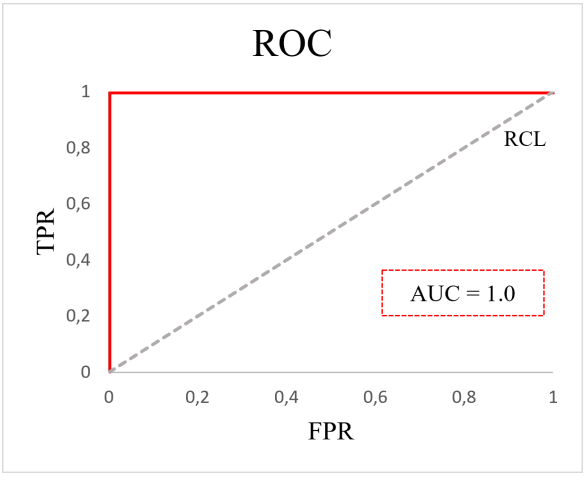

(b) ROC curve with AUC = 1

Figure 2.6. Illustration of ROC curve as a graphical representation of the trade off between the TPR and the FPR. The dashed line indicates the random chance line (RCL). A ROC curve above the RCL is considered better than random.

AUC ROC calculations were performed in R implementing the `get_roc_stats()` function from the *usefun* (V0.4.8) R package [83, 84].

2.9.2 Adjusting Synergy Predictions to Augment the Effect of Calibration Data

The topology of the input Boolean model alone carries some information about the dynamic response to perturbations [21]. Hence, some synergies can be predicted by an uncalibrated model. To augment the effect of model calibration on synergy predictions, the drug response of the calibrated model is normalised to the drug response of an uncalibrated model:

$$AUC_{normalised} = AUC_{calibrated} - AUC_{uncalibrated}$$

Drug combinations that are reported as more synergistic by the calibrated model – compared to the uncalibrated one – are considered as cell line specific synergies. It is reported, that this normalisation strategy was able to improve synergy predictions for the AGS cell line with CASCADE 1.0 [21]. For the Park- and Lu-models, this normalisation strategy will amplify the effect of calibration data as the same Boolean input model is used to predict synergies for different cell lines.

The normalisation strategy was implemented as a step in the calculation of AUC ROC. The normalised AUC ROC was calculated for each calibrated model and used in further analyses of predictive performance.

2.9.3 Visualisation of Predictive Performance in Boxplots

The predictive performance of models calibrated to random samples of baseline data was visualised in boxplots with jitter. The AUC ROC of each calibrated model was plotted against the size of the random sample included in the calibration dataset. This random sample boxplot served as a basis for comparison against the predictive performance obtained with driver-based calibration. The distribution of predictive performance associated with each random sample size is described in a boxplot by an *Interquartile Range* (IQR) and an upper and lower whisker (Figure 2.7).

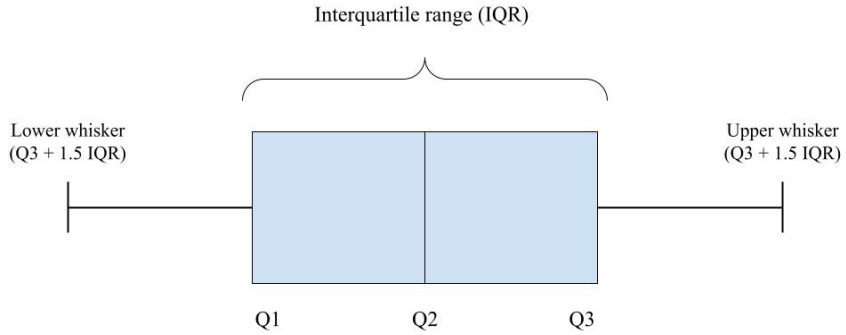

Figure 2.7. Illustration of a boxplot where the interquartile range (IQR) and the upper and lower whiskers are indicated.

The AUC ROC values of all calibrated models obtained by driver-based calibration were added as data points to the random sample boxplots. All driver-based calibrated models, having an AUC ROC value above the interquartile range of the random sample results, were considered an improvement of predictive performance.

Chapter 3

Results and Discussion

3.1 Modification and Characterisation of Boolean Cancer Models

Three Boolean cancer models were retrieved from the literature, and applied as input models for model calibration and synergy predictions with the DrugLogics pipeline. A summary of the selected Boolean models is given in table 3.1. All network interaction files and logical rules are provided in the GitHub repository: *model data*

Table 3.1. Summary of Boolean cancer models used in project analyses.

Model name	**Cancer system represented by model**	**Source**
CASCADE 1.0	AGS cell line, gastric cancer	Flobak et al. [20]
Park-model	Colorectal cancer	Park et al. [60]
Lu-model	Colitis associated colorectal cancer	Lu et al. [47]

Model modifications were performed to ensure that the models fulfilled some common criteria. Input nodes were removed to avoid the need for any input specifications, only intracellular model components involved in cancer signalling pathways were retained, and two nodes representing prosurvival and antisurvival were considered the main model outputs. The degree- and average clustering coefficient distribution was calculated before and after model modifications, in order to characterise the change in scale-freeness and hierarchical structure. Both a scale-free and a hierarchical structure is recognised by a degree- and average clustering coefficient distribution, following a power-law with a negative exponent.

CASCADE 1.0 already fulfills all model requirements. It is self-contained without any input nodes, includes nodes representing intracellular biomolecules related to cancer, and has two output nodes representing prosurvival and antisurvival (Figure 3.1). Hence, no model modifications were performed on CASCADE 1.0.

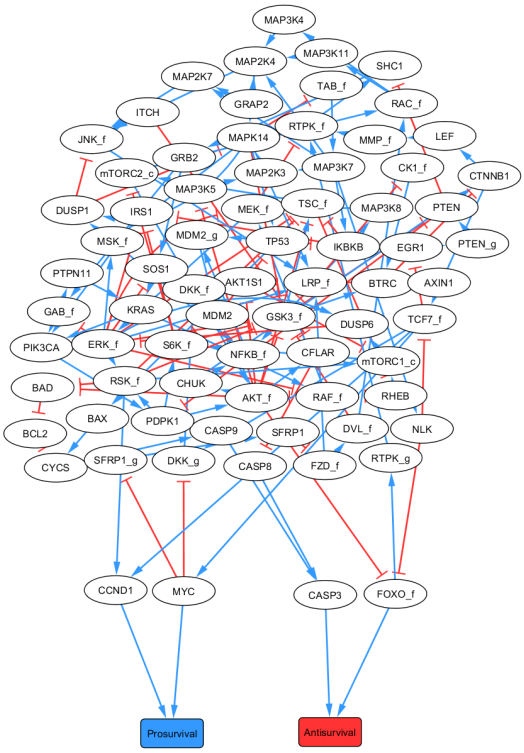

Figure 3.1. Graphical representation of the CASCADE 1.0 model, with 77 nodes and 149 directed edges. Square nodes represent the phenotypic outputs Antisurvival and Prosurvival. Red arrows represent inhibiting interactions, while blue arrows represent activating interactions.

A power-law was fitted to the degree distribution of CASCADE 1.0 with the following equation: $P(k) = 156.71k^{-2.089}, R^2 = 0.917$(Figure 3.2). The negative exponent of the power-law and the R^2 value being close to 1, suggests that CASCADE 1.0 is scale-free.

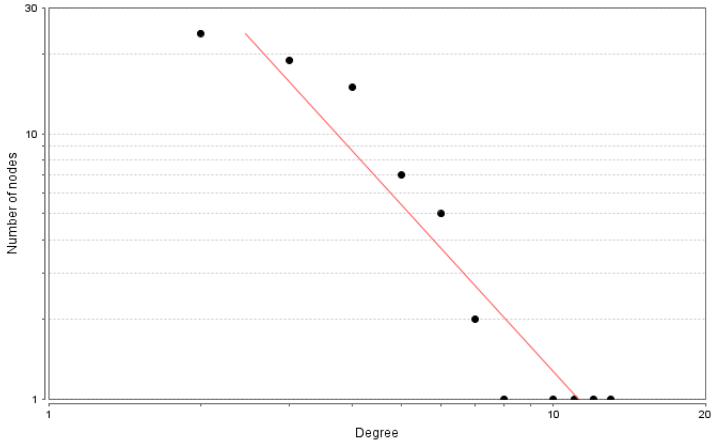

Figure 3.2. Degree distribution of CASCADE 1.0 on a log log scale. A power-law (red line) is fitted with the following equation: $P(k) = 156.71k^{-2.089}$, $R^2 = 0.917$.

A power-law was fitted to the average clustering coefficient distribution of CASCADE 1.0 with the following equation: $C(k) = 0.046k^{0.151}, R^2 = 0.012$. Based both on visual

inspection of the plot and the R^2 value, the relationship between degree and clustering average clustering coefficient does not seem to follow a power-law.

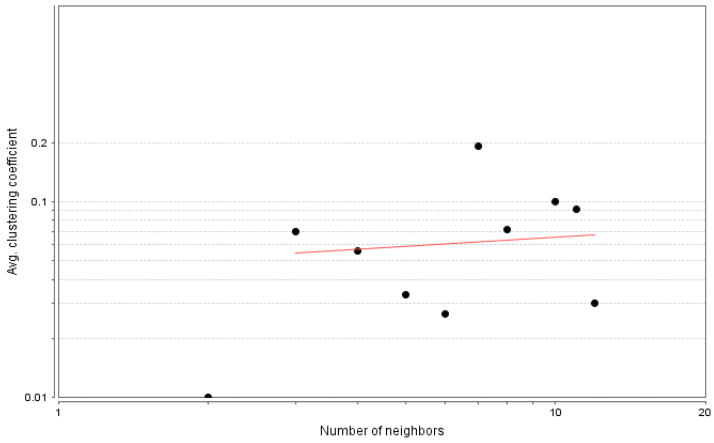

Figure 3.3. Average clustering coefficient distribution of CASCADE 1.0 on a log log scale. A power-law (red line) is fitted with the following equation: $C(k) = 0.046k^{0.151}, R^2 = 0.012$

.

Some model modifications were performed on the Park-model. It mainly includes components representing the intracellular signalling network of CRC. However, four input nodes representing extracellular signalling molecules are included and were removed from the model. In addition, the phenotypic output nodes named *Apoptosis* and *Proliferation* were substituted by the output nodes Antisurvival and Prosurvival (Figure 3.4).

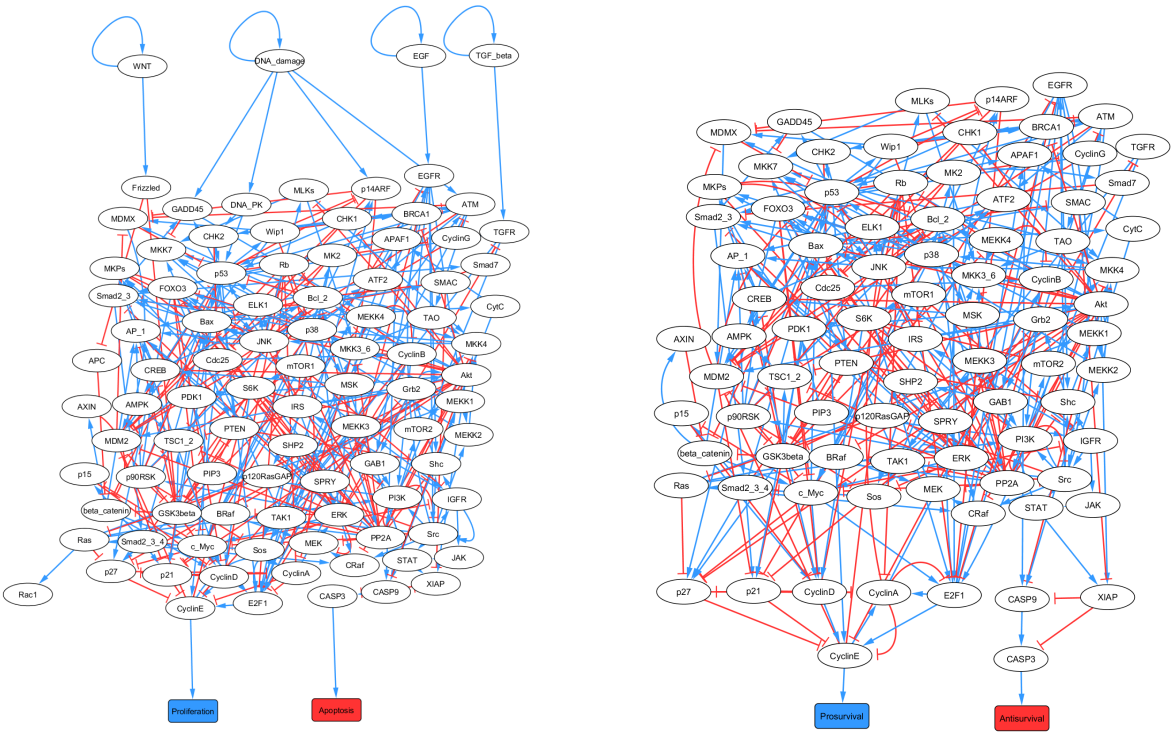

(a) Park-model before model modifications including 97 nodes and 343 directed edges.

(b) Park-model after model modifications including 91 nodes and 326 directed edges.

Figure 3.4. Park-model (a) before and (b) after model modifications. Square nodes represent the phenotypic outputs Antisurvival and Prosurvival. Red arrows represent inhibiting interactions, while blue arrows represent activating interactions.

A power-law was fitted to the degree distribution of the original and modified Park-model with the following equations:

Original model: $P(k) = 14.33k^{-0.697}, R^2 = 0.388$

Modified model: $P(k) = 14.385k^{-0.674}, R^2 = 0.414$

Only minor differences are observed between the fitted power-law of the degree distribution of the original and modified Park-models. The R^2 values indicate a poor fit and do not suggest a scale-free behaviour for the original nor the modified version of the Park-model. However, if the degree distribution plots are inspected visually, the poor fit seems to be caused by an underrepresentation of low-degree nodes (Figure 3.5). The graphical representation of the degree distribution indicates a scale-free behaviour, but the fitted power-law is offset by some outliers.

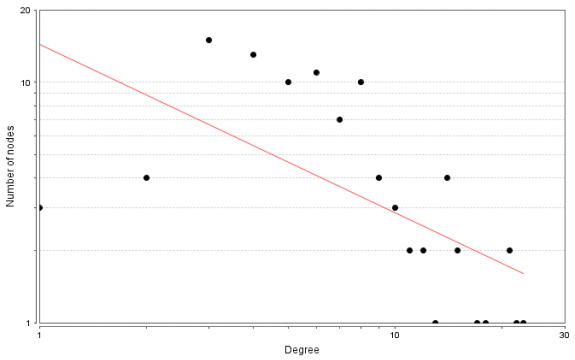

(a) Degree distribution of Park-model before model modifications. A power-law (red line) is fitted with the following equation: (a) $P(k) = 14.33k^{-0.697}$, $R^2 = 0.388$

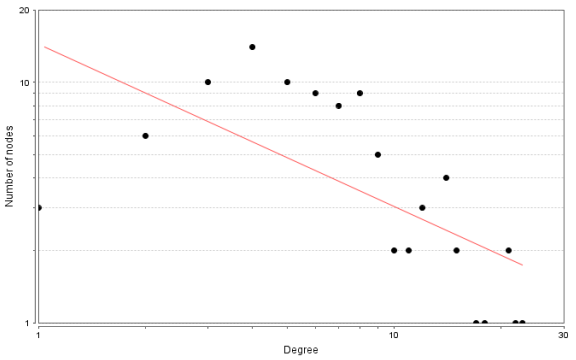

(b) Degree distribution of Park-model after model modifications. A power-law (red line) is fitted with the following equation: $P(k) = 14.385k^{-0.674}$, $R^2 = 0.414$

Figure 3.5. The degree distribution of the (a) original and the (b) modified version of the Park-model on a log log scale.

A power-law was fitted to the average clustering coefficient distribution of the original and modified Park-model with the following equations (Figure 3.6):

Original model: $C(k) = 0.356k^{-0.268}, R^2 = 0.329$

Modified model: $C(k) = 0.439k^{-0.341}, R^2 = 0.424$

The power-law equation does suggest a negative relationship between the node degree and the average clustering coefficient, indicating a possible hierarchical structure. However, the R^2 values do not indicate a perfect fit.

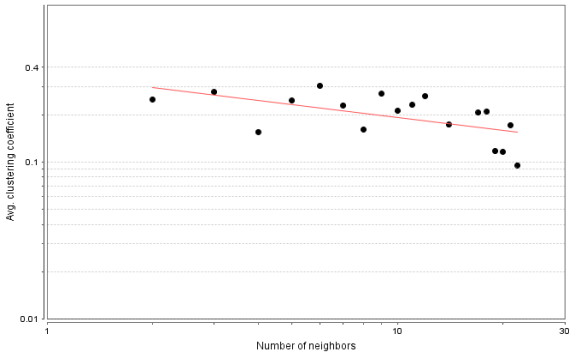

(a) Average clustering coefficient distribution of Park-model before model modifications. A power-law (red line) is fitted with the following equation: $C(k) = 0.356k^{-0.268}, R^2 = 0.329$

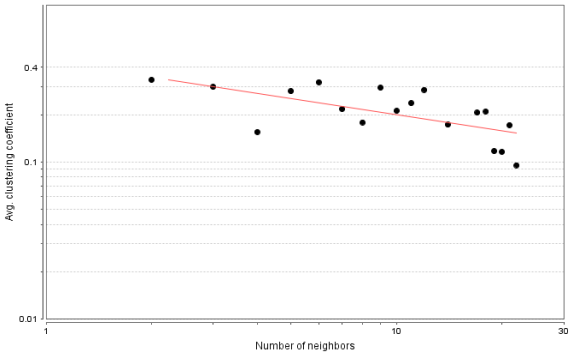

(b) Average clustering coefficient distribution of Park-model after model modifications. A power-law (red line) is fitted with the following equation: $C(k) = 0.439k^{-}0.341, R^2 = 0.424$

Figure 3.6. The clustering coefficient distribution of the (a) original and the (b) modified version of the Park-model on a log log scale.

Larger structural changes were performed on the Lu-model. The original model can be

divided into two main parts, one part representing the extracellular tumour microenvironment and the other part representing intracellular pathways in CRC (Figure 3.7a) [47]. The subpart representing the extracellular tumour microenvironment was removed to obtain a model representing only intracellular pathways. All nodes related to the microenvironment were removed, except IL6. The removal of IL6 prevented the model from reaching a stable state and was therefore kept in the modified model. In addition, the output nodes *Apoptosis* and *Proliferation* were substituted by the output nodes Antisurvival and Prosurvival respectively (Figure 3.7b).

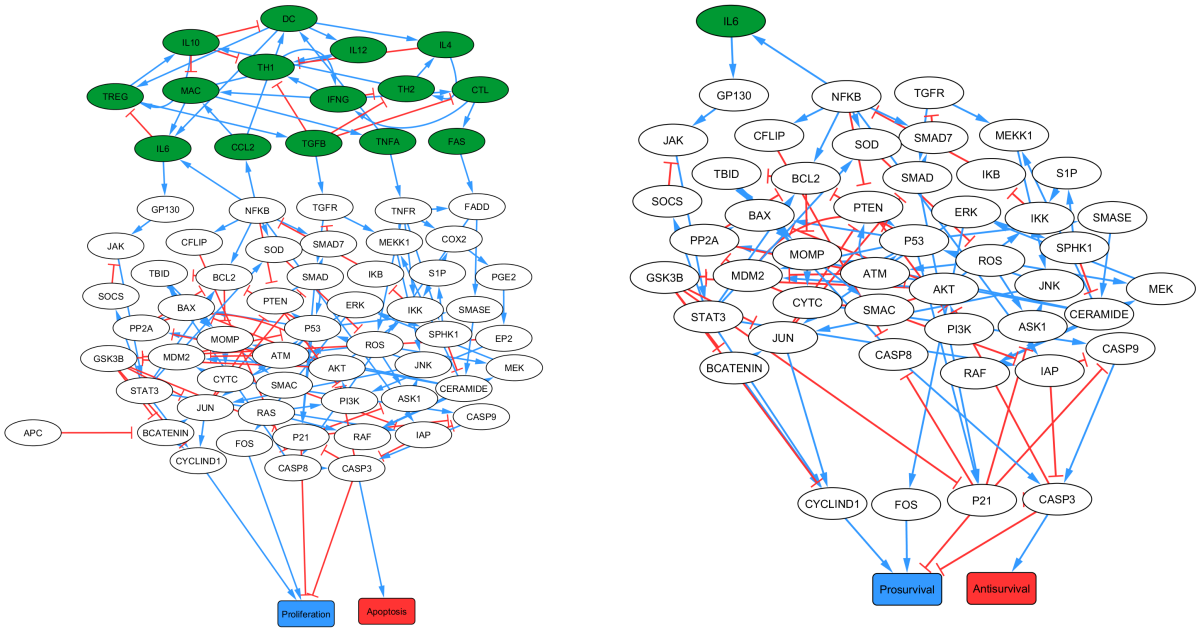

(a) Lu-model before model modifications including 70 nodes and 151 directed edges.

(b) Lu-model after model modifications including 49 nodes and 99 directed edges.

Figure 3.7. Lu-model (a) before and (b) after model modifications. Green nodes represent the extracellular microenvironment part of the model. Square nodes represent the phenotypic outputs Antisurvival and Prosurvival. Red arrows represent inhibiting interactions, while blue arrows represent activating interactions.

A power-law was fitted to the degree distribution of the original and modified Lu-model with the following equations (Figure 3.8):

Original model: $P(k) = 9.736k^{-0.502}, R^2 = 0.116$

Modified model: $P(k) = 7.462k^{-0.406}, R^2 = 0.121$

Neither the fitted power-law of the original, nor the modified Lu-model indicate a scale-free characteristic. Visual inspection of the degree distribution rather suggests that it follows a Poisson distribution, which is one of the hallmarks of random network models, suggesting that most nodes have an average degree [11].

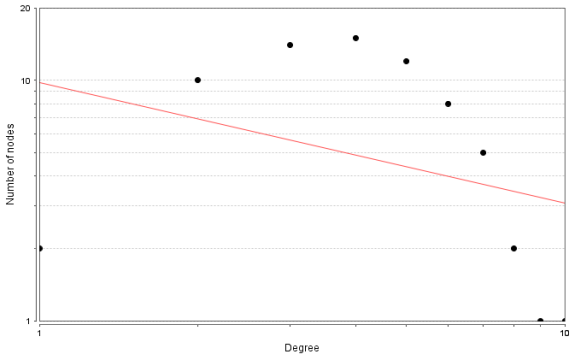

(a) Degree distribution of Lu-model before model modifications. A power-law (red line) is fitted with the following equation: $P(k) = 9.736k^{-0.502}$, $R^2 = 0.116$.

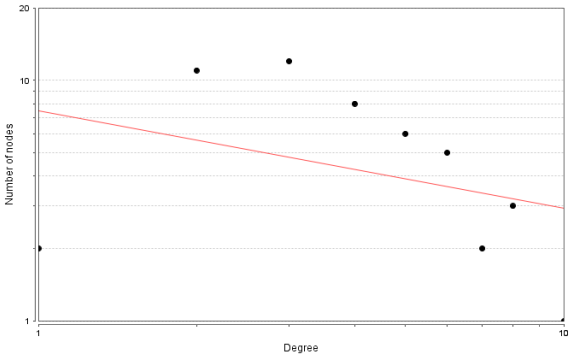

(b) Degree distribution of Lu-model after model modifications. A power-law (red line) is fitted with the following equation: $P(k) = 7.462k^{-0.406}$, $R^2 = 0.121$.

Figure 3.8. The degree distribution of the (a) original and the (b) modified version of the Lu-model on a log log scale.

A power-law was fitted to the average clustering coefficient distribution of the original and modified Lu-model with the following equations (Figure 3.9):

Original model: $C(k) = 0.099k^{-0.088}$, $R^2 = 0.016$

Modified model: $C(k) = 0.191k^{-0.298}$, $R^2 = 0.085$

No obvious hierarchical behaviour is observed for the original, nor the modified version of the Lu-model. Based on exponent decrease and the increase in R^2 value, one might argue that the hierarchical structure of the Lu-model is actually somewhat improved by model modifications.

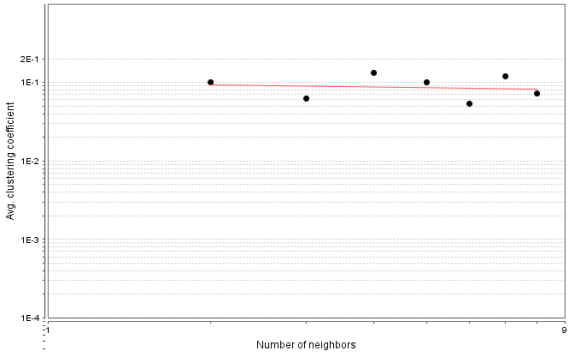

(a) Average clustering coefficient distribution of Lu-model before model modifications. A power-law (red line) is fitted with the following equation: $C(k) = 0.099k^{-0.088}$, $R^2 = 0.016$

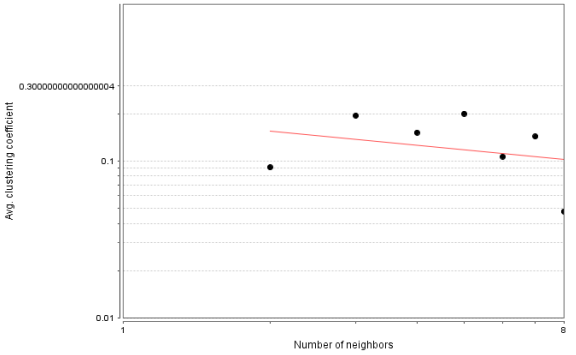

(b) Average clustering coefficient distribution of Lu-model after model modifications. A power-law (red line) is fitted with the following equation: $C(k) = 0.191k^{-0.298}$, $R^2 = 0.085$

Figure 3.9. The clustering coefficient distribution of the (a) original and the (b) modified version of the Lu-model on a log log scale.

Some model modification were performed on the Park and the Lu-models, while the origi-

nal network structure of CASCADE 1.0 was retained. It should be noted that these model modifications are not necessary requirements to run the DrugLogics synergy prediction pipeline. They are rather performed to limit the number of model specific adjustments and project steps. Larger multiscale models representing cancer development on different scales – from intracellular signalling and metabolism, to the effect of extracellular stimuli and cell-cell communication – should be considered in further research with the DrugLogics pipeline, as these elements could have great effect on drug response [75,76,80].

Model characterisation was performed to ensure that key network properties were not lost due to model modifications. No large changes in degree- or average clustering coefficient distribution are observed after model modification of the Lu- and Park-models. Both CASCADE 1.0 and the Park-model exhibit a scale-free structure, suggesting the presence of a few high degree hub nodes connected to a large number of low degree nodes. These hubs serve as the backbone of the network, being in close interaction with large fractions of the network, and thereby maintaining the structural integrity of the network [5]. The Lu-model, on the other hand, appears to have a more random network structure with a few low degree nodes, a few hubs and a large proportion of average degree nodes [11].

Cellular networks are usually hierarchical in structure, consisting of node communities only connected through a few number of hubs [5]. Such node communities represent groups of biomolecules, which interact both physically and functionally [10]. This modularity is present on different levels of the network, from physically connected protein complexes, to functionally related signalling molecules regulating the same cellular functions. No significant hierarchical structure is observed in any of the three models. The non-hierarchic structure can possibly be explained by the modelling strategy applied during network construction. Flobak et al., Park et al. and Lu et al. all apply a pathway oriented network construction strategy [20,47,60]. It can be suspected that this causes a more linear pathway network structure than a hierarchical module network structure. Additionally, in the CASCADE 1.0 model, all protein complexes are collapsed into single complex nodes, removing the modular layer of complexes.

No model is dismissed solely based on the absence of scale-freeness or hierarchical structure. The research done by the model creators suggests, that all three models are able to simulate certain cellular behaviours of cancer.

3.2 Collection of Cell Line Specific Baseline Activity Profiles for Model Calibration

A baseline activity profile gives an overview of the experimentally observed activity of each cancer related biomolecule included in a Boolean network model. Baseline activity profiles for the AGS cell line was retrieved from a paper published by Niederdorfer et al. [56]. The baseline activity profile was partly inferred from the literature, and partly from cell line copy number variations and gene expression data. COLO_205, HCT_116,

SW_48 and SW_620 specific baseline activity profiles were inferred from normalised and binarised transcription data. All baseline activity profiles are provided in Appendix C.

Ideally, the baseline activity profile should give a true representation of the observed activity of all cancer related biomolecules represented by a model. It should not be a relative description of the activity of biomolecules in a cancer cell compared to a healthy cell, but an absolute description of how these molecules are are acting in the cancer cell.

Creating good quality baseline activity profiles poses a great challenge, due to limitations regarding correct activity inference from omics data. In this project, cell line specific baseline activity profiles are completely or partly inferred from transcriptomic data. The validity of inferring protein activity from transcription data is however highly debated. The transcriptomic profile of a cell gives a snapshot of the temporary state of the cell and provides information about the set and the number of RNA molecules which are transcribed from the genome [72]. There is, however, no straight-forward correlation between the amount of mRNA and the amount of active protein in the cell [52]. Due to variations in the degradation rate of mRNA, there are variations in the number of proteins being translated from one mRNA molecule [52]. Analysing the proteome instead of the transcriptome can overcome some of these challenges, but also on the level of the proteome, challenges are faced when trying to infer protein activity from protein level measurements. The level of protein does not take into account how the protein activity is affected by post-translational modifications, the spatial location of the protein and other regulatory interactions between the protein and its environment [52, 71].

Phosphoprotomic analysis has been suggested as a source for assessing protein activity. The phosphorylation or dephosphorylation of a protein is often associated with an activating or deactivating regulation of a protein, and most signalling pathways in cancer are driven and mediated by protein phosphorylation [8]. Protein phosphorylation is easily detected, but the level or the site of phosphorylation is more difficult to identify. And again, there is not necessarily a straight forward relationship between the level of phosphorylation and activity. GSK3β and BRAF are examples of proteins which are deactivated rather than activated by phosphorylation [16]. Further development of good quality datasets and high performance tools for activity inference from phosphoproteomics is needed.

Different levels of omics data, from transcriptomics to phosphoproteomics, provide important information about protein activity and involvement in cellular signalling. However, no omics level is able to provide all the information necessary to infer protein activity and regulation. Hence, protein activity should ideally be assessed at as many levels as possible [52]. The integrative analyses of *multi-omics* data will hopefully improve the process of inferring protein activity and several bioinformatic tools are being developed to automate this process [6, 9, 49]. The use and integration of such tools, as a part of the DrugLogics framework, has been the main objective of the master's project of Victoria Nilsen Gjøvaag (Exploring Software Workflows to Optimise Biomarker Inference for Boolean Model Calibration and Drug Synergy Predictions, 2023). However, no exten-

sive multi-omics activity inference was conducted in this project. It is quite certain that transcriptomic data only provides a partial image of the baseline activity of proteins in a cancer cell. However, transcriptomics datasets are largely available in different databases and provide good coverage of model nodes which enabled the construction of complete baseline activity profiles for all cell lines.

3.3 Identification of Cell Line Specific Gold Standard Synergies

Cell line specific and experimentally verified gold standard synergies were retrieved from the literature. Flobak et al. provides an experimental validation of four drug synergies i AGS, among the pairwise combinations of seven targeted drugs [20]. A drug screen conducted by Jaaks et al. provides cell line specific drug synergies for the COLO_205, HCT_116, SW_48 and SW_620 cell lines. Synergistic drug combinations were further filtered for targets included in the Park- and Lu-models. All cell line and model specific gold standard synergies are presented in Appendix D.

Generally, a larger number of gold standard synergies are identified for the CRC cell lines, than AGS, as the number pairwise drug combinations tested by Jaaks et al. is much larger than the number of pairwise drug combinations tested by Flobak et al. (2025 versus 21) [20, 35]. It should also be noted, that two different synergy calculation methods are applied in each respective synergy screen. In the Jaaks et al. screen, Bliss independence is applied to assess drug synergy, while Flobak et al. apply Loewe additivity. Different synergy calculation methods can provide different synergy results [23]. This difference is, however, accounted for during *in silico* synergy predictions with Drabme, as different synergy calculation methods are computationally implemented, and can be applied during synergy predictions.

The Bliss independence model applied by Jaaks et al. corresponds to the Bliss method applied during synergy predictions with Drabme. Loewe additivity, however, can not be applied by the Drabme module, as the implementation of dose-response curves is not supported by the binary modelling framework. However, as explained by Flobak et al., a drug combination is considered synergistic, according to Loewe additivity, if "the combined effect outperforms the effect of either drug" [20]. This interpretation is similar to the HSA method ($E_{AB} > \max(E_A, E_B)$), which is implemented in the Drabme module and was considered the appropriate alternative to Loewe additivity.

3.4 Calculation of Degree Z-score, DP, and a Near-minimal FVS

For all model nodes included in CASCADE 1.0, Park- and Lu-models, the degree Z-score and DP was calculated. In addition, a near-minimal FVS was identified for each model. In

this section it is investigated whether or not these three measures suggest unique possible driver sets or not.

3.4.1 Top Nodes Based on Degree Z-score

The top 10% subset of all model nodes, based on degree Z-score, is provided for each Boolean model in table 3.2. The Z-scores for all remaining model nodes are given in Appendix E.

A node is considered a hub if it has a degree Z-score above 2.5, as given by Guimera and Amaral [27]. Five hub nodes are identified in CASCADE 1.0 and the Park-model, while only one hub is identified for the Lu-model. The difference in hubbiness is related to differences in degree distribution observed for the three models. The scale-free network structure of CASCADE 1.0 and the Park-model is characterised by a high number of low-degree nodes and a high number of high-degree nodes, compared to models with a random network structure, such as the Lu-model [11]. The limited number of hubs identified for the Lu-model might be a first indication that degree Z-score is not a suitable measure for target control, in the case of the Lu-model.

Based on Z-score, AKT is among the top nodes across all models. The high Z-score can be related to the biological relevance of AKT in many human cancers [66]. AKT is a key kinase, affecting the activity of many downstream proteins involved in cell survival and proliferation. This extensive signalling involvement is reflected in the topology of all three Boolean models.

Table 3.2. Nodes with the highest degree Z-score in CASCADE 1.0, Park-model and Lu-model.

Degree Z-score					
CASCADE 1.0		**Park-model**		**Lu-model**	
Node	**Score**	**Node**	**Score**	**Node**	**Score**
ERK_f	3.956	Akt	3.302	P53	2.950
AKT_f	3.523	ERK	3.092	NFKB	1.960
MAPK14	3.090	PP2A	2.883	AKT	1.960
GSK3_f	2.656	p53	2.673	P21	1.960
LRP_f	1.790	GSK3beta	2.044	CASP3	1.465
TSC_f	1.356	c_Myc	2.044		
RSK_f	1.356	p38	1.625		
TCF7_f	0.923	JNK	1.625		
		Bax	1.416		

3.4.2 Top Nodes Based on DP

The top 10% subset of all model nodes, based on DP is provided for each Boolean model in table 3.3. The DP for all remaining model nodes are given in Appendix E.

Across all three models, AKT is also among the top nodes based on DP. The upper possible DP limit for a node depends on the number of outgoing interactions, as the mutual information is summarised over all outputs [62]. Hence, there might be a correlation between the high Z-score of AKT and the high DP. However, some nodes are included in the subset of top nodes based on DP, but not Z-score. One example is the RAC_f node included on CASCADE 1.0. RAC_f and its nearest neighbours are visualised in Figure 3.10.

RAC_f has a degree of 4 and a degree Z-score of 0.056. However, RAC_f constitutes the only input node of MAP3K11 and MAP3K4, giving it complete determinative power over the state of these two nodes. Hence, the DP-score of RAC_f is 2.000, making it one of the top nodes in CASCADE 1.0 based on DP. This example illustrates how Z-score and DP are not always correlated.

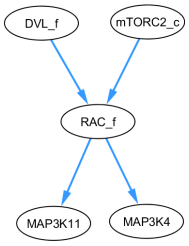

Figure 3.10. RAC node and its four nearest neighbours

Table 3.3. Nodes with the highest DP in CASCADE 1.0, Park-model and Lu-model

Determinative power					
CASCADE 1.0		**Park-model**		**Lu-model**	
Node	**Score**	**Node**	**Score**	**Node**	**Score**
AKT_f	4.059	ERK	3.794	NFKB	2.828
MAPK14	3.193	p53	3.754	GSK3B	2.220
TCF7_f	2.623	Akt	3.155	ERK	2.019
ERK_f	2.262	ATM	2.884	MOMP	2.000
LRP_f	2.008	GSK3beta	2.617	AKT	1.907
RAC_f	2.000	Smad2_3	2.311		
MAP3K7	1.999	PP2A	2.245		
IKBKB	1.690	p38	1.851		
		Src	1.733		

3.4.3 Near-minimal FVS

Table 3.4 gives an overview of all nodes included in a near-minimal FVS identified for each Boolean model. Across all three models, between a third and a fourth of all network nodes are included in a near-minimal FVS. Newby et al. identified a near-minimal FVS for 6 different network models, with a size ranging from 28 to 60 nodes [55]. They report that the size of the near-minimal FVSs identified ranged from 8 to 17 nodes, which corresponds to a 30% subset, and is consistent with the size of the near-minimal FVSs identified in this project.

Table 3.4. All nodes included in the near-minimal FVS identified for CASCADE 1.0, Park-model and Lu-model

Near-minimal FVS		
CASCADE 1.0	**Park-model**	**Lu-model**
26/77 nodes (34%)	**24/91 nodes (26%)**	**15/49 nodes (31%)**
AKT_f, AKT1S1, BTRC, CTNNB1, DUSP6, ERK_f, GRB2, GSK3_f, KRAS, LRP_f, MAPK14, MDM2, MDM2_g, MEK_f, mTORC1_c, mTORC2_c, PDPK1, PIK3CA, RAF_f, RHEB, RTPK_f, S6K_f SHC1, TCF7_f, TP53,TSC_f	Akt, AXIN, beta catenin, CyclinA, CyclinB, E2F1, ERK, GSK3beta, JNK, MDM2, mTOR1, mTOR2, p38, PI3K, p53, PDPK1, PIP3, PP2A, S6K, SHP2, Smad2_3, Smad7, Src, TSC1	AKT, CASP3, CASP8, CASP9, ERK, JAK, MEK, P21, P53, SMAD, SMAD7, SOCS, SPHK1, STAT3, TGFR

3.4.4 Degree Z-score, DP, and Near-minimal FVS Give Unique Node Subsets

There is some overlap between the selection of nodes with the top 10% highest degree Z-score, the selection of nodes with the top 10% highest DP and the near-minimal FVS. (Figure 3.11). However, all measures identify a unique subset of nodes across all three models. No subset is completely covered by any other subset.

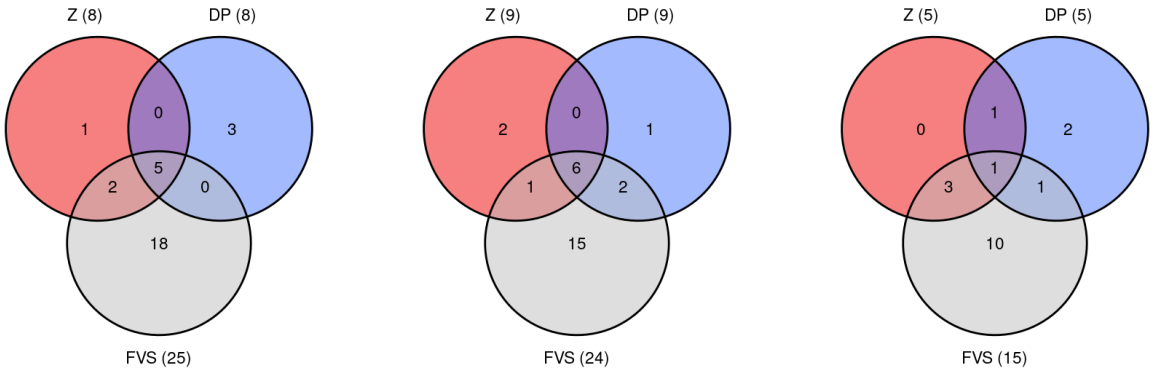

(a) CASCADE 1.0 *(b) Park-model* *(c) Lu-model*

Figure 3.11. A venndiagram indicating the overlap between nodes with high degree Z-score (10% highest), nodes with high DP (10% highest) and nodes included in the near-minimal FVS of (a) CASCADE 1.0, (b) Park-model and (c) Lu-model.

Since each measure provides a unique subset of nodes and covers a different node property, they are further investigated as possible driver set identifiers and used to select subsets of baseline data for Boolean model calibration.

3.5 Effect of Calibration Data Subsetting on Calibrated Model Stable State

The aim of Boolean model calibration, using the Gitsbe software module, is to obtain a calibrated model whose stable state reflects a target state. In this section, it is investigated if calibration of a Boolean model, with respect to a possible driver set of nodes, will ensure a calibrated model with a stable state which correctly represents the target state.

Boolean model calibration can be described as a Boolean model optimisation problem. It is a search for an optimal model in a model solution space, and the best model solution is the one that reflects the target state. The feasible model solution space is restricted by the topology of the Boolean input model, as it can only reach a limited number of possible stable states [67]. Mutations introduced to the logical rules during model calibration can, however, increase the number of possible stable states, as is exemplified by the exchange of an OR operator against an AND operator in the toy example in Figure 3.12. Hence, the model solution space is rather restricted to the possible stable states of the Boolean input model and all possible mutated counterparts.

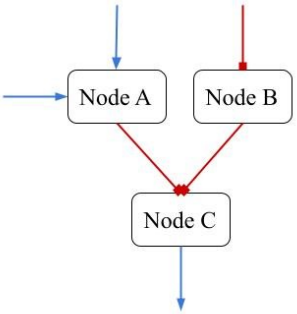

C = NOT (A OR B)	C = NOT (A AND B)
[A,B,C]	[A,B,C]
~~[0,1,0]~~	[0,1,0]
~~[1,0,0]~~	[1,0,0]
[0,0,1]	[0,0,1]
[1,1,0]	[1,1,0]
~~[0,0,0]~~	~~[0,0,0]~~
~~[0,1,1]~~	~~[0,1,1]~~
~~[1,1,1]~~	~~[1,1,1]~~
~~[1,0,1]~~	~~[1,0,1]~~

Figure 3.12. Model solution space for a three-node sub-network. Exchanging the OR operator for an AND operator in the logical rule of node C increases the number of possible state solutions from two to four.

The model solution space is further constrained by the calibration dataset, as it defines the target state of some nodes, and acts as an objective guiding model calibration. The activity of a node is a dependent variable as it is determined by the activity of its regulators. Hence, including information about the target activity of one node in the calibration dataset will also provide information about the target activity of other nodes, as their activity is inferred from this main node. Due to this node interdependence, it is hypothesised that only including the target activity for a set of driver nodes is sufficient to obtain a calibrated model whose stable state is compliant with the whole target state, as the target activity of all remaining nodes will be inferred from this driver set. This hypothesis is illustrated by a toy example in Figure 3.13. The toy example includes a

three-node sub-network where node A and node B inhibit node C. The topology of the sub-network itself constrains the possible model solution space. The solution space is further constrained as node A is defined as active in calibration dataset 1. The activity of node A and B in calibration dataset 2 constitutes a driver set as it only allows one possible model solution.

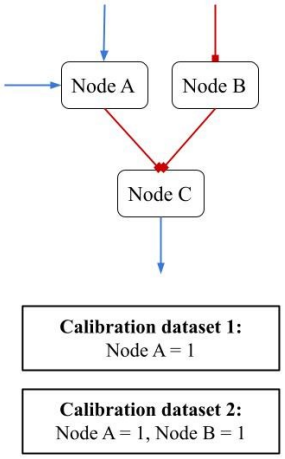

Model solution space constrained by topology	Model solution space constrained by calibration dataset 1	Model solution space constrained by calibration dataset 2
[A,B,C]	[A,B,C]	[A,B,C]
[0,1,0]	~~[0,1,0]~~	~~[0,1,0]~~
[1,0,0]	[1,0,0]	~~[1,0,0]~~
[0,0,1]	~~[0,0,1]~~	~~[0,0,1]~~
[1,1,0]	[1,1,0]	[1,1,0]
~~[0,0,0]~~	~~[0,0,0]~~	~~[0,0,0]~~
~~[0,1,1]~~	~~[0,1,1]~~	~~[0,1,1]~~
~~[1,1,1]~~	~~[1,1,1]~~	~~[1,1,1]~~
~~[1,0,1]~~	~~[1,0,1]~~	~~[1,0,1]~~

Figure 3.13. The model solution space for a three-node sub-network is restricted both by the topology and the applied calibration dataset. Calibration dataset 2 constitutes a driver set as it only allows one possible model solution.

This driver-based calibration strategy was applied to calibrate three Boolean cancer models representing AGS (CASCADE 1.0) and CRC (Park-model and Lu-model). The target state for model calibration was given by the cell line specific baseline activity profiles of AGS, COLO205, HCT116, SW48, and SW620. Subsets of data from these baseline activity profiles were sampled for possible driver sets, based on degree Z-score, DP, and a near-minimal FVS. A near-minimal FVS constitutes a single possible driver set. Z-score and DP, on the other hand, are continuous measures. Hence, 10 possible driver sets – including the top 10%, 20%, ... 100% nodes – were sampled for each measure.

The output from model calibration is an ensemble of calibrated models. If a true driver set constrains the model solution space in a way that only leaves one possible target state, then every model in the calibrated model ensemble should reach this target state. Hence, the efficiency of the driver-based calibration strategy is evaluated both in terms of stable state homogeneity across the ensemble, and the compliance between the stable state of the calibrated model ensemble and the target state defined by the baseline activity profile. All results obtained by driver-based model calibration are presented in the following sections, followed by a discussion of main findings.

3.5.1 Model Calibration Using Possible Driver Sets Based on Degree Z-score

For CASCADE 1.0, an increased level of stable state homogeneity is observed, as the sample size of the possible driver set (Z-score) increases. (Figure 3.14). There is a notable increase in stable state homogeneity as the size of the possible driver set exceeds 30%. However, no overall homogeneous stable state is obtained for any calibrated model ensemble. The increase in stable state homogeneity across model ensembles is also reflected in an increase in baseline compliance. The highest compliance level – of 0.783 – is obtained when CASCADE 1.0 is calibrated to the complete baseline activity profile of AGS. The stable state of nodes such as RHEB, MAP2K4, MAP3K11, MAP3K4, TSC_f and mTORC1_c violate their baseline activity across stable states.

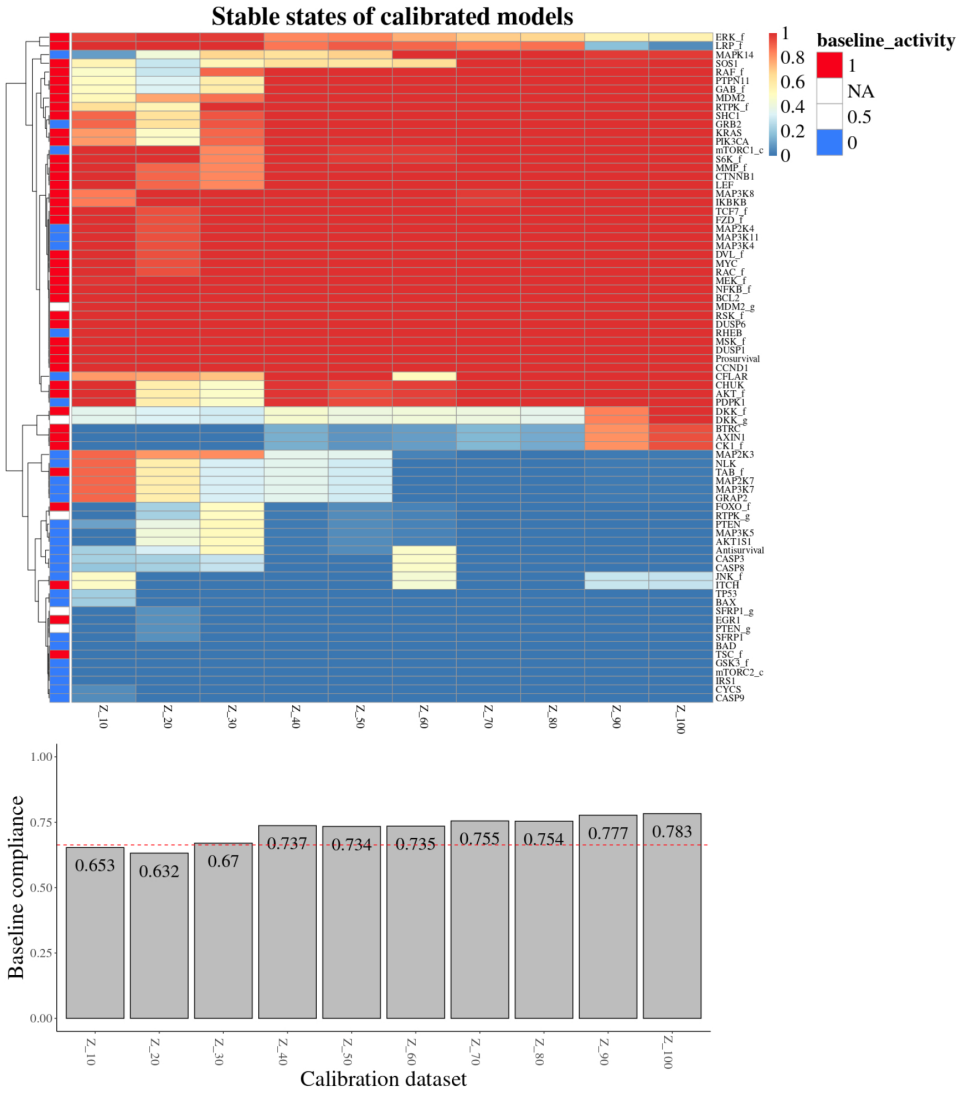

Figure 3.14. Ensemble-wise stable state heatmap for CASCADE 1.0. Columns are ordered by the size of the possible driver set (Z-score), and an annotation row indicates the experimentally observed AGS baseline activity. A baseline compliance plot is provided below the heatmap, and the baseline compliance of the uncalibrated model is indicated by a red line.

The stable state of the calibrated Park-model shows high levels heterogeneity across all cell lines, and no consistent stable state is reached by any calibrated model ensemble (Figure 3.15). However, there seems to be an increase in stable state homogeneity as the size of the possible driver set increases. Across all cell lines, this increase in stable state homogeneity seems to coincide with an increase in baseline compliance. The highest compliance level – of 0.755 – is obtained by the Park-model calibrated to the complete baseline activity profile of the SW_620 cell line.

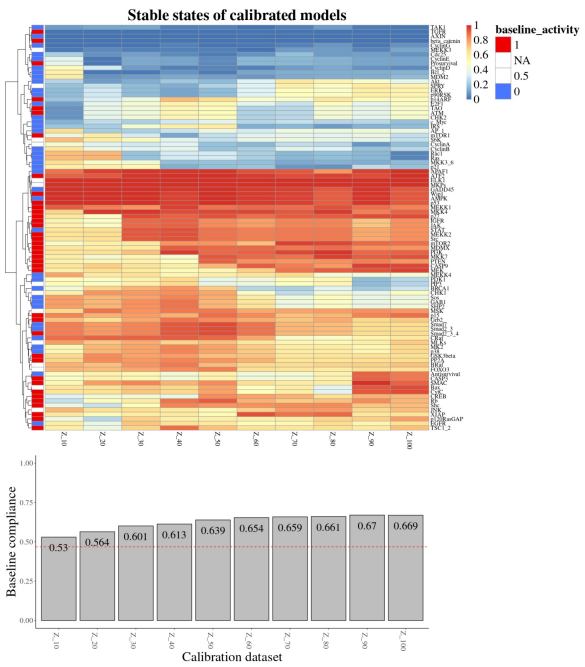

(a) COLO_205

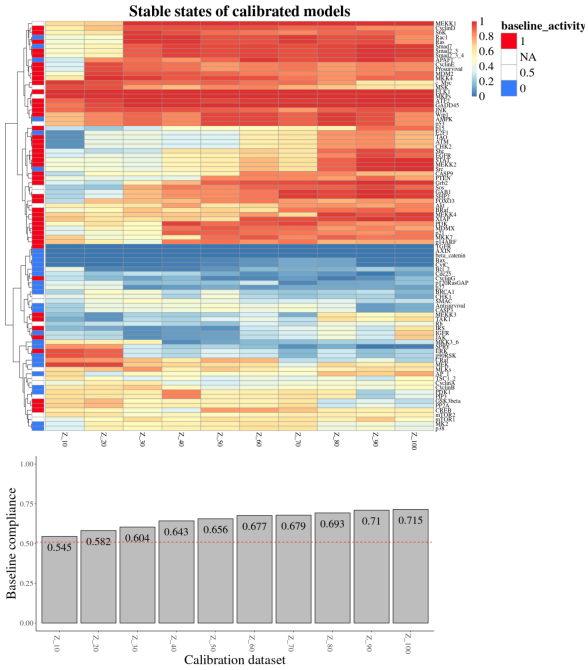

(b) HCT_116

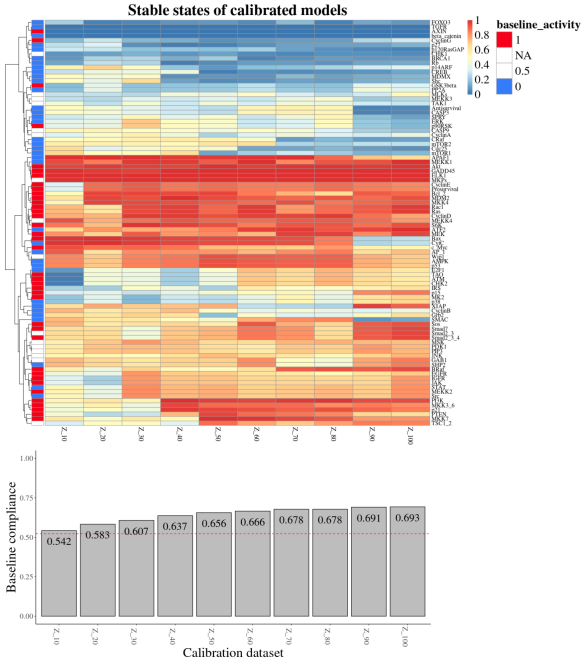

(c) SW_48

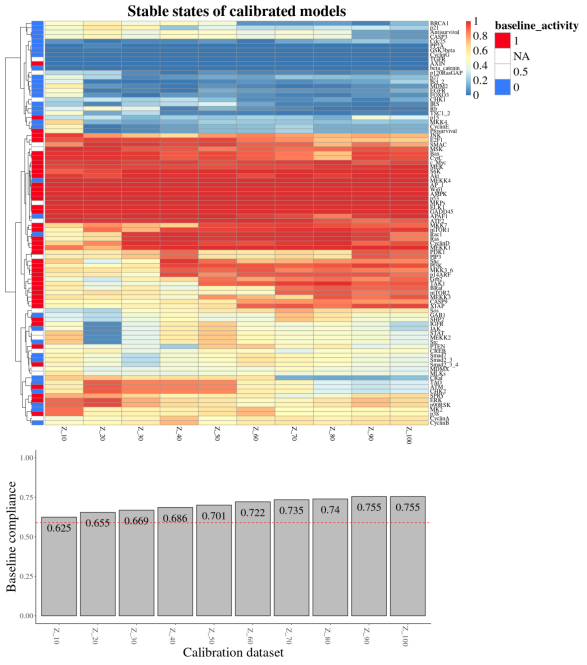

(d) SW_620

Figure 3.15. Ensemble-wise stable state heatmap for the Park-model calibrated to the (a) COLO_205, (b) HCT_116, (c) SW_48 and (d) SW_620 cell line. Columns are ordered by the size of the possible driver set (Z-score), and an annotation row indicates the experimentally observed cell line specific baseline activity. A baseline compliance plot is provided below every heatmap, and the baseline compliance of the uncalibrated model is indicated by a red line.

The stable state of the calibrated Lu-model differs between cell lines (Figure 3.16). When the Lu-model is calibrated to the baseline data of the COLO_205 and HCT_116 cell lines, the stable state homogeneity increases as the size of the possible driver set (Z-score) increases. However, for the HCT_116 cell line, a high level of stable state heterogeneity is observed when calibrated to the complete baseline activity profile. For both cell lines, higher levels of stable state homogeneity seems to be associated with higher levels of baseline compliance, but no overall baseline compliant stable state is obtained. For the SW_48 and SW_620 cell lines, model ensembles switch between different stable states. Some of these switches are reflected in the compliance plot as well. For the SW_48 cell line, ensemble-wise stable states with larger fractions of inactive nodes are associated with higher baseline compliance, while the opposite is true for the SW_620 cell line. Across all cell lines, the highest compliance level – of 0.679 – is obtained by the Lu-model, calibrated to a 90% sample of the COLO_205 baseline activity profile.

Across all stable states, 15 nodes (ATM, CASP8, CFLIP, GP130, IKB, IKK, IL6, JAK, NFKB, ROS, SMAD7, SOCS, SOD, STAT3, TGFR) are observed to be consistently active or inactive, even though the baseline activity of these nodes differs between cell lines.

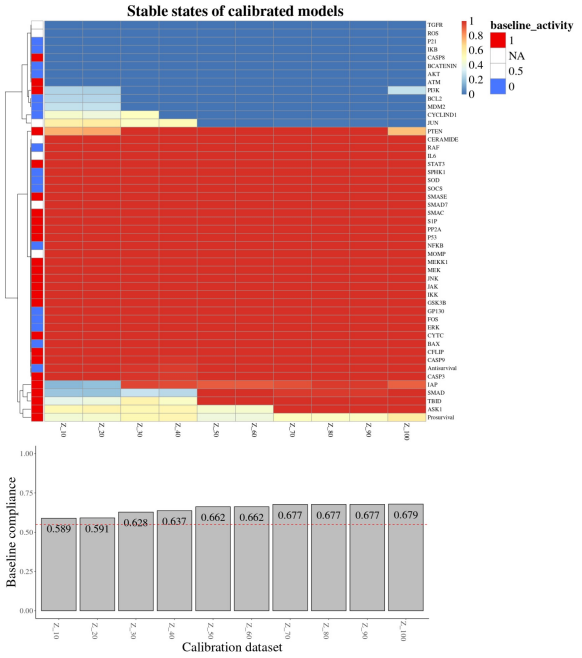

(a) COLO_205

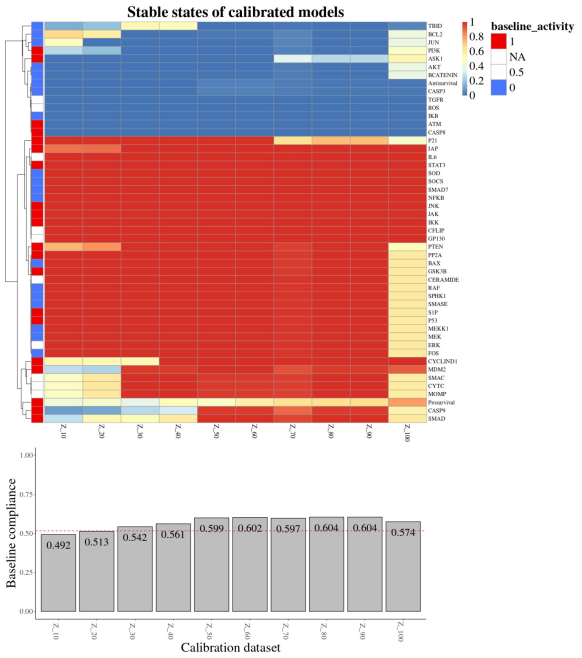

(b) HCT_116

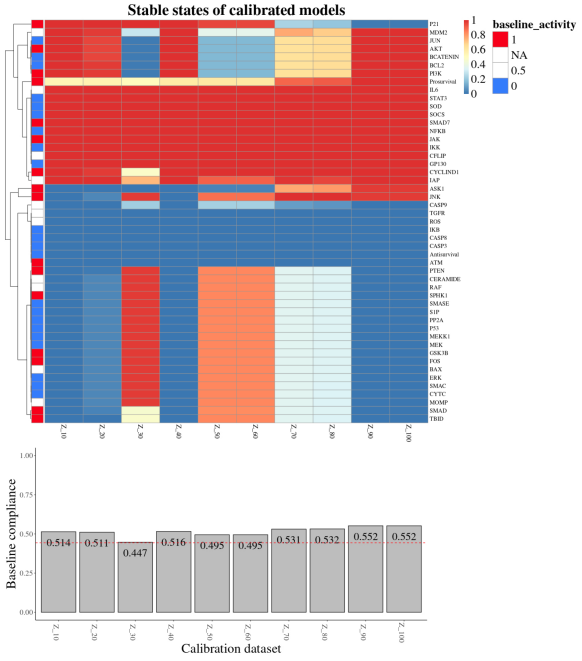

(c) SW_48

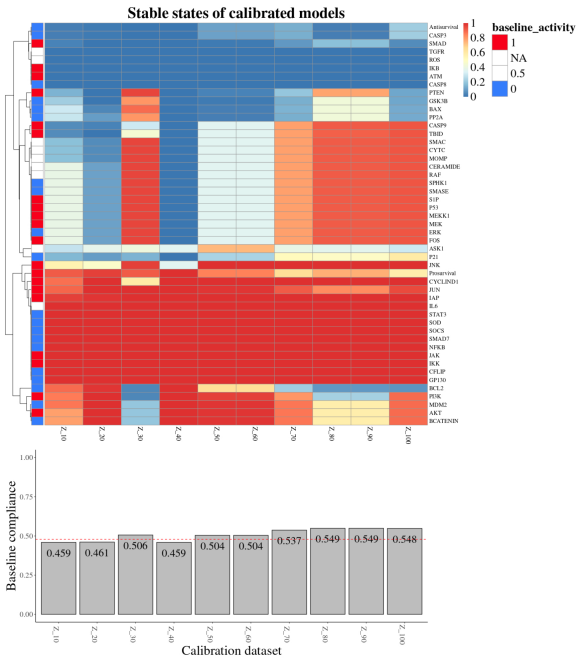

(d) SW_620

Figure 3.16. Ensemble-wise stable state heatmap for the Lu-model calibrated to the (a) COLO_205, (b) HCT_116, (c) SW_48 and (d) SW_620 cell line. Columns are ordered by the size of the possible driver set (Z-score), and an annotation row indicates the experimentally observed cell line specific baseline activity. A baseline compliance plot is provided below every heatmap, and the baseline compliance of the uncalibrated model is indicated by a red line.

3.5.2 Model Calibration Using Possible Driver Sets Based on DP

The ensemble-wise stable state of CASCADE 1.0, calibrated to possible driver sets (DP), can be divided into three main groups: largely homogeneous, partly homogeneous and largely heterogeneous (Figure 3.17). When CASCADE 1.0 is calibrated to possible driver sets of 10% to 50%, the average stable state of the calibrated model ensemble has some areas of stable state homogeneity, and some areas of heterogeneity. When CASCADE 1.0 is calibrated to possible driver sets of 70% to 100%, average stable states are highly homogeneous. However, no overall homogeneous stable state is observed across ensembles. The stable state of CASCADE 1.0 calibrated to a possible driver set of 60% stands out as being highly heterogeneous across the model ensemble.

Differences in stable state homogeneity are reflected in the baseline compliance plot. Higher levels of ensemble-wise stable state homogeneity is associated with higher levels of baseline compliance. The calibrated model ensemble with the highest level of stable state heterogeneity does also have the lowest compliance level. The highest compliance level – of 0.783 – is observed for CASCADE 1.0 calibrated to the complete AGS baseline activity profile.

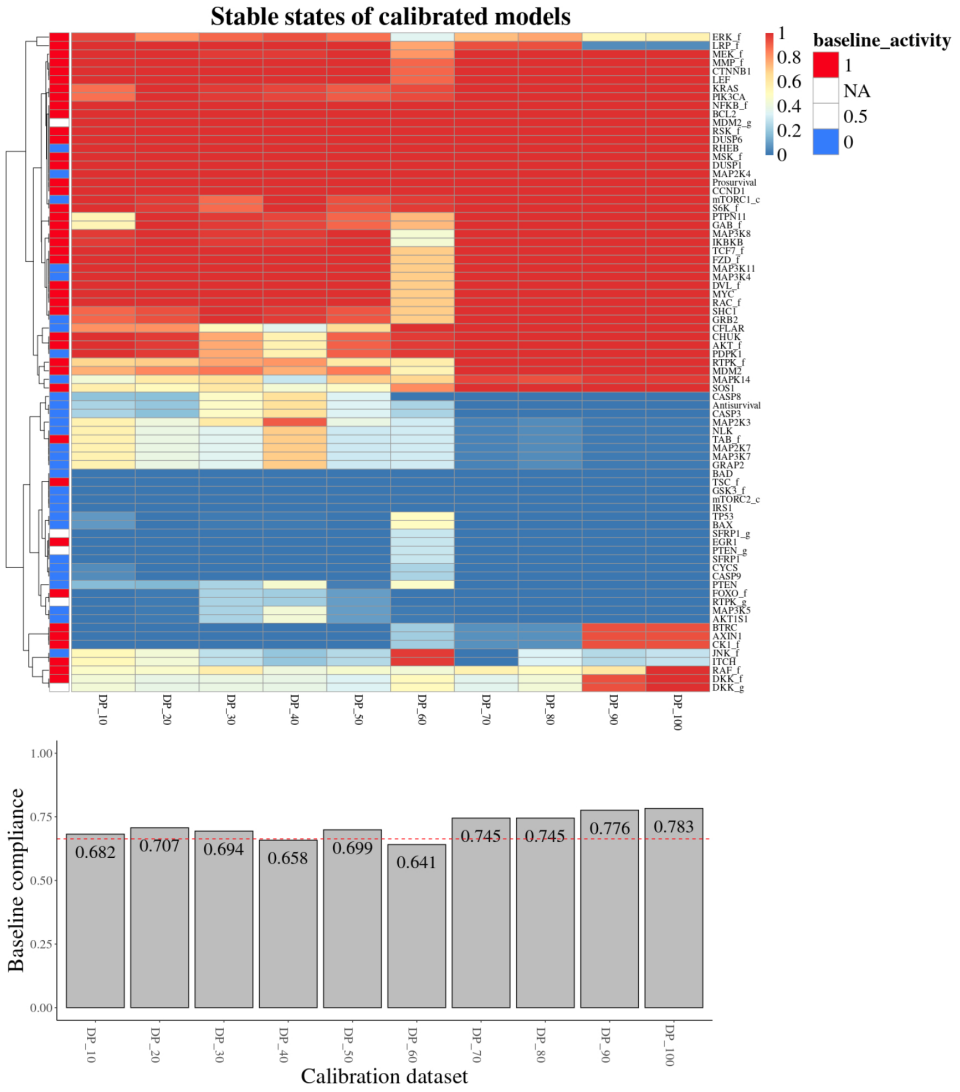

Figure 3.17. Ensemble-wise stable state heatmap for CASCADE 1.0. Columns are ordered by the size of the possible driver set (DP), and an annotation row indicates the experimentally observed AGS baseline activity. A baseline compliance plot is provided below the heatmap, and the baseline compliance of the uncalibrated model is indicated by a red line.

High levels of stable state heterogeneity is observed for the calibrated Park-model, and no homogeneous stable state is reached across any ensemble (Figure 3.18). The tendency is, however, that there is an increase in stable state homogeneity for models calibrated to possible driver sets (DP) of a larger size. This increase in stable state homogeneity is reflected in an increase in baseline compliance across all cell lines, and the highest compliance level – of 0.761 – is observed for the Park-model calibrated to the complete baseline activity profile of the SW_620 cell line.

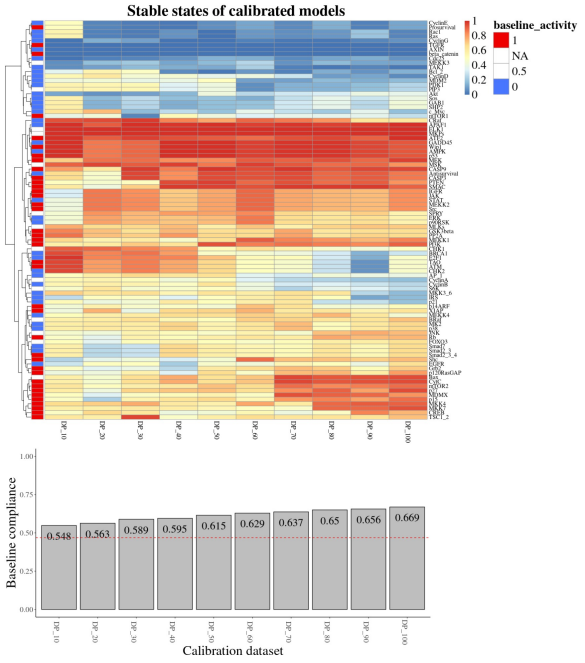

(a) COLO_205

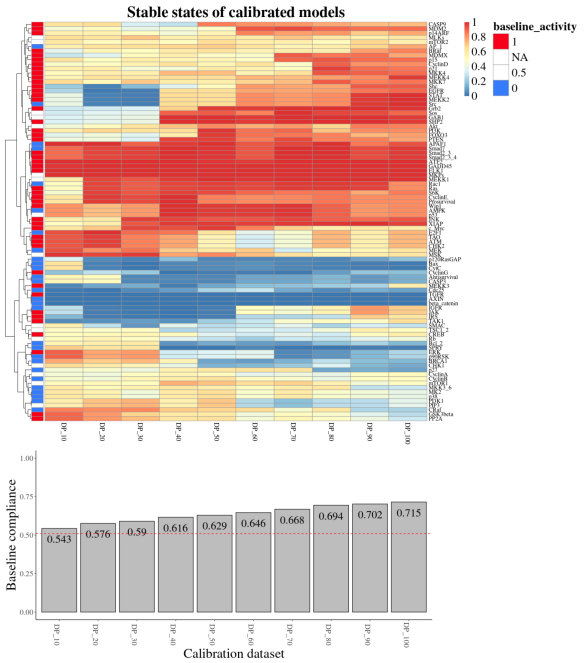

(b) HCT_116

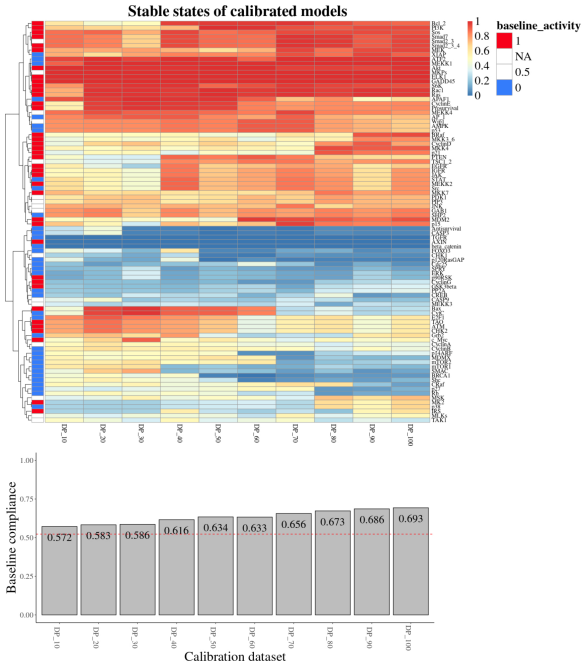

(c) SW_48

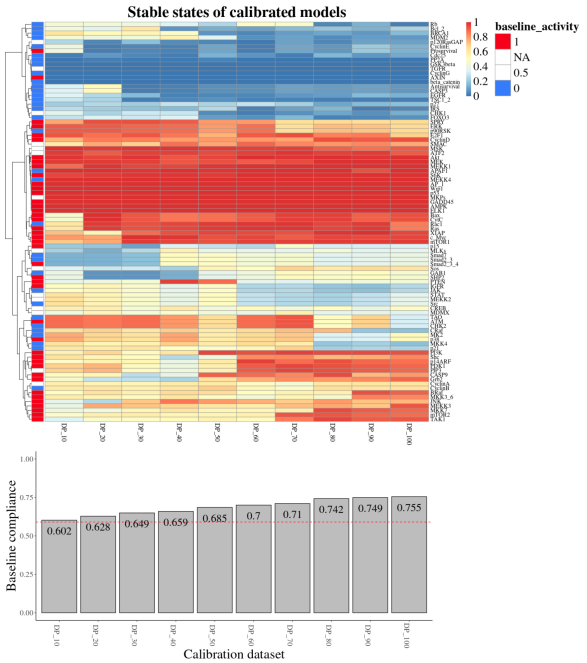

(d) SW_620

Figure 3.18. Ensemble-wise stable state heatmap for the Park-model calibrated to the (a) COLO_205, (b) HCT_116, (c) SW_48 and (d) SW_620 cell line. Columns are ordered by the size of the possible driver set (DP), and an annotation row indicates the experimentally observed cell line specific baseline activity. A baseline compliance plot is provided below every heatmap, and the baseline compliance of the uncalibrated model is indicated by a red line.

Different stable state patterns are observed for the calibrated Lu-model across cell lines (Figure 3.19). When the Lu-model is calibrated to the COLO_205 and the HCT_116 cell lines, there is an increase in stable state homogeneity as the size of the possible driver

set (DP) gets larger. However, for the HCT_116 cell line, there is a sudden increase in stable state heterogeneity as the sample size exceeds 80%. This is not observed in the COLO_205 cell line. In the stable state heatmaps of the Lu-model calibrated to the SW_48 and SW_620 cell lines, several stable state switches are observed.

The increase in stable state homogeneity observed for the COLO_205 cell line seems to coincide with an increase in baseline compliance. The Lu-model, calibrated to the complete baseline activity profile of COLO_205, obtains the highest compliance – of 0.679. For the SW_48 cell line, a stable state characterised by a larger fraction of inactive nodes is associated with a higher compliance, while the opposite is true for the SW_620 cell line. However, no overall baseline compliant stable state is obtained by any calibrated model ensemble.

Across all calibrated model stable states, a group of 15 nodes (ATM, CASP8, CFLIP, GP130, IKB, IKK, IL6, JAK, NFKB, ROS, SMAD7, SOCS, SOD, STAT3, TGFR) are observed consistently active or inactive, even though their baseline activity differs between cell lines.

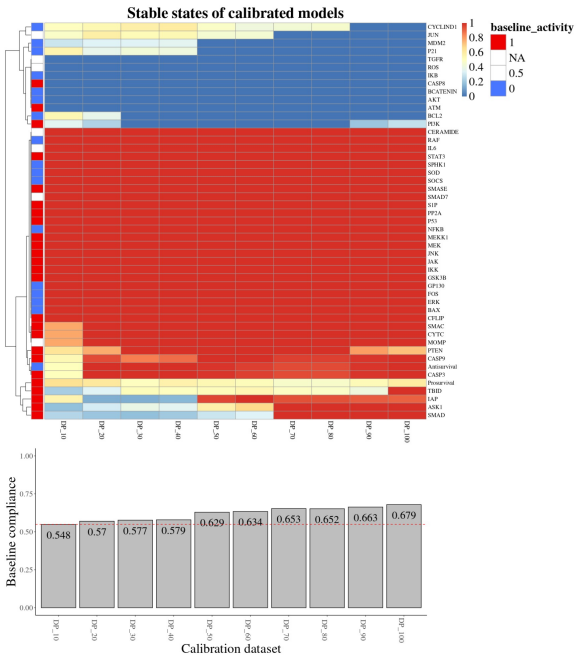

(a) COLO_205

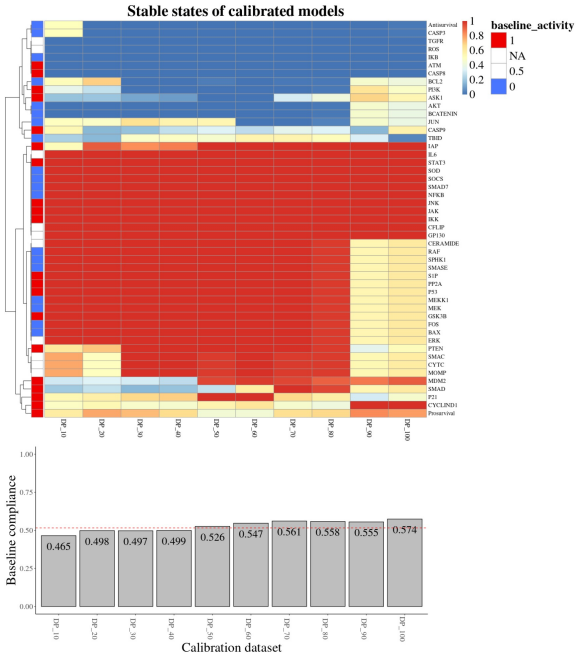

(b) HCT_116

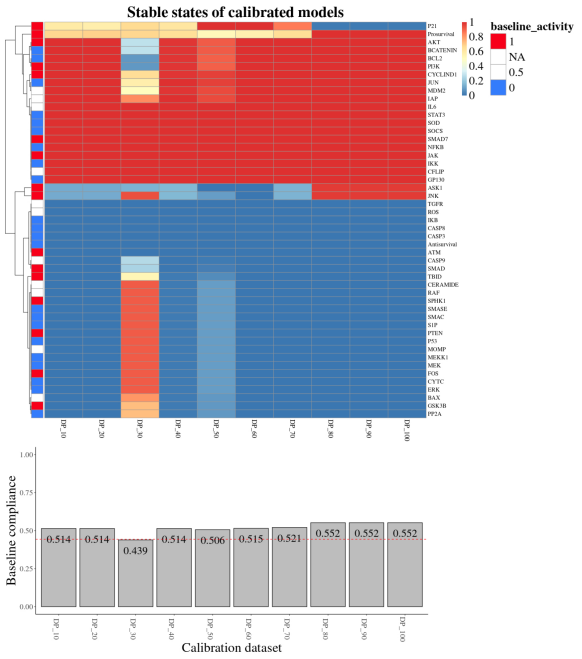

(c) SW_48

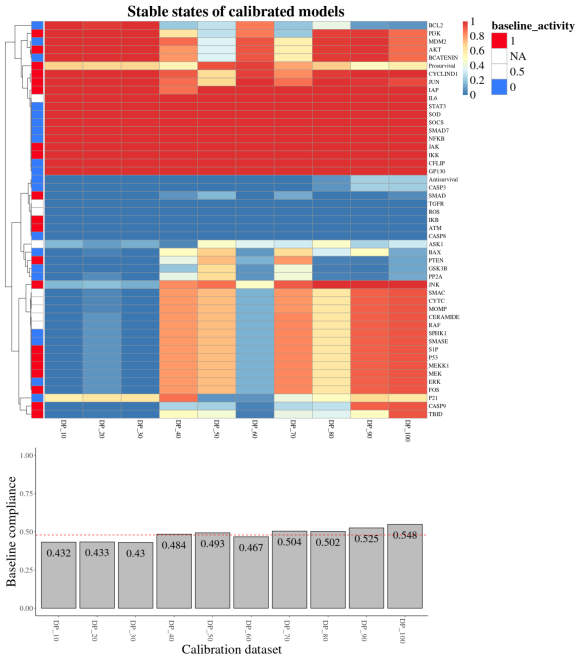

(d) SW_620

Figure 3.19. Ensemble-wise stable state heatmap for the Lu-model calibrated to the (a) COLO_205, (b) HCT_116, (c) SW_48 and (d) SW_620 cell line. Columns are ordered based on the size of the possible driver set (DP), and an annotation row indicates the experimentally observed cell line specific baseline activity. A baseline compliance plot is provided below every heatmap, and the baseline compliance of the uncalibrated model is indicated by a red line.

3.5.3 Model Calibration Using a Possible Driver Set Based on a Near-minimal FVS

Some stable state heterogeneity is observed for the model ensemble of CASCADE 1.0 calibrated to a possible driver set given by the near-minimal FVS (Figure 3.20). The compliance between this stable state and the AGS baseline activity profile is 0.693.

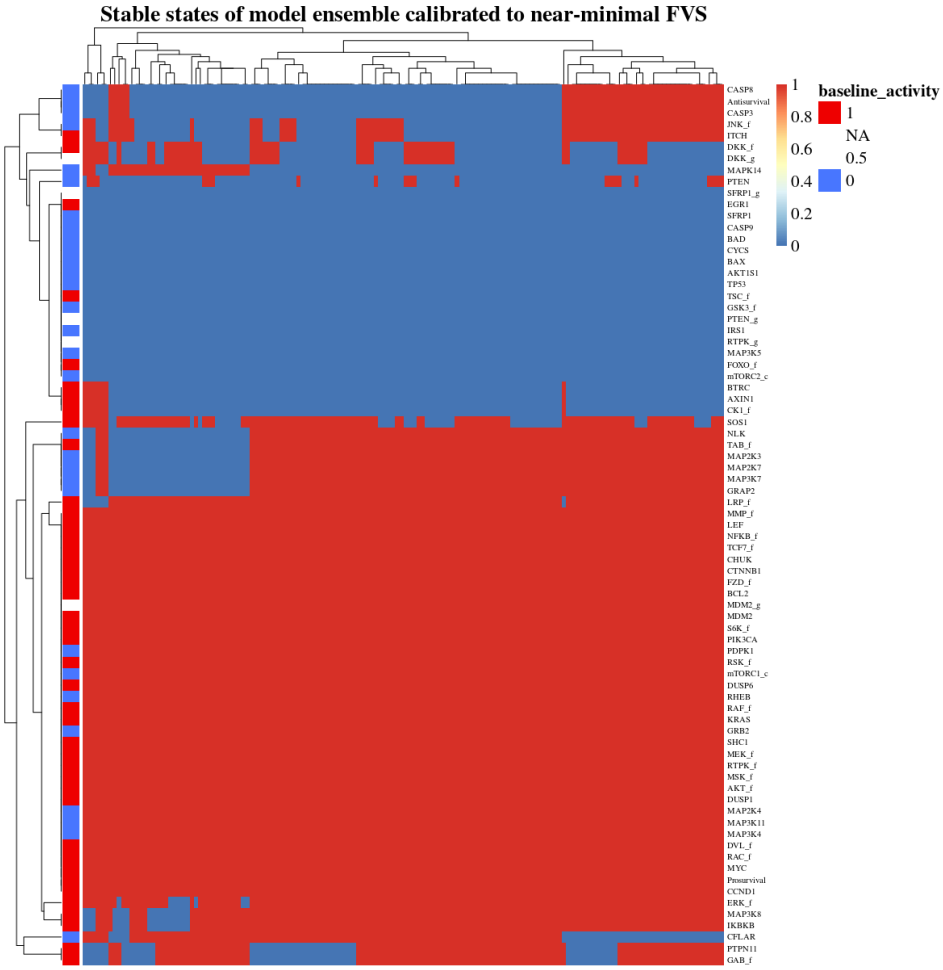

Figure 3.20. Model-wise stable state heatmap for CASCADE 1.0 calibrated to a possible driver set based on a near-minimal FVS. Model nodes are represented by rows, and individual models in the calibrated model ensemble are represented by columns. An annotation row indicates the experimentally observed baseline activity of AGS.

The stable state of the calibrated Park-model is largely heterogeneous across model ensembles (Figure 3.21). No homogeneous stable state is obtained across the model ensemble, for any cell line.

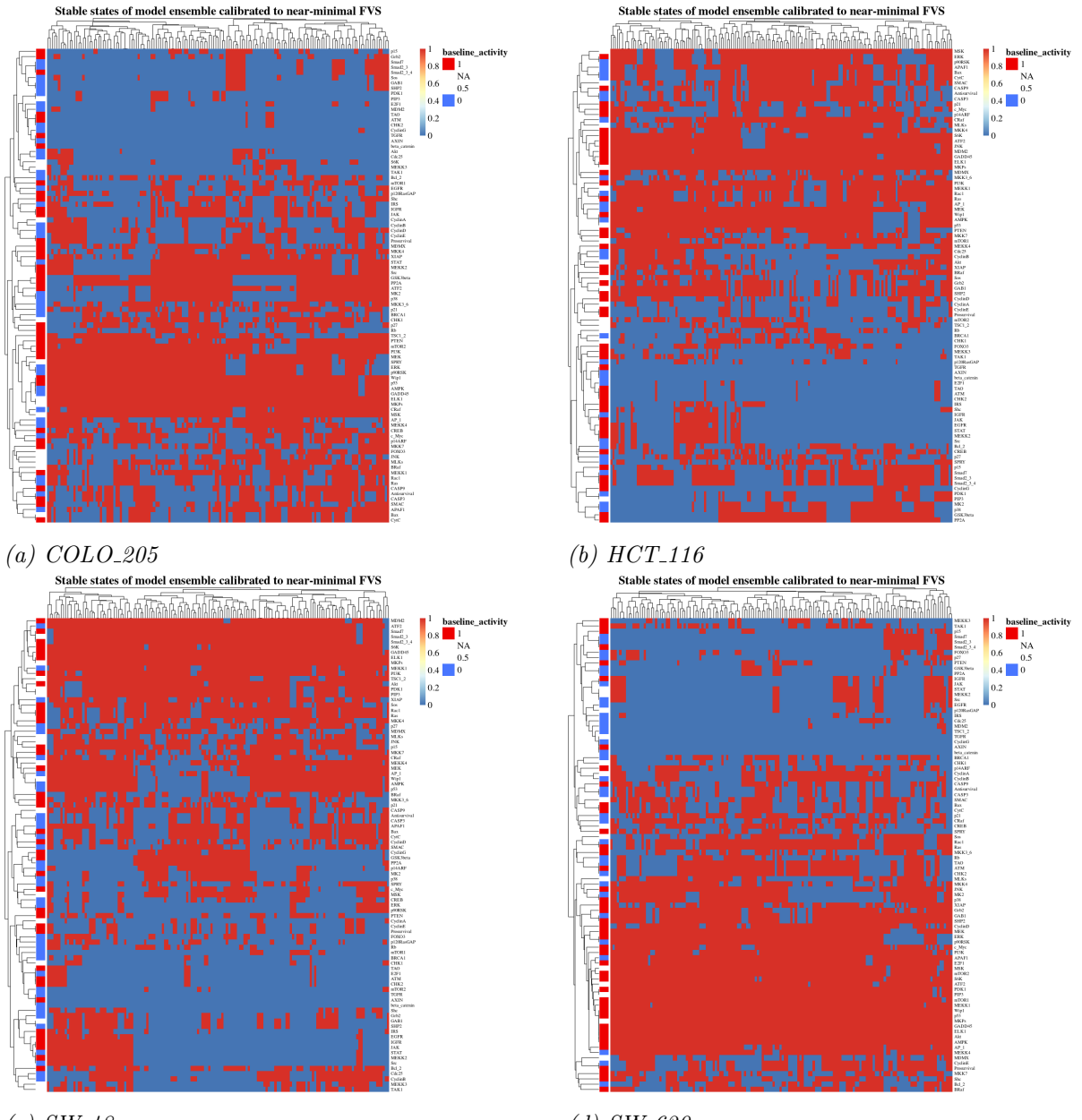

(a) COLO_205

(b) HCT_116

(c) SW_48

(d) SW_620

Figure 3.21. Model-wise stable state heatmap for the Park-model calibrated to a possible driver set based on a near-minimal FVS. Model nodes are represented by rows, and individual models in the calibrated model ensemble are represented by columns. The annotation row indicates the experimentally observed baseline activity of the (a) COLO_205, (b) HCT_116, (c) SW_48 and d) SW_620 cell line

The baseline compliance of the calibrated Park-model ranges from 0.501 to 0.649 (Table 3.5). The highest baseline compliance is observed for the SW_620 cell line.

Table 3.5. Compliance between the stable state of the Park-model, calibrated to a possible driver set based on a near-minimal FVS, and cell line specific baseline activity profiles.

Model	**Cell line**	**Baseline compliance**
Park	COLO_205	0.546
Park	HCT_116	0.501
Park	SW_48	0.538
Park	SW_620	0.649

The stable state of calibrated Lu-model has large areas of homogeneity and some areas of heterogeneity across model ensembles (Figure 3.22). The ensemble stable state of the Lu-model, calibrated to a near-minimal FVS sample of the SW_48 baseline activity profile, is homogeneous across all nodes, except the *Prosurvival* output node (Figure 3.22c).

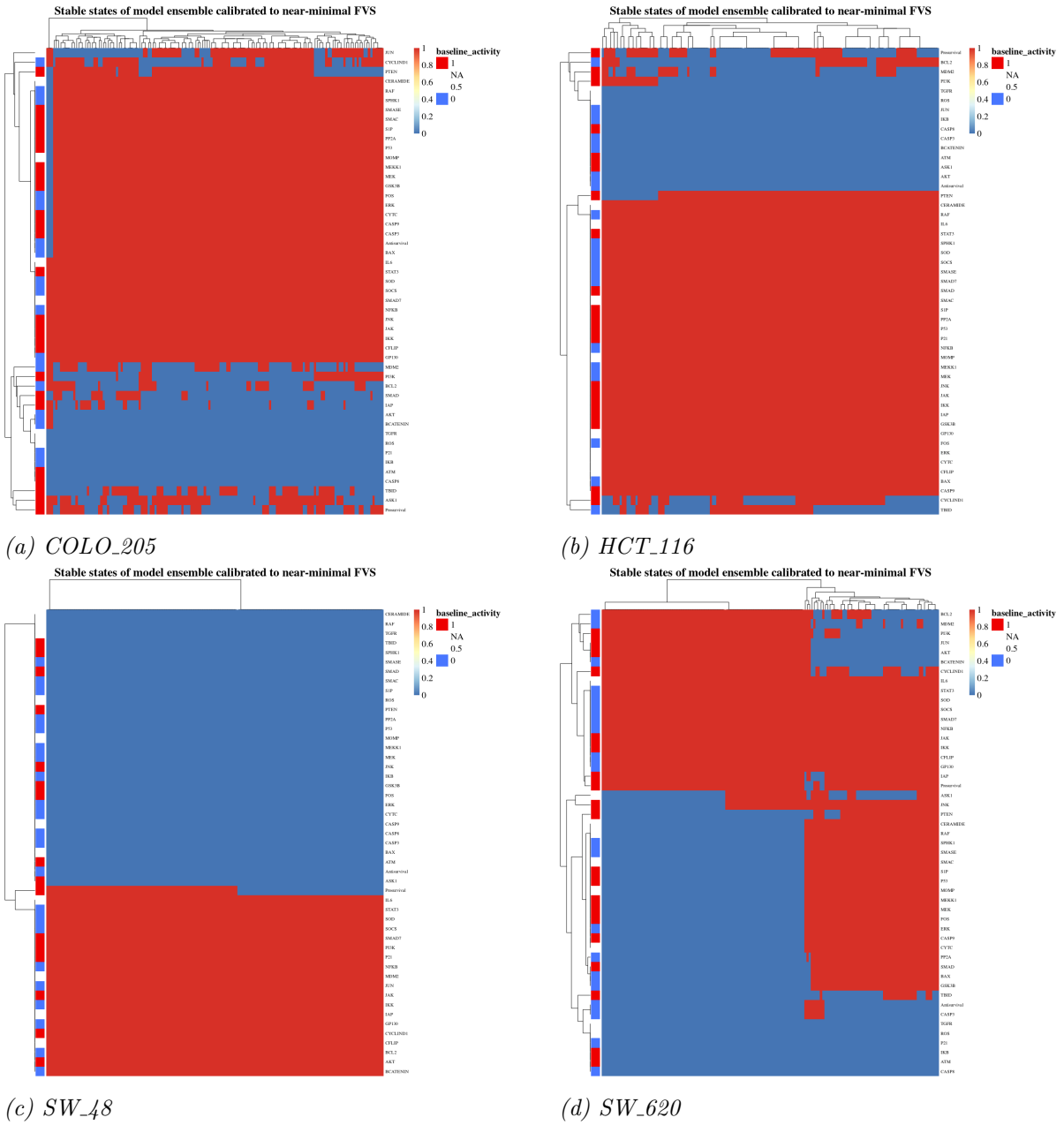

(a) COLO_205

(b) HCT_116

(c) SW_48

(d) SW_620

Figure 3.22. Model-wise stable state heatmap for the Lu-model calibrated to a possible driver set based on a near-minimal FVS. Model nodes are represented by rows, and individual models in the calibrated model ensemble are represented by columns. The annotation row indicates the experimentally observed baseline activity of the (a) COLO_205, (b) HCT_116, (c) SW_48 and d) SW_620 cell line

The baseline compliance of the calibrated Lu-model ranges from 0.475 to 0.580 (Table 3.6). The highest baseline compliance – of 0.580 – is observed for the COLO_205 cell line.

Table 3.6. Compliance between the stable state of the Lu-model, calibrated to a possible driver set based on a near-minimal FVS, and cell line specific baseline activity profiles.

Model	Cell line	Baseline compliance
Lu	COLO_205	0.580
Lu	HCT_116	0.548
Lu	SW_48	0.515
Lu	SW_620	0.475

3.5.4 A Driver-based Calibration Strategy does not Ensure a Calibrated Model with a Baseline Compliant Stable State

Three main observations are extracted from stable state results and will be discussed in the following sections. First of all, stable state results do not suggest that a driver set can be identified for CASCADE 1.0, Park-model and Lu-model – based on degree Z-score, DP, nor a near-minimal FVS – as the driver-based strategy does not ensure a calibrated model reflecting the cell line specific baseline activity. Secondly, the cell line specific topology of CASCADE 1.0 gives a higher baseline compliance compared to the generic CRC topologies of the Park- and Lu-models. It seems however, that there is some cell line specific bias in the network of the Park- and Lu-models as well, as a higher baseline compliance is observed for certain CRC cell lines compared to others. The last observation – which is discussed most thoroughly – relates to how certain topological characteristics and limitations affect the ability to obtain a calibrated model with a baseline compliant stable state.

No Driver Set is Identified Based on Degree Z-score, DP or a Near-minimal FVS

Neither degree Z-score, DP, nor a near-minimal FVS is identified as a superior measure for identification of a driver set in CASCADE 1.0, Park- and the Lu-model, as no overall baseline compliant state is observed for any calibrated model. In addition, the highest baseline compliance is generally observed when these models are calibrated to the complete baseline profile of a cell line, suggesting that the target state is not inferred from the state of the possible driver set.

These findings underpin that target control of complex networks is a very challenging task. There is no general dominating theory or strategy for successful control of large complex networks [7]. Even though Z-score, DP, and a near-minimal FVS cover node properties that would indicate a possible driver set, both the results from this project and previous scientific reports are not conclusive. Although hubs are central interaction points in scale-free networks, it is debated to what extent driver nodes tend to be high degree nodes. Guo et al. find, that in biological networks, driver nodes tend to be nodes with a high degree, while Liu et al., on the other hand, conclude that the number of

driver nodes is significantly larger among low-degree nodes in scale-free networks [28,46]. Matache and Matache, as well as Pentzien et al., find that knowledge about the activity of a subset of nodes with the highest DP reduces the uncertainty about the whole model state [50,62]. They do, however, not conclude that a DP-based subset of nodes provides full target control. Controlling the near-minimal FVS of a Boolean model should in theory be sufficient to drive the model into a target state, as it prevents multistability [55]. However, this target state needs to be one of the natural end states of the model. As previously mentioned, the possible model solution space is restricted by the topology of the input Boolean model, as it has finite number of possible stable states [67]. If the cell line specific baseline state is not in the state space of the model, it can not be reached, even by a sufficient driver set.

Differences in Baseline Compliance Suggests Cell Line Specific Bias in the Network Topology

The highest baseline compliance value of – 0.783 – is obtained by CASCADE 1.0, calibrated to the complete AGS baseline activity profile. The Park- and Lu-models are not able to reach this compliance level for any cell line specific baseline activity profile. This can be explained by the fact, that CASCADE 1.0 is a cell line specific AGS model, while both the Park- and Lu-models are only specific for the CRC cancer type [20,47,60]. The cell line specific topology of CASCADE 1.0 might be better at representing the cell line specific baseline activity of AGS, than the general CRC topology of the Park- and Lu-models are able to represent the cell line specific baseline activity profiles of COLO_205, HCT_116, SW_48 and SW_620. The level of baseline compliance obtained by model calibration of the Park- and Lu-models does, however, suggest that there might be some cell line specific bias in the topology of these networks as well. The highest baseline compliance for the Lu-model is observed when calibrated to the COLO_205 cell line, and ranges from 0.548 to 0.679. In comparison, the baseline compliance with the remaining cell lines is in the following range: HCT_116 [0.465, 0.604], SW_48 [0.447, 0.552] and SW_620 [0.410, 0.541]. The highest baseline compliance is obtained by the Park-model when calibrated to the SW_620 cell line, and ranges from 0.602 to 0.755. In comparison, the baseline compliance of the remaining cell lines is in the following range: COLO_205 [0.530, 0.670], HCT_116 [0.543, 0.715] and SW_48 [0.542, 0.693]. These results suggest, that even though these models are supposed to be generic CRC cell lines, they are better fit to represent the baseline activity of some CRC cell lines. No further analysis was conducted to identify which topological characteristics are causing this cell line bias.

Model Topology Limits the Ability to Reach a Baseline Compliant State

The driver-based calibration strategy applied in this project does not ensure maximal compliance between the stable state of calibrated models and the cell line specific baseline activity profiles. It can partly be because no true driver set is identified based on the selection of network measures. However, it is more likely caused by certain topological

characteristics restricting the possible model solution space during calibration.

CASCADE 1.0 does obtain a largely homogeneous stable state across the model ensemble, when calibrated to a 70% sample of AGS baseline activity data, based on degree Z-score or DP. However, this homogeneous stable state configuration does only have an overall baseline compliance of ~ 0.75. For some nodes, such as *MAP2K4*, *MAP3K11* and *MAP3K4*, the stable state activity violates the baseline activity. These nodes are defined as inactive in the AGS baseline activity profile, but are observed as active across stable states.

The logical equations of these nodes imply that MAP3K4, MAP3K11 and MAP2K4 are only regulated by activation:

MAP3K4: RAC_f

MAP3K11: RAC_f

MAP2K4: MAP3K4 | MAP3K11 | MAP3K7 | GRAP2

It is also evident, from these logical equations, that the activity of this node triplet is solely based on the activity of RAC_f, as it is the only activator of MAP3K4 and MAP3K11, which are sufficient activators of MAP2K4. This is an example of what Kauffman defines as *canalising Boolean functions* [39]. Canalising Boolean functions have the property that the activity of an input is sufficient to determine the activity of the output. In this case, the activity of RAC_f is sufficient to determine the activity of MAP3K4, MAP3K11, and MAP2K4. RAC_f is defined as active in the AGS baseline activity profile, while MAP3K4, MAP3K11, and MAP2K4 are defined as inactive. However, the activity of RAC_f and the inactivity of MAP3K4, MAP3K11, and MAP2K4 are not in accordance with the topology, due to the canalising functions, and is not a possible state in the model solution space of CASCADE 1.0.

Such inconsistencies between the model topology and the baseline activity profile need to be addressed, as it limits successful model calibration. There are two different approaches to this challenge, depending on whether the network topology or the baseline activity data is considered the most likely reflection of reality. The topology of the network can be changed to fit the baseline data, or the topology can be used to evaluate the accuracy of the baseline activity [29]. The activity of RAC_f is reported by several researchers, and was also considered by Flobak et al. as one of the main biomarkers of AGS [20, 33, 43]. MAP3K11 activity in gastric cancer is reported by Ramachandraiah et al., supporting the stable state configuration of CASCADE 1.0. However, Magnelli et al. report that MAP2K4 is mainly a tumour suppressor in gastric cancer, suggesting that inactivation promotes pathogenesis, which is more in accordance with the applied AGS baseline activity profile [48]. Such contradictions makes it evident that more research is needed to improve the consistency between CASCADE 1.0 and the AGS baseline activity profile.

Stable state heatmaps reveal notable heterogeneity across ensembles of the calibrated Park-model, suggesting that different stable states are reached by models in the ensemble. There seems to be a general increase in both stable state homogeneity and baseline compliance as larger samples of the baseline activity profile is added to the calibration datasets, suggesting that the Park-model is quite sensitive to the data included in the calibration dataset during model calibration. Even adding the the baseline data of nodes with the 10% lowest Z-score and DP gives an increase in baseline compliance. A much higher stable state homogeneity is observed for calibrated model stable states reached by the Lu-model, as 15 nodes are consistently observed as active or inactive across all calibrated Lu-models. This highly consistent state does, however, not reflect differences in baseline activity across cell lines, suggesting that the topology of the Lu-model is not able to adapt to cell line specific differences during model calibration.

Kauffman characterises Boolean networks as either *ordered*, *critical* or *chaotic* [39]. The stable state of an ordered model has a "frozen core" of nodes with a fixed state, and some additional "twinkling islands" of nodes which are able to change their activity. The stable state of an ordered network is robust, both to changes in the activity of certain nodes, and mutations to interactions or logical rules [70]. The stable state of a chaotic model, on the other hand, has a more flexible core, and is more sensitive to small changes in conditions. A model with a critical behaviour lies on the border between chaos and order, and is both robust and adaptive. The consistency observed in the stable states of the Lu-model indicates an ordered model structure, having a fixed node core, unaffected by the calibration data. The heterogeneity observed across stable states of the Park-model is more in accordance with the description of a chaotic Boolean model, as the model is able to reach a variety of stable states, and is sensitive to the content of the calibration dataset.

In a biological perspective, it is more likely that cellular systems are ordered or critical, as robustness to perturbations is an essential property of living cells [70]. Cancer cells are especially robust, as they are able to maintain proliferation despite perturbations [40]. Shmulevichet et al. analysed the underlying genetic network of the HeLa cervical cancer cell line, and concluded that these cells are either ordered or critical, but not chaotic [70]. Hence, in a biological perspective, the ordered behaviour of the Lu-model is more in accordance with the expected behaviour of a cancer model than the chaotic behaviour of the Park-model. In a model calibration perspective, however, some model flexibility is required for the model to adapt to the cell line specific baseline activity data, and to be able to reflect a baseline target state. An ordered network with a fixed core, such as the Lu-model, will not be able to adapt to any cell line specific baseline data that is different from the natural stable state of the model. The model needs to be sensitive to mutations introduced to the logical rules during model calibration, hence calling for a more chaotic model behaviour. No optimal trade-off between order and chaos is observed in the Lu- and Park-models, taking into account both the biological and the model calibration perspective. As previously mentioned, Kauffman presents a third model category, the

critical one, which lies on the border between order an chaos. It might be suspected that a high quality Boolean cancer model, both in terms of biological representation and model calibration potential, should possess such a critical behaviour. However, more research is required to make any further conclusions.

Overall, these results highlight how the process of model calibration is more a process of Boolean model refinement than a process of extensive Boolean model adaptation. If the baseline target state violates the feasible state space of the Boolean input model, no baseline compliant stable state can be reached, even by a driver set of nodes. A strategy for evaluating the compatibility between the baseline target state and the feasible state space of the Boolean model would be a valuable contribution to the process of model calibration. Measuring the *Hamming distance* (the similarity between two binary strings) [59] between the baseline target state and the stable state of the uncalibrated model could give a first indication of compatibility. Several computational methods have been presented to identify inconsistencies between experimental data and model topologies [30,51] and could be implemented in this model calibration framework as well.

3.6 Effect of Calibration Data Subsetting on Synergy Predictions

A calibrated model ensemble can be given as input for prediction of synergistic drug combinations, using the Drabme software module. It has previously been shown, by Niederdorfer et al., that calibrating a model to the baseline activity data of highly influential network nodes could improve predictive performance [56]. Highly influential nodes, or network driver nodes, are subsets of network nodes able to control the dynamic behaviour of the network, and drive the network into a target state [81]. Since driver nodes are able to control the dynamics of a network model, they will largely determine how the model reacts to drug perturbation simulations as well. Hence, correctly defining the activity of driver nodes during model calibration is thought to also ensure precise synergy predictions.

Niederdorfer et al. identified highly influential nodes through a series of *in silico* perturbation experiments [56]. Each network node was sequentially fixed at its state defined in the baseline activity profile, and at its inverted state. Each perturbation was followed by a synergy simulation, and those nodes whose inversion led to a change in synergy predictions, or caused the system to reach a cyclic attractor, were considered highly influential [56]. A downside of this strategy is the large number of simulations required to assess the influentiality of every network node. Given a network of n nodes, this strategy requires $n * 2$ pipeline simulations and is a rather tedious approach.

In this project, it is hypothesised, that calculating the degree Z-score and DP for every model node, as well as identifying and a near-minimal FVS, could serve as a possible strategy for identifying a driver set *a priori*, without the need of numerous dynamic

simulations. In the following section it is investigated if model calibration with respect to possible driver sets – based on degree Z-score, DP, and a near-minimal FVS – improve subsequent synergy predictions compared to random sample calibration.

3.6.1 Models Calibrated to Random Samples of Baseline Activity Data Reveal Possible Span of Predictive Performance

Random resampling was performed to assess the possible span of predictive performance for each Boolean model compared to a set of cell line specific gold standard synergies. For every Boolean model and cell line combinations, random resampling was applied to construct a variety of calibration dataset including random subsets of baseline activity data. Each sample was used as calibration dataset for model calibration, and subsequent synergy predictions were performed with each calibrated model ensemble. The AUC ROC was calculated for each calibrated model ensemble, indicating the predictive performance and the ability to correctly predict a set of experimentally verified gold standard synergies.

For CASCADE 1.0 and the AGS baseline activity profile, a large span of AUC ROC values is observed across all sample sizes (Figure 3.23). The largest variation is observed for samples sizes below 40%, where both AUC ROC values close to 1.0 and 0.0 are observed. For models calibrated to random baseline samples above 30%, there is a drop in the upper possible predictive performance below an AUC ROC of 0.7.

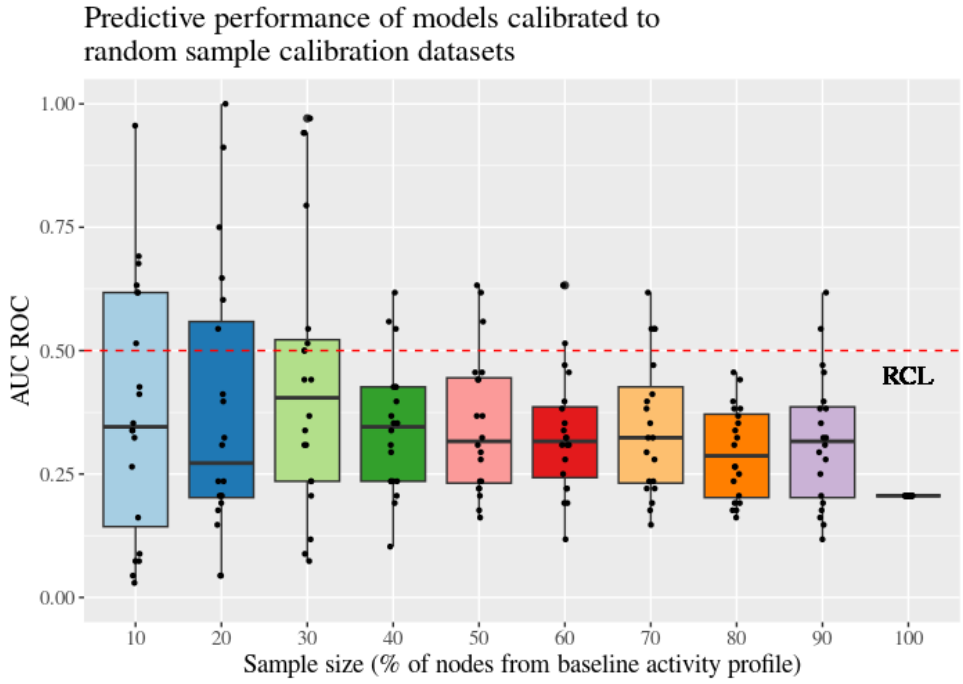

Figure 3.23. Predictive performance (AUC ROC) of CASCADE 1.0 calibrated to random samples of the AGS baseline activity profile. The x-axis gives the sample size, and the y-axis gives the corresponding AUC ROC value. The Random Chance Line (RCL) of classification is represented by a red line.

.

The possible span of AUC ROC values is narrower for the Park-model, compared to CASCADE 1.0, ranging from an AUC ROC of ∼0.25 to ∼0.75, across cell lines (Figure 3.24). No calibrated Park-model approaches a maximal AUC ROC of 1.0.

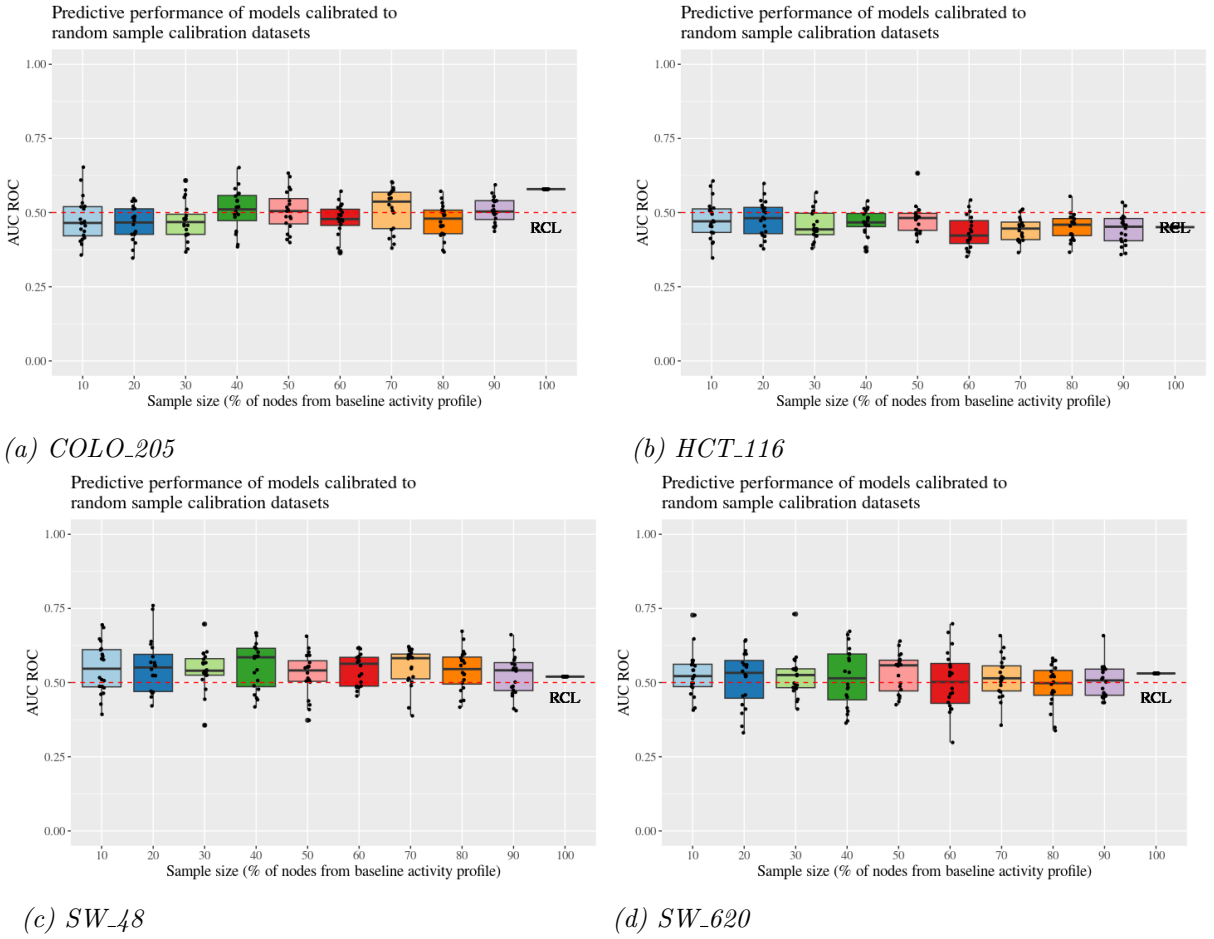

(a) COLO_205

(b) HCT_116

(c) SW_48

(d) SW_620

Figure 3.24. Predictive performance (AUC ROC) of the Park-model calibrated to random samples of the (a) COLO_205, (b) HCT_116, (c) SW_48, d) SW_620 baseline activity profiles. The x-axis gives the sample size, and the y-axis gives the corresponding AUC ROC value. The Random Chance Line (RCL) of classification is represented by a red line.

For the Lu-model, results differ between cell lines (Figure 3.25). The Interquartile Range (IQR) of AUC ROC values observed for the COLO_205 cell line, is below the RCL for all sample sizes. For the SW_620 cell line, on the other hand, most sample sizes have an IQR above the RCL. However, across all cell lines, AUC ROC values both above and below the RCL are observed for all samples sizes below 100%. An AUC ROC of 0.9 is obtained for the SW_620 cell line, but for all other cell lines, the predictive performance never exceeds an AUC ROC of 0.75.

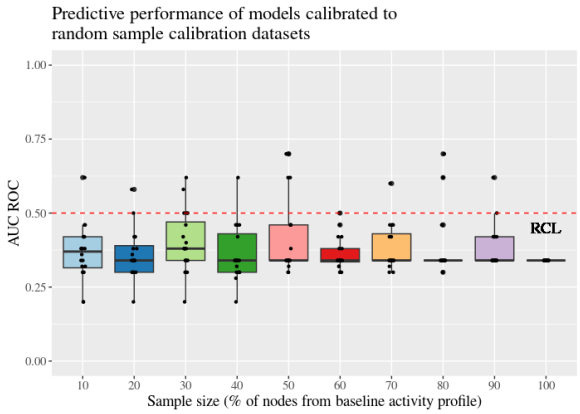

(a) COLO_205

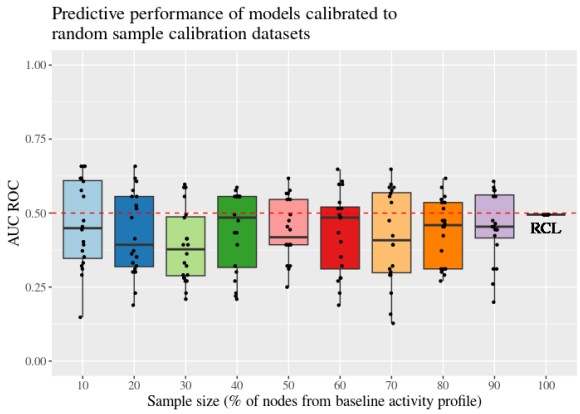

(b) HCT_116

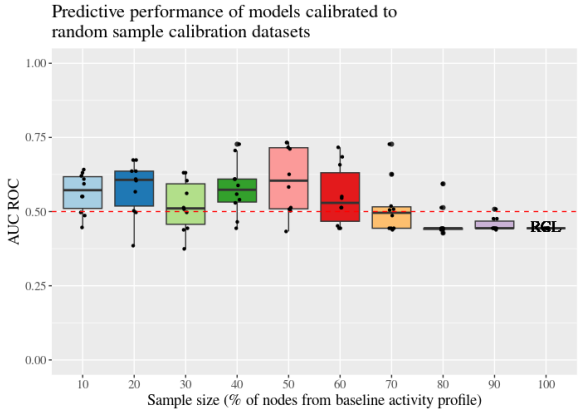

(c) SW_48

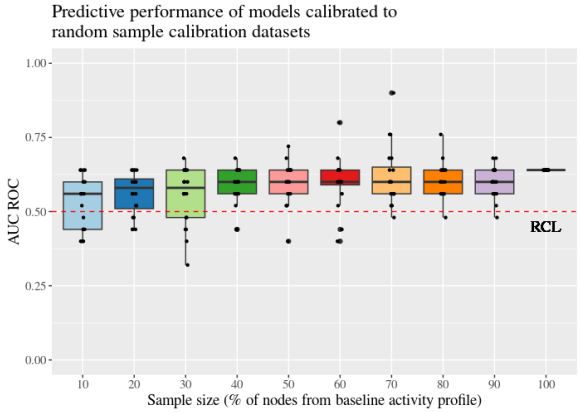

(d) SW_620

Figure 3.25. Predictive performance (AUC ROC) of the Lu-model calibrated to random samples of the (a) COLO_205, (b) HCT_116, (c) SW_48, d) SW_620 baseline activity profiles. The x-axis gives the sample size, and the y-axis gives the corresponding AUC ROC value. The Random Chance Line (RCL) of classification is represented by a red line.

For all model and cell line specific random resampling results, the AUC ROC and sample size of the worst and best performing models are provided in Table 3.7 and 3.8. Both best performing and worst performing models are calibrated to random samples below 80%. Across all models and cell lines, the best performing calibrated models have an AUC ROC above the RCL, which is considered better than a random synergy classifier.

Table 3.7. Overview of best performing models, calibrated to random samples of baseline activity data. For every model and cell line the AUC ROC closest to 1.000 is stated.

Model	**Cell line**	**AUC ROC**	**Sample size**
CASCADE 1.0	AGS	1.000	20
Lu	COLO_205	0.700	50, 80
Lu	HCT_116	0.658	10, 20
Lu	SW_48	0.733	50, 80
Lu	SW_620	0.900	70
Park	COLO_205	0.657	40
Park	HCT_116	0.633	50
Park	SW_48	0.760	20
Park	SW_620	0.731	30

Table 3.8. Overview of worst performing models, calibrated to random samples of baseline activity data. For every model and cell line the AUC ROC closest to 0.000 is stated.

Model	**Cell line**	**AUC ROC**	**Sample size**
CASCADE 1.0	AGS	0.029	10
Lu	COLO_205	0.200	10, 20, 30, 40
Lu	HCT_116	0.128	70
Lu	SW_48	0.374	30
Lu	SW_620	0.320	30
Park	COLO_205	0.347	20
Park	HCT_116	0.347	10
Park	SW_48	0.356	30
Park	SW_620	0.298	60

Two main conclusions can be drawn from these observations. First, across all sample sizes, we observe a variety of AUC ROC values. Two models calibrated to calibration datasets of equal sample size can obtain different levels of predictive performance, suggesting that the content of the calibration dataset is not arbitrary. The only difference between two calibration dataset of equal sample size is the identity and characteristics of the nodes included. Differences in predictive performance could be caused by the absence or presence of certain high impact nodes in the calibration datasets.

A second conclusion drawn from these results is that larger samples of baseline activity data included in the calibration data do not necessarily provide better predictive performance. The best predictive performance is generally observed for models calibrated to subsamples of baseline activity data. Across all combinations of models and cell lines, models calibrated to the complete baseline activity profile obtain an AUC ROC below or close to the RCL.

Calibrating a model with respect to a possible driver set, based on Z-score, DP, or near-minimal FVS, is in accordance with both of these observations. A driver set constitutes a subsample of baseline activity data, and includes nodes with high impact on model dynamics. Hence, it is in this project being tested as a strategy for constructing calibration datasets targeting models with high predictive performance, compared to random sampling.

3.6.2 Predictive Performance of Models Calibrated to Possible Driver Sets (Degree Z-score)

Models calibrated to possible driver sets, based on degree Z-score, are given as input to the Drabme module for synergy predictions. The AUC ROC is calculated for every calibrated model – as a measure of predictive performance – and compared against the predictive performance of models calibrated to random samples. An AUC ROC above the Interquartile Range (IQR) of the corresponding random sample results is considered an improvement of predictive performance.

Calibration of CASCADE 1.0, using a possible driver set (Z-score) with a sample size of 10% to 50%, obtains significantly improved predictive performance compared to random sampling (Figure 3.26). A maximal AUC ROC of 1.0 is obtained by CASCADE 1.0 when calibrated to a 10% sample. For models calibrated to samples above 50%, predictive performance falls below or within the IQR of random sample results.

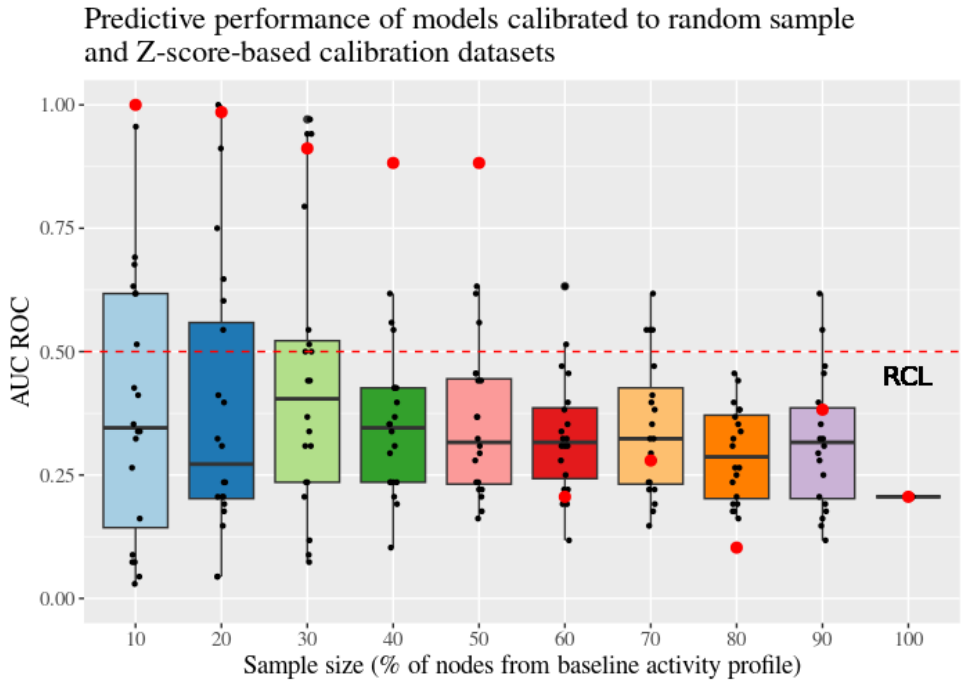

Figure 3.26. AUC ROC of CASCADE 1.0 calibrated to random samples of baseline activity data (black dots) and Z-score based samples of baseline activity data (red dots) for the AGS cell line. The x-axis indicates the sample size

.

The predictive performance obtained by the Park-model calibrated to possible driver sets (Z-score) differs across cell lines (Figure 3.27). For the COLO_205, HCT_116 and SW_48 cell lines, the AUC ROC falls mostly within and below, and sometimes above, the IQR of random sample results. For the SW_620 cell line, the AUC ROC never exceeds the IQR of random sample results.

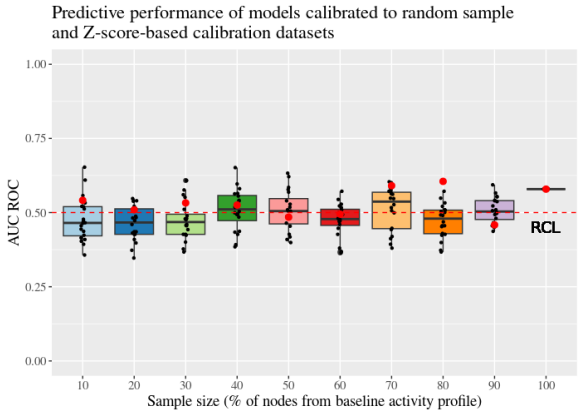

(a) COLO_205

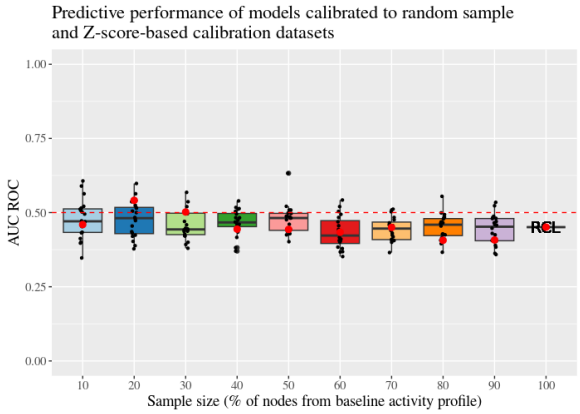

(b) HCT_116

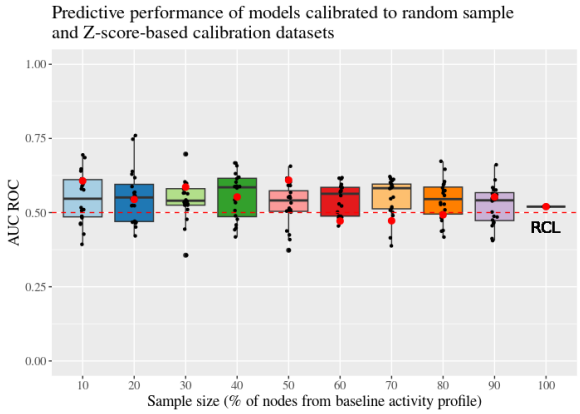

(c) SW_48

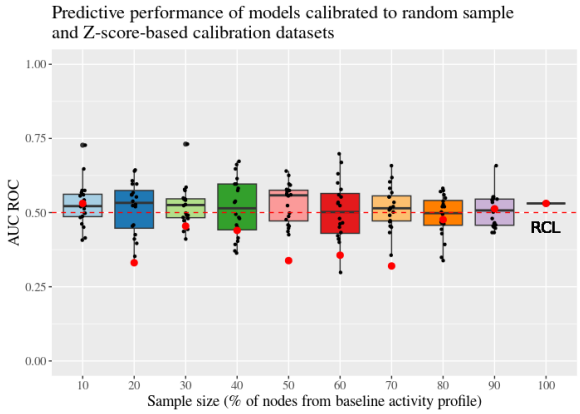

(d) SW_620

Figure 3.27. AUC ROC of Park-model calibrated to random samples of baseline activity data (black dots) and Z-score based samples of baseline activity data (red dots) for the (a) COLO_205, (b) HCT_116, (c) SW_48 and d) SW_620 cell line. The x-axis indicates the sample size.

As for the Park-model, great variation in predictive performance is observed for the Lu-model, calibrated to possible driver sets (Z-score) (Figure 3.28). For most calibrated models, the predictive performance falls within or below the IQR of random sample results. AUC ROC values above the IQR are only observed for the SW_48 cell line.

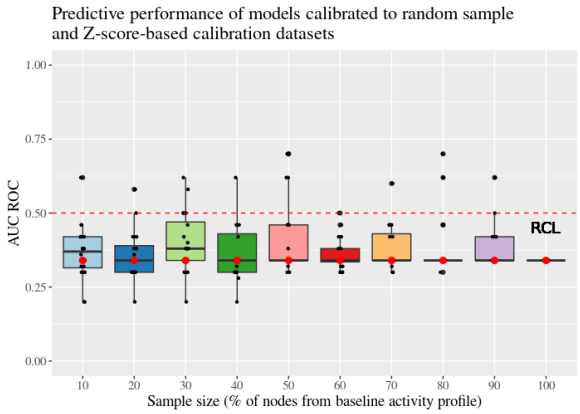

(a) COLO_205

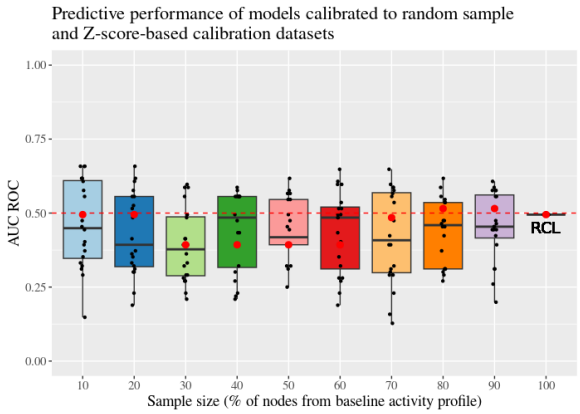

(b) HCT_116

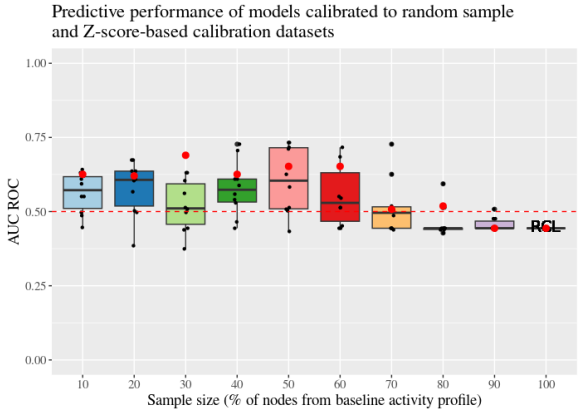

(c) SW_48

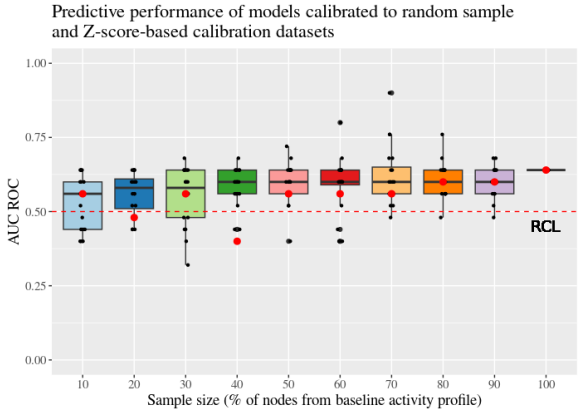

(d) SW_620

Figure 3.28. AUC ROC of Lu-model calibrated to random samples of baseline activity data (black dots), and Z-score based samples of baseline activity data (red dots) for the (a) COLO_205, (b) HCT_116, (c) SW_48 and d) SW_620 cell line. The x-axis indicates the sample size.

3.6.3 Predictive Performance of Models Calibrated to Possible Driver Sets (DP)

Models calibrated to possible driver sets, based on DP, were given as input to the Drabme pipeline module for synergy predictions. The AUC ROC was calculated for every calibrated model, as a measure of predictive performance, and compared against the predictive performance of models calibrated to random samples. An AUC ROC above the IQR of the corresponding random sample results is considered an improvement of predictive performance.

Calibration of CASCADE 1.0, using a possible driver set (DP) with a sample size of 10% to 50%, ensures an AUC ROC value above the IQR of corresponding random sample performance (Figure 3.29). As the DP based sample exceeds 50% of the baseline activity profile, predictive performance drops below the RCL and does not exceed the IQR of random sample performance.

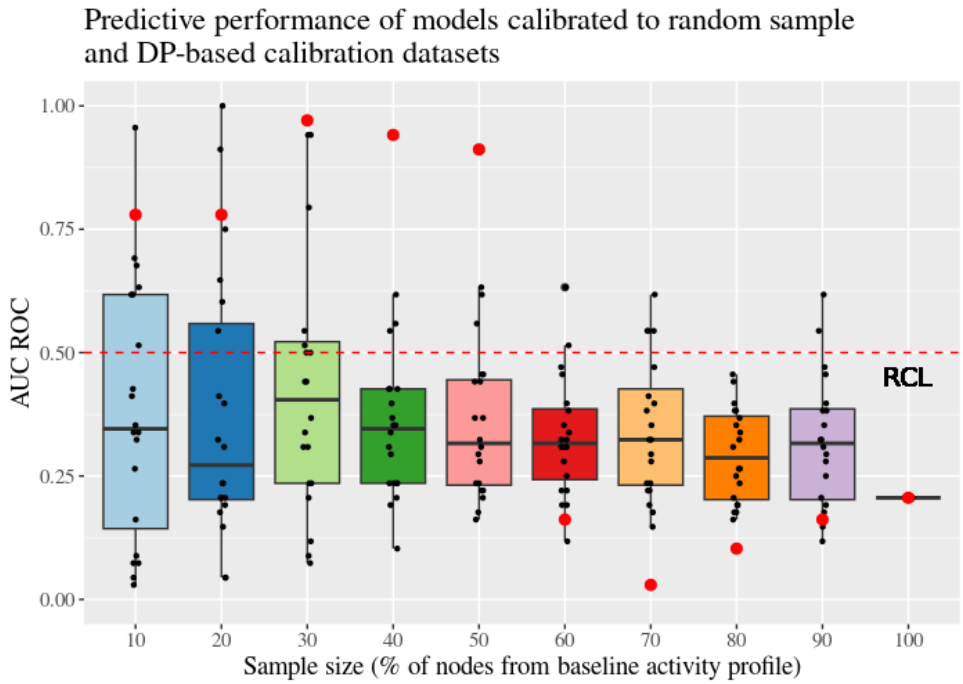

Figure 3.29. AUC ROC of CASCADE 1.0 calibrated to random samples of baseline activity data (black dots), and DP based samples of baseline activity data (red dots) for the AGS cell line. The x-axis indicates the sample size.

The Park-model calibrated to possible driver sets (DP) obtains an AUC ROC value both above, below and within the IQR of random sample performance. The upper AUC ROC value reached by models calibrated to random samples of baseline data, is not obtained by any model calibrated to a possible driver set.

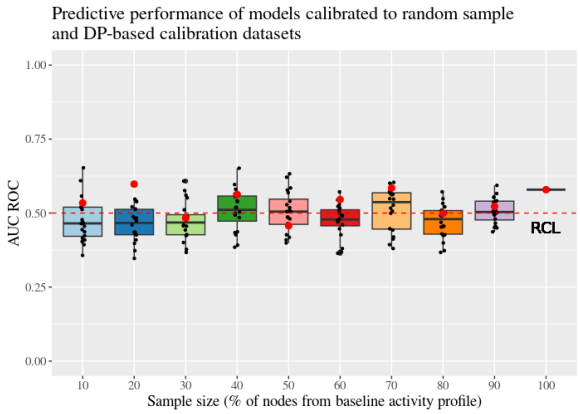

(a) COLO_205

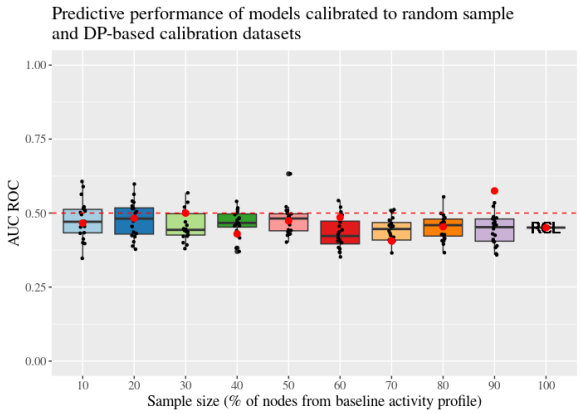

(b) HCT_116

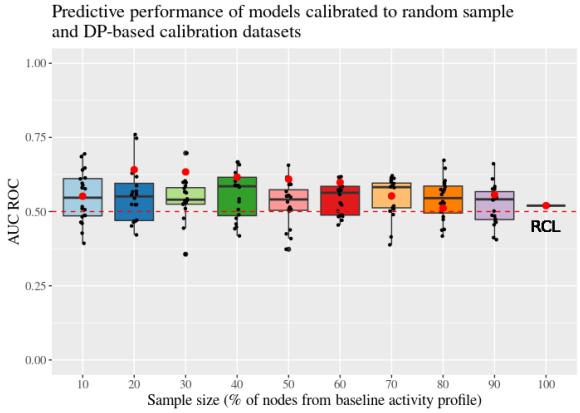

(c) SW_48

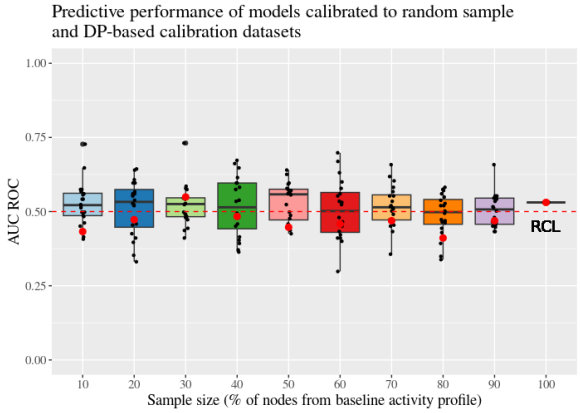

(d) SW_620

Figure 3.30. AUC ROC of Park-model calibrated to random samples of baseline activity data (black dots), and DP based samples of baseline activity data (red dots) for the (a) COLO_205, (b) HCT_116, (c) SW_48 and d) SW_620 cell line. The x-axis indicates the sample size.

The AUC ROC of the Lu-model calibrated to possible driver sets (DP) falls mostly within or below the IQR of random sample performance (Figure 3.31). Optimal predictive performance, reached by random sample calibration of the Lu-model, is not reached by any model calibrated to a possible driver set.

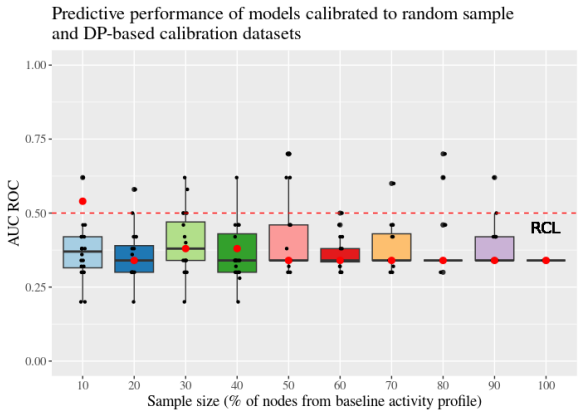

(a) COLO_205

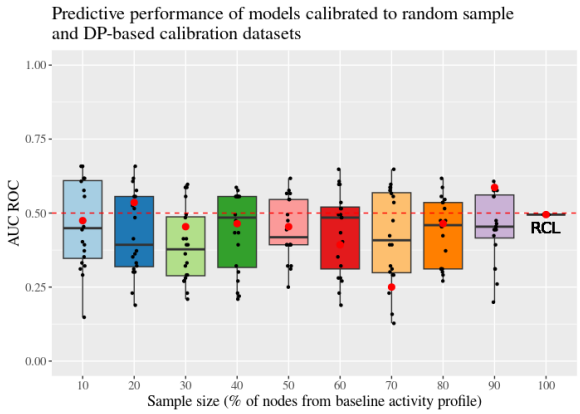

(b) HCT_116

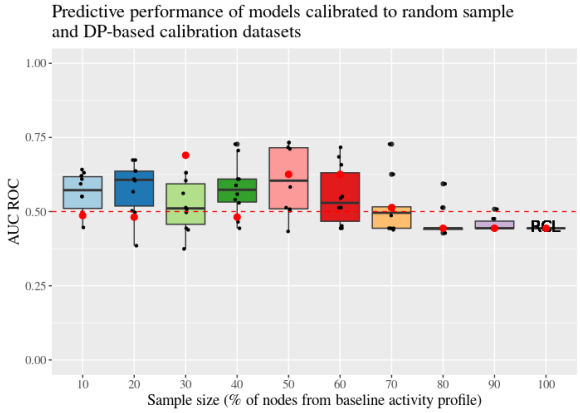

(c) SW_48

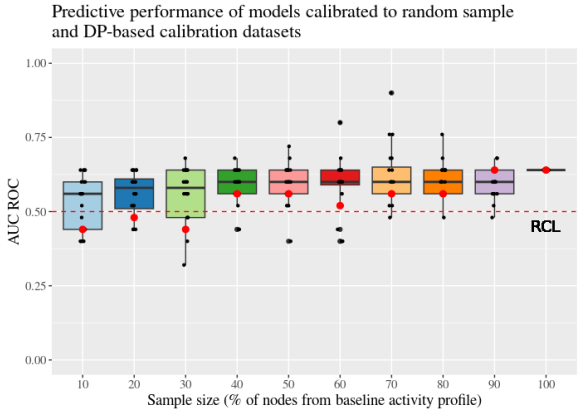

(d) SW_620

Figure 3.31. AUC ROC of Lu-model calibrated to random samples of baseline activity data (black dots), and DP based samples of baseline activity data (red dots) for the (a) COLO_205, (b) HCT_116, (c) SW_48 and d) SW_620 cell line. The x-axis indicates the sample size.

3.6.4 Predictive performance of models calibrated to a possible driver set (near-minimal FVS)

The AUC ROC of CASCADE 1.0 calibrated to a near-minimal FVS sample of baseline activity is above the IQR of random sample performance of similar sample size. (Table 3.9). The Park- and Lu-models calibrated to a near-minimal FVS sample obtain AUC ROC values both below, within and above the IQR of random sample performance, depending on the cell line. No calibrated model reaches the optimal predictive performance obtained by models calibrated to random samples.

Table 3.9. AUC ROC obtained by models calibrated to a possible driver set based on a near-minimal FVS. The IQR of AUC ROC values obtained by models calibrated to random samples of similar size is given as a comparison.

Model	Cell line	Sample size	AUC ROC	IQR of random sample AUC ROC (30%)
CASCADE 1.0	AGS	34	0.794	[0.235, 0.529]
Lu	COLO_205	31	0.300	[0.340, 0.480]
Lu	HCT_116	31	0.393	[0.286, 0.490]
Lu	SW_48	31	0.626	[0.444, 0.604]
Lu	SW_620	31	0.520	[0.480, 0.640]
Park	COLO_205	26	0.598	[0.427, 0.500]
Park	HCT_116	26	0.372	[0.425, 0.500]
Park	SW_48	26	0.581	[0.525, 0.583]
Park	SW_620	26	0.542	[0.482, 0.547]

3.6.5 Predictive Performance is Improved for CASCADE 1.0 when some Stable State Heterogeneity is Observed

The predictive performance of CASCADE 1.0 is improved, compared to random sampling, when calibrated to Z-score and DP based samples of the AGS baseline activity profile, below a 60% sample size. Adding more baseline data to the calibration dataset decreases the predictive performance significantly. Interestingly, this drop in predictive performance coincides with an increase in stable state homogeneity and baseline compliance observed in the stable state analysis. Comparing both stable state and predictive performance results, for CASCADE 1.0, it seems like an optimal model in terms of stable state homogeneity and baseline compliance is not the same as an optimal model in terms of predictive performance.

This observation questions one of the main assumptions of the DrugLogics framework, namely that a model reflecting the baseline activity of a cell line also correctly reflects synergistic and non-synergistic responses to drug combinations. In machine learning terms, this is known as *transfer learning* [17]. In traditional machine learning, both the training data, used to build the model, and the test data, applied to test model performance, is taken from the same feature space. However, in many real-world scenarios, the training and test data might have features representing different attributes. Hence, transfer learning involves building a model based on one feature set and using this model to make predictions on another feature set [17]. The applicability of transfer learning requires a relationship between the training and the test data domain. In the DrugLogics framework, it is assumed that the ability to correctly represent the baseline activity of a cell line ensures the ability to predict cell line specific drug synergies. However, in the case of CASCADE 1.0, this positive relationship between baseline compliance and predictive

performance is not observed.

This unexpected inconsistency between the baseline compliance and predictive performance of CASCADE 1.0 can be explained by the ensemble-wise approach applied in the DrugLogics framework. From model calibration, an ensemble of calibrated models is given as output. Drug perturbation simulations are performed on the whole model ensemble, and the predictive performance is calculated based on the average drug combination response across the ensemble [84]. An ensemble-based machine learning approach is shown to improve the predictive performance of a prediction model, as the combined performance of an ensemble of different imperfect models is better than the performance of one imperfect model [63], as exemplified in Figure 3.32.

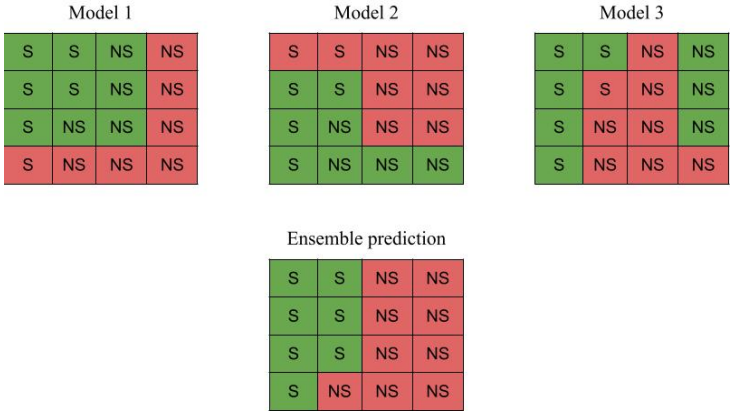

Figure 3.32. Illustrative representation of ensemble-wise prediction of synergies (S) and non-synergies (NS). Neither model 1, 2, nor 3 is able to correctly classify synergies and non-synergies, but the ensemble-wise prediction is in accordance with the true classification.

This strategy requires some diversity across the model ensemble, to ensure that different models make different errors. This error diversity will provide a lower error rate for the model ensemble combined, as the error of one model is compensated for by another. For CASCADE 1.0, a calibrated model ensemble with some stable state diversity is able to correctly predict most synergistic drug combinations in AGS, not necessarily because every individual model in the ensemble has an overall high predictive performance, but because the collective prediction effort of the ensemble is high.

3.6.6 Park- and Lu-models are not Able to Correctly Predict Synergies for CRC Cell Lines

Neither the Park-, nor the Lu-model is able to correctly predict all cell line specific drug synergies included in the gold standard synergy lists of the COLO_205, HCT_116, SW_48 and SW_620 cell lines. The predictive performance of the Park- and Lu-models, calibrated to random samples of baseline data, never approach an AUC ROC of 1.0, and no general improvement in predictive performance is observed for the Park- and Lu-models calibrated

to possible driver sets, based on degree Z-score, DP or a near-minimal FVS. No calibrated model is able to correctly discriminate between TP and FP synergistic drug combinations. This suggests, that the topology of the Park- and Lu-models do not reflect the dynamic response to combinatorial drug perturbations that is observed experimentally in the four CRC cell lines.

The topology of each CRC model has to be inspected individually to assess the possibility of model improvement. Folkesson et al. suggest three topological changes that can be introduced to a logical cancer model, to improve the ability to correctly predict synergistic drug combinations [22]. First, the logical rules of existing nodes can be altered. Logical rule adjustments were introduced to both CRC models in this project during model calibration, but were insufficient to obtain models with an AUC ROC close to 1.0. Folkesson et al. also suggest introducing additional nodes and additional edges, between existing nodes, to the model. Synergistic drug combinations act through certain molecular mechanisms [36, 41], and if these mechanisms are identified, missing interactions or nodes facilitating these effects can be added to the model.

CASCADE 1.0 was constructed specifically to represent AGS and predict synergistic drug responses in this cell line [20]. Park- and Lu-model, on the other hand, represent the generic signalling network in CRC and are not topologically adjusted to represent a specific cell line [47, 60]. Eduati et al. constructed a set of cell line specific logical models, for 14 different CRC cell lines, from a generic prior knowledge network [19]. They quantified the heterogeneity across these CRC cell line specific models and observed a lot of variability across major signalling pathways. Hence, it can be suspected, that such cell line specific differences need to be implemented in the model topology of the Park- and Lu-models as well, to improve their ability to correctly predict cell line specific drug synergies.

3.7 Further prospects

Some suggestions for further research and improvement of calibration data influence on model calibration and synergy predictions have been mentioned throughout this report, and are related to three main aspects: improvement of baseline activity inference, topological assessment of input model, and further investigation and identification of driver nodes.

First of all, new tools for activity inference from multi-omics data should be investigated, to improve the quality of the cell line specific baseline activity profiles. If the molecular profile used to define the target state during model calibration is erroneous, then the calibrated model will reflect these errors. The construction of baseline activity profiles, conducted in this report, was based on transcriptomic data. However, transcriptomic data is not a fully legitimate proxy for protein activity [52]. Genomic data in combination with proteomic data has been proposed as the most effective strategy for activity inference [68]. Hence, omics inference tools integrating both genomics and proteomics should be

considered for further research.

Secondly, results obtained in this report highlight, that both successful model calibration and synergy prediction is dependent on the network topology of the Boolean input model. If the target state for model calibration is not in the feasible state space of the input model, then no calibration strategy will be able to target this state. A strategy that allows to test the compatibility between the experimentally observed baseline target state and the topology of the network model – prior to model calibration – would be a valuable contribution to the DrugLogics framework. The same holds for successful synergy predictions. If no possible configuration of the input model is able to reflect the dynamic response to drug perturbations, observed *in vitro*, then no calibration strategy can resolve that issue. Hence, when such inconsistencies are discovered, larger topological modifications have to be made to improve predictive performance.

Lastly, even though no general driver set was identified using Z-score, DP, or a near-minimal FVS in this project, the notion of driver nodes and target control should be further investigated. For CASCADE 1.0, a driver-based calibration strategy was, in fact, able to improve predictive performance. However, the research has to be extended from purely stating *that* a calibration strategy improves predictive performance, to asking *why* this is the case, and how it can be extended to other models. Results also suggest, that a possible driver set can be unsuccessful in driving the calibrated model to a baseline compliant stable state, but successful in obtaining a calibrated model with high predictive performance. Hence, a goal dependent (baseline-compliant stable state versus predictive performance) strategy for driver set identification might be required.

Chapter 4

Conclusion

The main aim of this project was to identify a strategy for calibration dataset construction, that would improve model calibration of Boolean cancer models and drug synergy predictions.

The DrugLogics pipeline includes two software modules for calibration of Boolean models and combinatorial perturbation experiments. The model calibration module introduces changes to the logical rules of a Boolean input model, to obtain a calibrated ensemble of models whose stable state reflects an experimentally observed target state. The ensemble of calibrated models can be given as input to the synergy prediction module to assess the response to combinatorial perturbation experiments. In this project, the two software modules were used to calibrate three different Boolean cancer models, to make them compliant with a cell line specific baseline state. Combinatorial perturbation experiments – simulating the effect of targeted cancer drugs – were performed on the cell line specific calibrated models, to assess the ability to correctly identify cell line specific drug combinations with synergistic effect.

One of the main inputs given to the model calibration module was a *calibration dataset* including the experimentally observed baseline activity of genes and proteins in a cell line. It was hypothesised, that including the experimentally observed baseline activity for a set of *driver nodes* would be sufficient to obtain a calibrated model that correctly represents the complete baseline activity profile, as the state of the driver set determines the state of the whole network model. It was further hypothesised, that this driver-based calibration strategy would improve subsequent synergy predictions, as it is assumed, that a model correctly representing the baseline state of a cell line, would also correctly represent the response to targeted drug combinations. If the hypothesis is correct, then the process of inferring the experimentally observed baseline activity from omics data could be limited to the driver set of model nodes.

Three topological measures, *degree Z-score*, *Determinative Power* (DP) and a *near-minimal Feedback Vertex Set* (FVS), were used to identify possible driver sets in three Boolean cancer models: CASCADE 1.0 representing the AGS cell line of gastric cancer, the Park-

model representing *Colorectal Cancer* (CRC), and the Lu-model also representing CRC. Baseline activity profiles for AGS and four CRC cell lines were retrieved from omics data, and a collection of calibration datasets were constructed by sampling the baseline activity data with respect to the possible driver sets. These calibration datasets were further used as input for automated calibration of the selected Boolean cancer models.

The efficiency of the driver-based calibration strategy was assessed in terms of stable state homogeneity, and compliance between the stable state of the calibrated Boolean model ensemble and the cell line specific baseline activity profile. Overall, this driver-based strategy for model calibration did not ensure calibrated models reaching an overall baseline compliant stable state, as some stable state heterogeneity was observed for all calibrated models. Stable state results do suggest, that certain topological characteristics – inherent in the Boolean input models – limit the ability to obtain a calibrated model stable state with high baseline compliance. First of all, the compliance between the stable state of a calibrated model and the baseline activity profile is higher for some cell lines than others, suggesting that there might be some cell line specific bias in the topology of the input models. Secondly, large differences in topological flexibility were observed across the Boolean models. For some models, the activity of certain nodes was restricted to a single value, due to the presence of canalising functions, and an overall ordered model structure. If the activity of such fixed nodes is not in accordance with the cell line specific baseline profile, then there will be inconsistencies between the model stable state and the cell line specific baseline profile, which can not be resolved by any driver-based calibration strategy.

All calibrated models were further used as input for *in silico* drug synergy predictions, in order to assess how the driver-based calibration strategy affects the ability to correctly predict a set of cell line specific gold standard synergies, compared to models calibrated to random samples of baseline activity data. Overall, no general improvement in predictive performance was observed for the two CRC models, compared to random sampling. No calibrated version of these models – neither random, nor driver-based – was able to correctly predict all gold standard synergies. Hence, larger topological adjustments have to be made to improve their predictive performance. For CASCADE 1.0, some improvement in predictive performance was observed when calibrated to possible driver sets based on degree Z-score and DP, compared to random sample calibration. Interestingly, this improvement in predictive performance is observed for models with some heterogeneity across the stable states of the ensemble. This result could suggest, that the best performing model in terms of stable state homogeneity and baseline compliance is not necessarily the best model in terms of predictive performance. It also suggests, that the predictive error rate of an ensemble of diverse models would be lower than for an ensemble of similar models.

To further improve both model calibration and synergy predictions, several action areas should be further assessed. The process of baseline activity inference should integrate several omics data types, and topological characteristics limiting performance need to be

resolved. In addition, more insight into how possible driver sets improve performance in some models, and how it can be utilised in other models as well, constitute valuable next steps.

Bibliography

[1] Wassim Abou-Jaoud'e, Pauline Traynard, Pedro T Monteiro, Julio Saez-Rodriguez, Tomas Helikar, Denis Thieffry, and Claudine Chaouiya. Logical modeling and dynamical analysis of cellular networks. *Frontiers in genetics*, 7:94, 2016.

[2] Bissan Al-Lazikani, Udai Banerji, and Paul Workman. Combinatorial drug therapy for cancer in the post-genomic era. *Nature biotechnology*, 30(7):679–692, 2012.

[3] István Albert, Juilee Thakar, Song Li, Ranran Zhang, and Réka Albert. Boolean network simulations for life scientists. *Source code for biology and medicine*, 3(1):1–8, 2008.

[4] Reka Albert and Juilee Thakar. Boolean modeling: a logic-based dynamic approach for understanding signaling and regulatory networks and for making useful predictions. *Wiley Interdisciplinary Reviews: Systems Biology and Medicine*, 6(5):353–369, 2014.

[5] Shahnawaz Ali, Md Zubbair Malik, Soibam Shyamchand Singh, Keilash Chirom, Romana Ishrat, and RK Brojen Singh. Exploring novel key regulators in breast cancer network. *PLoS One*, 13(6):e0198525, 2018.

[6] Mariano J Alvarez, Yao Shen, Federico M Giorgi, Alexander Lachmann, B Belinda Ding, B Hilda Ye, and Andrea Califano. Network-based inference of protein activity helps functionalize the genetic landscape of cancer. *Nature genetics*, 48(8):838, 2016.

[7] Yazdan Asgari, Ali Salehzadeh-Yazdi, Falk Schreiber, and Ali Masoudi-Nejad. Controllability in cancer metabolic networks according to drug targets as driver nodes. *PLoS One*, 8(11):e79397, 2013.

[8] Keith Ashman and Elena López Villar. Phosphoproteomics and cancer research. *Clinical and Translational Oncology*, 11:356–362, 2009.

[9] Pau Badia-i Mompel, Jesús Vélez Santiago, Jana Braunger, Celina Geiss, Daniel Dimitrov, Sophia Müller-Dott, Petr Taus, Aurelien Dugourd, Christian H Holland, Ricardo O Ramirez Flores, et al. decoupler: ensemble of computational methods to infer biological activities from omics data. *Bioinformatics Advances*, 2(1):vbac016, 2022.

[10] Albert-Laszlo Barabasi and Zoltan N Oltvai. Network biology: understanding the cell's functional organization. *Nature reviews genetics*, 5(2):101–113, 2004.

[11] Albert-László Barabási and Márton Pósfai. *Network science*. Cambridge University Press, Cambridge, 2016.

[12] Jonas Béal, Lorenzo Pantolini, Vincent Noël, Emmanuel Barillot, and Laurence Calzone. Personalized logical models to investigate cancer response to braf treatments in melanomas and colorectal cancers. *PLoS Computational Biology*, 17(1):e1007900, 2021.

[13] Jane V Carter, Jianmin Pan, Shesh N Rai, and Susan Galandiuk. Roc-ing along: Evaluation and interpretation of receiver operating characteristic curves. *Surgery*, 159(6):1638–1645, 2016.

[14] Webster K Cavenee and Raymond L White. The genetic basis of cancer. *Scientific American*, 272(3):72–79, 1995.

[15] Di Chen, Xi Liu, Yiping Yang, Hongjun Yang, and Peng Lu. Systematic synergy modeling: understanding drug synergy from a systems biology perspective. *BMC systems biology*, 9(1):1–10, 2015.

[16] Pedro R Cutillas. Role of phosphoproteomics in the development of personalized cancer therapies. *PROTEOMICS–Clinical Applications*, 9(3-4):383–395, 2015.

[17] Oscar Day and Taghi M Khoshgoftaar. A survey on heterogeneous transfer learning. *Journal of Big Data*, 4:1–42, 2017.

[18] Kenneth De Jong. Learning with genetic algorithms: An overview. *Machine learning*, 3(2):121–138, 1988.

[19] Federica Eduati, Victoria Doldàn-Martelli, Bertram Klinger, Thomas Cokelaer, Anja Sieber, Fiona Kogera, Mathurin Dorel, Mathew J Garnett, Nils Blüthgen, and Julio Saez-Rodriguez. Drug resistance mechanisms in colorectal cancer dissected with cell type–specific dynamic logic models. *Cancer research*, 77(12):3364–3375, 2017.

[20] Åsmund Flobak, Anaïs Baudot, Elisabeth Remy, Liv Thommesen, Denis Thieffry, Martin Kuiper, and Astrid Lægreid. Discovery of drug synergies in gastric cancer cells predicted by logical modeling. *PLoS computational biology*, 11(8):e1004426, 2015.

[21] Å. Flobak, J. Zobolas, M. Vazquez, T. S. Steigedal, L. Thommesen, A. Grislingås, B. Niederdorfer, E. Folkesson, and M Kuiper. Logical modeling: Combining manual curation and automated parameterization to predict drug synergies. *BioRxiv*, 2021.

[22] Evelina Folkesson, B Cristoffer Sakshaug, Andrea D Hoel, Geir Klinkenberg, and Åsmund Flobak. Synergistic effects of complex drug combinations in colorectal cancer cells predicted by logical modelling. *Frontiers in Systems Biology*, 3:12, 2023.

[23] Julie Foucquier and Mickael Guedj. Analysis of drug combinations: current methodological landscape. *Pharmacology Research & Perspectives*, 3(3):e00149, 2015.

[24] Machtelt Garrels. *Bash Guide for Beginners*. Fultus Corporation, 2010.

[25] Jennifer Golbeck. *Chapter 3 - Network Structure and Measures*. Morgan Kaufmann, 2013.

[26] John J Grefenstette. Genetic algorithms and machine learning. In *Proceedings of the sixth annual conference on Computational learning theory*, pages 3–4, 1993.

[27] Roger Guimera and Luís A Nunes Amaral. Functional cartography of complex metabolic networks. *nature*, 433(7028):895–900, 2005.

[28] Wei-Feng Guo, Shao-Wu Zhang, Qian-Qian Shi, Cheng-Ming Zhang, Tao Zeng, and Luonan Chen. A novel algorithm for finding optimal driver nodes to target control complex networks and its applications for drug targets identification. *BMC genomics*, 19:67–79, 2018.

[29] Rosa Maria Gutierrez-Rios, David A Rosenblueth, Jose Antonio Loza, Araceli M Huerta, Jeremy D Glasner, Fred R Blattner, and Julio Collado-Vides. Regulatory network of escherichia coli: consistency between literature knowledge and microarray profiles. *Genome research*, 13(11):2435–2443, 2003.

[30] Carito Guziolowski, Annabel Bourdé, Francois Moreews, and Anne Siegel. Bioquali cytoscape plugin: analysing the global consistency of regulatory networks. *BMC genomics*, 10(1):1–11, 2009.

[31] Douglas Hanahan and Robert A Weinberg. Hallmarks of cancer: the next generation. *cell*, 144(5):646–674, 2011.

[32] Leland H Hartwell, John J Hopfield, Stanislas Leibler, and Andrew W Murray. From molecular to modular cell biology. *Nature*, 402(Suppl 6761):C47–C52, 1999.

[33] Hsieh-Hsun Ho, Chi-Sen Chang, Wei-Chi Ho, Sheng-You Liao, Wea-Lung Lin, and Chau-Jong Wang. Gallic acid inhibits gastric cancer cells metastasis and invasive growth via increased expression of rhob, downregulation of akt/small gtpase signals and inhibition of nf-κb activity. *Toxicology and Applied Pharmacology*, 266(1):76–85, 2013.

[34] Wenpin Hou, Peiying Ruan, Wai-Ki Ching, and Tatsuya Akutsu. On the number of driver nodes for controlling a boolean network when the targets are restricted to attractors. *Journal of theoretical biology*, 463:1–11, 2019.

[35] Patricia Jaaks, Elizabeth A Coker, Daniel J Vis, Olivia Edwards, Emma F Carpenter, Simonetta M Leto, Lisa Dwane, Francesco Sassi, Howard Lightfoot, Syd Barthorpe, et al. Effective drug combinations in breast, colon and pancreatic cancer cells. *Nature*, 603(7899):166–173, 2022.

[36] Jia Jia, Feng Zhu, Xiaohua Ma, Zhiwei W Cao, Yixue X Li, and Yu Zong Chen. Mechanisms of drug combinations: interaction and network perspectives. *Nature reviews Drug discovery*, 8(2):111–128, 2009.

[37] Won Duk Joo, Irene Visintin, and Gil Mor. Targeted cancer therapy–are the days of systemic chemotherapy numbered? *Maturitas*, 76(4):308–314, 2013.

[38] Sourabh Katoch, Sumit Singh Chauhan, and Vijay Kumar. A review on genetic algorithm: past, present, and future. *Multimedia Tools and Applications*, 80(5):8091–8126, 2021.

[39] Stuart A Kauffman. *Origins of order in evolution: self-organization and selection in evolution*. Oxford University Press, 1993.

[40] Hiroaki Kitano. Cancer robustness: tumour tactics. *Nature*, 426(6963):125–125, 2003.

[41] Hiroaki Kitano. A robustness-based approach to systems-oriented drug design. *Nature reviews Drug discovery*, 6(3):202–210, 2007.

[42] Rajeev Kumar and Abhaya Indrayan. Receiver operating characteristic (roc) curve for medical researchers. *Indian pediatrics*, 48:277–287, 2011.

[43] Yi-Chieh Lee, Tsan-Hwang Cheng, Jung-Shin Lee, Jiun-Hwan Chen, Yi-Chen Liao, Yao Fong, Cheng-Hsun Wu, and Yuan-Wei Shih. Nobiletin, a citrus flavonoid, suppresses invasion and migration involving fak/pi3k/akt and small gtpase signals in human gastric adenocarcinoma ags cells. *Molecular and cellular biochemistry*, 347:103–115, 2011.

[44] Xiangyi Li, Guangrong Qin, Qingmin Yang, Lanming Chen, and Lu Xie. Biomolecular network-based synergistic drug combination discovery. *BioMed research international*, 2016, 2016.

[45] Xiangrong Liu, Zengyan Hong, Juan Liu, Yuan Lin, Alfonso Rodríguez-Patón, Quan Zou, and Xiangxiang Zeng. Computational methods for identifying the critical nodes in biological networks. *Briefings in bioinformatics*, 21(2):486–497, 2020.

[46] Yang-Yu Liu, Jean-Jacques Slotine, and Albert-László Barabási. Controllability of complex networks. *nature*, 473(7346):167–173, 2011.

[47] Junyan Lu, Hanlin Zeng, Zhongjie Liang, Limin Chen, Liyi Zhang, Hao Zhang, Hong Liu, Hualiang Jiang, Bairong Shen, Ming Huang, et al. Network modelling reveals the mechanism underlying colitis-associated colon cancer and identifies novel combinatorial anti-cancer targets. *Scientific reports*, 5(1):14739, 2015.

[48] Lucia Magnelli, Nicola Schiavone, Fabio Staderini, Alessio Biagioni, and Laura Papucci. Map kinases pathways in gastric cancer. *International Journal of Molecular Sciences*, 21(8):2893, 2020.

[49] Loredana Martignetti, Laurence Calzone, Eric Bonnet, Emmanuel Barillot, and Andrei Zinovyev. Roma: representation and quantification of module activity from target expression data. *Frontiers in genetics*, 7:18, 2016.

[50] Mihaela T Matache and Valentin Matache. Logical reduction of biological networks to their most determinative components. *Bulletin of mathematical biology*, 78:1520–1545, 2016.

[51] Ioannis N Melas, Regina Samaga, Leonidas G Alexopoulos, and Steffen Klamt. Detecting and removing inconsistencies between experimental data and signaling network topologies using integer linear programming on interaction graphs. *PLoS computational biology*, 9(9):e1003204, 2013.

[52] Rafael Moreno-Sánchez, Emma Saavedra, Juan Carlos Gallardo-Pérez, Franklin D Rumjanek, and Sara Rodríguez-Enríquez. Understanding the cancer cell phenotype beyond the limitations of current omics analyses. *The FEBS journal*, 283(1):54–73, 2016.

[53] Jeffrey A Moscow, Tito Fojo, and Richard L Schilsky. The evidence framework for precision cancer medicine. *Nature Reviews Clinical Oncology*, 15(3):183–192, 2018.

[54] Aurélien Naldi. Biolqm: a java toolkit for the manipulation and conversion of logical qualitative models of biological networks. *Frontiers in physiology*, 9:1605, 2018.

[55] Eli Newby, Jorge Gómez Tejeda Zañudo, and Réka Albert. Structure-based approach to identifying small sets of driver nodes in biological networks. *Chaos: An Interdisciplinary Journal of Nonlinear Science*, 32(6):063102, 2022.

[56] Barbara Niederdorfer, Vasundra Touré, Miguel Vazquez, Liv Thommesen, Martin Kuiper, Astrid Lægreid, and Åsmund Flobak. Strategies to enhance logic modeling-based cell line-specific drug synergy prediction. *Frontiers in Physiology*, 11:862, 2020.

[57] Kivilcim Ozturk, Michelle Dow, Daniel E Carlin, Rafael Bejar, and Hannah Carter. The emerging potential for network analysis to inform precision cancer medicine. *Journal of molecular biology*, 430(18):2875–2899, 2018.

[58] Bernhard Palsson. *Systems biology*. Cambridge university press, 2015.

[59] Francesco Pappalardo, Cristiano Calonaci, Marzio Pennisi, Emilio Mastriani, and Santo Motta. Hamfast: fast hamming distance computation. In *2009 WRI World Congress on Computer Science and Information Engineering*, volume 1, pages 569–572. IEEE, 2009.

[60] Sang-Min Park, Chae Young Hwang, Jihye Choi, Chang Young Joung, and Kwang-Hyun Cho. Feedback analysis identifies a combination target for overcoming adaptive resistance to targeted cancer therapy. *Oncogene*, 39(19):3803–3820, 2020.

[61] Georgios A Pavlopoulos, Maria Secrier, Charalampos N Moschopoulos, Theodoros G Soldatos, Sophia Kossida, Jan Aerts, Reinhard Schneider, and Pantelis G Bagos. Using graph theory to analyze biological networks. *BioData mining*, 4(1):1–27, 2011.

[62] Trevor Pentzien, Bhanwar L Puniya, Tomáš Helikar, and Mihaela T Matache. Identification of biologically essential nodes via determinative power in logical models of cellular processes. *Frontiers in Physiology*, 9:1185, 2018.

[63] R. Polikar. Ensemble based systems in decision making. *IEEE Circuits and Systems Magazine*, 6(3):21–45, 2006.

[64] Bruce AJ Ponder. Cancer genetics. *Nature*, 411(6835):336–341, 2001.

[65] Sue Povey, Ruth Lovering, Elspeth Bruford, Mathew Wright, Michael Lush, and Hester Wain. The hugo gene nomenclature committee (hgnc). *Human genetics*, 109:678–680, 2001.

[66] Sundaramoorthy Revathidevi and Arasambattu Kannan Munirajan. Akt in cancer: mediator and more. In *Seminars in cancer biology*, volume 59, pages 80–91. Elsevier, 2019.

[67] Julian D Schwab, Silke D Kühlwein, Nensi Ikonomi, Michael Kühl, and Hans A Kestler. Concepts in boolean network modeling: What do they all mean? *Computational and structural biotechnology journal*, 18:571–582, 2020.

[68] Daniela Senft, Mark DM Leiserson, Eytan Ruppin, and A Ronai Ze'ev. Precision oncology: the road ahead. *Trends in molecular medicine*, 23(10):874–898, 2017.

[69] Paul Shannon, Andrew Markiel, Owen Ozier, Nitin S Baliga, Jonathan T Wang, Daniel Ramage, Nada Amin, Benno Schwikowski, and Trey Ideker. Cytoscape: a software environment for integrated models of biomolecular interaction networks. *Genome research*, 13(11):2498–2504, 2003.

[70] Ilya Shmulevich, Stuart A Kauffman, and Maximino Aldana. Eukaryotic cells are dynamically ordered or critical but not chaotic. *Proceedings of the National Academy of Sciences*, 102(38):13439–13444, 2005.

[71] Basavaradhya Sahukar Shruthi, Palani Vinodhkumar, et al. Proteomics: A new perspective for cancer. *Advanced biomedical research*, 5, 2016.

[72] Stanislaw Supplitt, Pawel Karpinski, Maria Sasiadek, and Izabela Laczmanska. Current achievements and applications of transcriptomics in personalized cancer medicine. *International Journal of Molecular Sciences*, 22(3):1422, 2021.

[73] Anthony Trewavas. A brief history of systems biology: "every object that biology studies is a system of systems." francois jacob (1974). *The Plant Cell*, 18(10):2420–2430, 2006.

[74] Dieudonne van der Meer, Syd Barthorpe, Wanjuan Yang, Howard Lightfoot, Caitlin Hall, James Gilbert, Hayley E Francies, and Mathew J Garnett. Cell model passports—a hub for clinical, genetic and functional datasets of preclinical cancer models. *Nucleic acids research*, 47(D1):D923–D929, 2019.

[75] Neil Vasan, José Baselga, and David M Hyman. A view on drug resistance in cancer. *Nature*, 575(7782):299–309, 2019.

[76] Neil Vasan, José Baselga, and David M Hyman. A view on drug resistance in cancer. *Nature*, 575(7782):299–309, 2019.

[77] Charles J Vaske, Stephen C Benz, J Zachary Sanborn, Dent Earl, Christopher Szeto, Jingchun Zhu, David Haussler, and Joshua M Stuart. Inference of patient-specific pathway activities from multi-dimensional cancer genomics data using paradigm. *Bioinformatics*, 26(12):i237–i245, 2010.

[78] Mengyuan Wang, Haiying Wang, and Huiru Zheng. A mini review of node centrality metrics in biological networks. *International Journal of Network Dynamics and Intelligence*, 1(1):99–110, 2022.

[79] Rui-Sheng Wang, Assieh Saadatpour, and Reka Albert. Boolean modeling in systems biology: an overview of methodology and applications. *Physical biology*, 9(5):055001, 2012.

[80] Helen V Warner, Nikita Sivakumar, Shayn M Peirce, and Matthew J Lazzara. Multiscale computational models of cancer. *Current Opinion in Biomedical Engineering*, 11:137–144, 2019.

[81] Felix M Weidner, Julian D Schwab, Silke D Werle, Nensi Ikonomi, Ludwig Lausser, and Hans A Kestler. Capturing dynamic relevance in boolean networks using graph theoretical measures. *Bioinformatics*, 37(20):3530–3537, 2021.

[82] Gang Yang, Jorge Gómez Tejeda Zañudo, and Réka Albert. Target control in logical models using the domain of influence of nodes. *Frontiers in physiology*, page 454, 2018.

[83] John Zobolas. *usefun: A Collection of Useful Functions by John*, 2020.

[84] John Zobolas. *Tutorial for synergy prediction using the DrugLogics software pipeline*, 2022.

Appendix A

Pipeline Configuration File

The pipeline configuration file includes global, Gitsbe-specific, and Drabme-specific parameter specifications. The following parameter specifications were applied in this report.

A.1 Global configurations

verbosity was set to 3, to save all logging messages produced by Gitsbe and Drabme. If necessary these could be used to trace back the execution of certain pipeline analyses.

delete_tmp_files and *compress_log_and_tmp_files* was set to TRUE, to avoid saving all temporary files produced during simulations and save storage.

use_parallel_sim was set to TRUE to allow parallel simulations. This configuration option allows faster simulations, due to the use of several processor cores. The maximal number of simulations was usually set to 4, using the *parallel_sim_num* option in the configuration file. When running the pipeline using an external server, the *parallel_sim_num* was changed to adjust to the number of processor cores available.

The *attractor_tool* was set to biolqm_stable_states. This tool calculates all the fixpoints of the models.

A.2 Gitsbe specific configurations

remove_output _nodes was set to FALSE and *remove_input _nodes* was set to TRUE, to ensure self-contained models. Output nodes are not removed because these represent phenotypic outcomes, which are very relevant for further perturbation analyses with Drabme.

The only relevant export format in this case was the *export_to_gitsbe*, because these Gitsbe output models are used as input for the Drabme module.

The following options were defined to configure the genetic algorithm used to generate and optimise the ensemble of Boolean models.

- *simulations*: The number of simulations was set to 50.
- *generations*: The maximal number of generations per evolution was set to 20. The number of generations is less if the target fitness threshold is reached.
- *population*: The number of models per generation was set to 20.
- *crossover*: The number of crossovers was set to 1. This number indicates the number of splitting points used when splitting and matching features from the parent models during the crossover phase.
- *selection*: This option was set to 3, meaning that three models are selected from each generation.
- Different types of mutations can be introduced during the mutation phase. In this case 3 *balance_mutations* were introduced during each mutation phase.
- *target_fitness*: The fitness target threshold is set to 0.99, just below the absolute maximum of 1. A fitness above 0.99 will halt the generation.
- *bootstrap_mutations_factor*: This option is set to 1000, to boost the number of mutations introduced in the initial generation.
- *mutations_factor*: Unlike the bootstrap factor, this option is only set to 1, to reduce the number of mutations introduced after the initial generation.
- *models_saved*: 3 models are saved after each simulation. Given that the number of simulations is 50, this results in a total of 150 output models in each ensemble.
- *fitness_threshold*: In addition to the fitness target threshold, a lower fitness threshold for saving a model is defined. This threshold is set to 0.1, which is a limit usually being exceeded.

A.3 Drabme specific configurations

The Drabme configurations include two parameters.

max_drug_comb_size is related to the order of drug combinations tested. This option was set to 2, to limit the perturbation analyses to double drug combinations.

synergy_method parameter defined the synergy calculation method. This option was set to either *HSA* or *Bliss* depending on the synergy calculation method applied in the experimental synergy screen used to provide gold standard synergies.

Appendix B

Calculation of Determinative Power

The Determinative Power (DP) value of node j is the sum of the Mutual Information (MI) for all its output nodes [81].

$$DP(j) = \sum_{i=1}^{n} MI(f_i(X); (X_j) \tag{B.1}$$

MI is a measure of the information gained about the state of X = {X_1, X_2 ..., X_n} given the knowledge about the state of X_j [62]. The expression *$f_i(X)$* represents the logical function of node i. The DP of node j is the sum of the MI for all its output nodes [81]. The Shannon entropy H(X) is applied to calculate MI. In the binary case, such as for Boolean modelling, the Shannon entropy is calculated as follows

$$h(p) = -plog_2(p) - (1-p)log_2(1-p) \tag{B.2}$$

Implementing the Shannon entropy equation in calculation of MI we get

$$MI(f_i(X); (X_j) = H(f_i(X)) - H(f_i(X)|(X_j) \tag{B.3}$$

$$
\begin{aligned}
&H(f_i(X)) = h\left(\sum_{x\epsilon suppf_i} p_x\right),\\
&H(f_i(X)|(X_j) = \sum_{x\epsilon suppf_i} P(X_j = x_j)h\left(\sum_{x\epsilon suppf_i} P(X = x|X_j = xj)\right)\\
&= P(X_j = 1)h\left(\sum_{x\epsilon suppf_i} P(X = x|X_j = 1)\right) + P(X_j = 0)h\left(\sum_{x\epsilon suppf_i} P(X = x|X_j = 0)\right),\\
&MI(f_i(X);(X_j) = h\left(\sum_{x\epsilon suppf_i} p_x\right)\\
&- P(X_j = 1)h\left(\sum_{x\epsilon suppf_i} P(X = x|X_j = 1)\right) + P(X_j = 0)h\left(\sum_{x\epsilon suppf_i} P(X = x|X_j = 0)\right)
\end{aligned}
\tag{B.4}
$$

We assume that there is an equal probability of X being 1 and 0 [62]. Hence, $P(X_i = 1) = P(X_i = 0) = 1/2$.

Example: Consider a 4-node network and the following logical rules:

Logical rule of node 1:$f_1(x_2, x_3, x_4) = x_2$ AND x_3 AND NOT x_4
Logical rule of node 2:$f_2(x_1, x_2, x_3) = x_1$ AND (x_2 OR x_3)
Logical rule of node 3:$f_3(x_1, x_2) = x_1$ OR x_2

Node x_4 is an input and has no logical rule. Given the logical rules, the following input states will give an active node:

Node 1 activity : $suppf_1(x_2, x_3, x_4) = (1, 1, 0)$
Node 2 activity : $suppf_2(x_1, x_2, x_3) = (1, 0, 1), (1, 1, 0), (1, 1, 1)$
Node 3 activity : $suppf_3(x_1, x_2) = (0, 1), (1, 0), (1, 1)$

To calculate the DP value of node 1 we need to solve the following equation adding the MI for the logical rules dependent on X_1, which are f_2 and f_3.

$$
\begin{aligned}
&DP(1) = MI(f_2; X_1) + MI(f_3; X_1)\\
&MI(f_2; X_1) = h\left(\sum_{x\epsilon suppf_2} p_x\right)\\
&- P(X_1 = 1)h\left(\sum_{x\epsilon suppf_2} P(X = x|X_1 = 1)\right) + P(X_1 = 0)h\left(\sum_{x\epsilon suppf_2} P(X = x|X_1 = 0)\right)
\end{aligned}
$$

We see that

$$\sum_{x \epsilon suppf_2} p_x = 3/8$$

if we sum up all the possible states that result in the activity of node 2. And since all elements of $suppf_2$ have $X_1 = 1$, it follows that

$$\sum_{x \epsilon suppf_2} P(X = x | X_1 = 0) = 0$$

and

$$\begin{aligned}\sum_{x \epsilon suppf_2} P(X = x | X_1 = 1) &= \sum_{x \epsilon suppf_2} \frac{P(X = x, X_1 = 1)}{P(X_1 = 1)} \\ &= \frac{P(1,0,1)}{1/2} + \frac{P(1,1,0)}{1/2} + \frac{P(1,1,1)}{1/2} \\ &= \frac{1/8}{1/2} + \frac{1/8}{1/2} + \frac{1/8}{1/2} = \frac{3/8}{1/2} = 3/4.\end{aligned}$$

Then

$$\begin{aligned}MI(f_2(X); X_1 &= h(3/8) - \frac{1}{2}h(3/4) \\ &= \left(-\frac{3}{8}log_2(\frac{3}{8}) - (1 - \frac{3}{8})log_2(1 - \frac{3}{8})\right) - \frac{1}{2}\left(-\frac{3}{4}log_2(\frac{3}{4}) - (1 - \frac{3}{4})log_2(1 - \frac{3}{4})\right) \\ &= 0.5488.\end{aligned}$$

Similarly,

$$MI(f_3(X); X_1) = h(3/4) - \frac{1}{2}h(1) + \frac{1}{2}h(1/2) = 0.3113.$$

Given these calculations, the DP value of node X_1 is 0.8601.

Appendix C

Cell Line Specific Baseline Activity Profiles

Cell line specific baseline activity profiles are provided in the following tables.

Table C.1. AGS baseline activity for all nodes included in CASCADE 1.0, retrieved from Niederdorfer et al. [56]

Model: CASCADE 1.0		
Node	**AGS**	**Activity inference tool**
AKT_f	1	literature
BAX	0	literature
BCL2	1	literature
CASP3	0	literature
CASP8	0	literature
CCND1	1	literature
CTNNB1	1	literature
ERK_f	1	literature
GSK3_f	0	literature
JNK_f	0	literature
KRAS	1	literature
MAPK14	0	literature
MMP_f	1	literature
MYC	1	literature
NFKB_f	1	literature
PIK3CA	1	literature
PTEN	0	literature
RAC_f	1	literature
S6K_f	1	literature
TCF7_f	1	literature

TP53	0	literature
MAP3K7	0	PARADIGM
IKBKB	1	PARADIGM
FOXO_f	1	PARADIGM
TSC_f	1	PARADIGM
GAB_f	1	PARADIGM
FZD_f	1	PARADIGM
BAD	0	PARADIGM
CFLAR	0	PARADIGM
CYCS	0	PARADIGM
EGR1	1	PARADIGM
LEF	1	PARADIGM
SFRP1	0	PARADIGM
SHC1	1	PARADIGM
TAB_f	1	PARADIGM
PDPK1	0	PARADIGM
RSK_f	1	PARADIGM
GRB2	0	PARADIGM
mTORC1_c	0	PARADIGM
mTORC2_c	0	PARADIGM
NLK	0	PARADIGM
mTORC1_c	0	PARADIGM
MEK_f	1	PARADIGM
CHUK	1	PARADIGM
MSK_f	1	PARADIGM
GRAP2	0	PARADIGM
VDL_f	1	PARADIGM
BTRC	1	PARADIGM
CASP9	0	PARADIGM
DUSP6	1	PARADIGM
ITCH	1	PARADIGM
MAP3K5	0	PARADIGM
MDM2	1	PARADIGM
PTPN11	1	PARADIGM
RTPK_f	1	PARADIGM
SOS1	1	PARADIGM
DUSP1	1	PARADIGM
MAP2K4	0	PARADIGM
RHEB	0	PARADIGM
AKT1S1	0	PARADIGM

AXIN1	1	PARADIGM
CK1_f	1	PARADIGM
IRS1	0	PARADIGM
MAP2K3	0	PARADIGM
MAP2K7	0	PARADIGM
MAP3K11	0	PARADIGM
MAP3K4	0	PARADIGM
MAP3K8	0	PARADIGM
RAF_f	1	PARADIGM
DKK_f	1	PARADIGM
RTPK_g	NA	-
MDM2_g	NA	-
PTEN_g	NA	-
SFRP1_g	NA	-
DKK_g	NA	-

Table C.2. Baseline activity for all nodes included in the Lu-model, inferred for the COLO_205, HCT_116, SW_48 and SW_620 cell lines. Normalised transcription values and corresponding binary values are provided.

Model: Lu									
Node	**COLO205**		**HCT116**		**SW48**		**SW620**		**Activity inference tool**
	Norm	Bin	Norm	Bin	Norm	Bin	Norm	Bin	
AKT	0.029	0	0.443	0	0.810	1	0.604	1	PROFILE
APC	0.500	0.5	0.500	0.5	0.500	0.5	0.500	0.5	PROFILE
ASK1	0.846	1	0.723	1	0.771	1	0.500	0.5	PROFILE
ATM	0.620	1	0.620	1	0.566	1	0.732	1	PROFILE
BAX	0.385	0	0.323	0	0.500	0.5	0.445	0	PROFILE
BCATENIN	0.414	0	0.323	0	0.248	0	0.307	0	PROFILE
BCL2	0.000	0	0.000	0	0.467	0	0.000	0	PROFILE
CASP3	0.849	1	0.122	0	0.332	0	0.390	0	PROFILE
CASP8	0.936	1	0.598	1	0.144	0	0.385	0	PROFILE
CASP9	0.780	1	0.677	1	0.500	0.5	0.677	1	PROFILE
CERAMIDE	NA	NA	NA	NA	NA	NA	NA	NA	PROFILE
CFLIP	0.780	1	0.500	0.5	0.500	0.5	0.323	0	PROFILE
CYCLIND1	0.252	0	0.615	1	0.648	1	0.638	1	PROFILE
CYCT	0.688	1	0.426	0	0.407	0	0.683	1	PROFILE
ERK	0.269	0	0.500	0.5	0.223	0	0.457	0	PROFILE
FOS	0.109	0	0.422	0	0.750	1	0.582	1	PROFILE

GP130	0.365	0	0.500	0.5	0.323	0	0.276	0	PROFILE
GSK3B	0.754	1	0.553	1	0.722	1	0.263	0	PROFILE
IAP	0.914	1	0.694	1	0.500	0.5	0.835	1	PROFILE
IKB	0.323	0	0.323	0	0.323	0	0.763	1	PROFILE
IKK	0.770	1	0.952	1	0.323	0	0.930	1	PROFILE
IL6	NA	NA	NA	NA	NA	NA	NA	NA	PROFILE
JAK	0.944	1	0.814	1	0.541	1	0.844	1	PROFILE
JNK	0.640	1	0.856	1	0.640	1	0.809	1	PROFILE
JUN	0.500	0.5	0.464	0	0.392	0	0.794	1	PROFILE
MDM2	0.209	0	0.683	1	0.500	0.5	0.268	0	PROFILE
MEK	0.841	1	0.323	0	0.458	0	0.705	1	PROFILE
MEKK1	0.857	1	0.418	0	0.323	0	0.570	1	PROFILE
MOMP	NA	NA	NA	NA	NA	NA	NA	NA	PROFILE
NFKB	0.313	0	0.313	0	0.245	0	0.245	0	PROFILE
P21	0.355	0	0.689	1	0.733	1	0.127	0	PROFILE
P53	0.791	1	0.651	1	0.457	0	0.709	1	PROFILE
PI3K	0.794	1	0.794	1	0.794	1	0.677	1	PROFILE
PP2A	0.885	1	0.646	1	0.180	0	0.459	0	PROFILE
PTEN	0.766	1	0.730	1	0.821	1	0.730	1	PROFILE
RAF	0.064	0	0.239	0	0.166	0	0.323	0	PROFILE
ROS	NA	NA	NA	NA	NA	NA	NA	NA	PROFILE
S1P	0.810	1	0.926	1	0.164	0	0.654	1	PROFILE
SMAC	1.000	1	NA	NA	0.000	0	NA	NA	PROFILE
SMAD	0.677	1	0.780	1	0.780	1	0.780	1	PROFILE
SMAD7	0.500	0.5	0.285	0	0.887	1	0.406	0	PROFILE
SMASE	0.629	1	0.139	0	0.072	0	0.343	0	PROFILE
SOCS	0.000	0	0.000	0	0.000	0	0.000	0	PROFILE
SOD	0.196	0	0.323	0	0.307	0	0.111	0	PROFILE
SPHK1	0.000	0	0.000	0	0.987	1	0.000	0	PROFILE
STAT3	0.597	1	0.639	1	0.076	0	0.161	0	PROFILE
TBID	0.641	1	0.376	0	0.553	1	0.553	1	PROFILE
TGFR	NA	NA	NA	NA	NA	NA	NA	NA	PROFILE

Table C.3. Baseline activity for all nodes included in the Park-model, inferred for the COLO_205, HCT_116, SW_48 and SW_620 cell lines. Normalised transcription values (inferred with PROFILE) and corresponding binary values are provided.

Model: Park									
Node	**COLO205**		**HCT116**		**SW48**		**SW620**		**Activity inference tool**
	Norm	Bin	Norm	Bin	Norm	Bin	Norm	Bin	
Akt	0.024	0	0.500	0.5	0.871	1	0.677	1	PARADIGM
AMPK	0.000	0	0.443	0	0.000	0	0.722	1	PARADIGM
AP1	0.399	0	0.342	0	0.242	0	0.864	1	PARADIGM
APAF1	0.161	0	0.323	0	0.161	0	0.056	0	PARADIGM
ATF2	0.596	1	0.677	1	0.102	0	0.500	0.5	PARADIGM
ATM	0.809	1	0.809	1	0.740	1	0.914	1	PARADIGM
AXIN	0.096	0	0.052	0	0.759	1	0.833	1	PARADIGM
Bax	0.500	0.5	0.414	0	0.644	1	0.577	1	PARADIGM
Bcl2	0.000	0	0.000	0	1.000	1	0.000	0	PARADIGM
betacatenin	0.591	1	0.449	0	0.323	0	0.422	0	PARADIGM
BRaf	0.500	0.5	0.826	1	0.826	1	0.876	1	PARADIGM
BRCA1	0.388	0	0.388	0	0.076	0	0.388	0	PARADIGM
c_Myc	0.158	0	0.689	1	0.599	1	0.966	1	PARADIGM
CASP3	0.805	1	0.165	0	0.360	0	0.409	0	PARADIGM
CASP9	0.780	1	0.677	1	0.500	0.5	0.677	1	PARADIGM
Cdc25	0.010	0	0.260	0	0.056	0	0.144	0	PARADIGM
CHK1	NA	NA	NA	NA	NA	NA	NA	NA	PARADIGM
CHK2	0.118	0	0.570	1	0.570	1	0.323	0	PARADIGM
CRaf	0.104	0	0.323	0	0.238	0	0.412	0	PARADIGM
CREB	0.652	1	0.652	1	0.323	0	0.500	0.5	PARADIGM
CyclinA	NA	NA	NA	NA	NA	NA	NA	NA	PARADIGM
CyclinB	0.050	0	0.241	0	0.050	0	0.323	0	PARADIGM
CyclinD	0.269	0	0.672	1	0.705	1	0.696	1	PARADIGM
CyclinE	0.010	0	0.598	1	0.677	1	0.010	0	PARADIGM
CyclinG	0.098	0	0.533	1	0.591	1	0.289	0	PARADIGM
CytC	0.714	1	0.482	0	0.464	0	0.710	1	PARADIGM
E2F1	0.038	0	0.058	0	0.323	0	0.577	1	PARADIGM
EGFR	0.268	0	0.529	1	0.899	1	0.026	0	PARADIGM
ELK1	0.500	0.5	0.643	1	0.600	1	0.850	1	PARADIGM
ERK	0.384	0	0.645	1	0.323	0	0.601	1	PARADIGM
FOXO3	0.500	0.5	0.599	1	0.442	0	0.442	0	PARADIGM
GAB1	0.220	0	0.500	0.5	0.500	0.5	0.220	0	PARADIGM
GADD45	0.430	0	0.836	1	0.572	1	0.847	1	PARADIGM
Grb2	0.901	1	0.837	1	0.465	0	0.762	1	PARADIGM

GSK3beta	0.753	1	0.553	1	0.722	1	0.263	0	PARADIGM
IGFR	0.892	1	0.220	0	0.628	1	0.628	1	PARADIGM
IRS	0.101	0	0.851	1	0.863	1	0.379	0	PARADIGM
JAK	0.718	1	0.628	1	0.718	1	0.323	0	PARADIGM
JNK	0.500	0.5	0.826	1	0.500	0.5	0.753	1	PARADIGM
MDM2	0.323	0	0.870	1	0.718	1	0.417	0	PARADIGM
MDMX	0.652	1	0.986	1	0.323	0	0.500	0.5	PARADIGM
MEK	1.000	1	0.106	0	0.712	1	0.998	1	PARADIGM
MEKK1	0.979	1	0.500	0.5	0.323	0	0.753	1	PARADIGM
MEKK2	0.966	1	0.770	1	0.655	1	0.500	0.5	PARADIGM
MEKK3	0.500	0.5	0.780	1	0.500	0.5	0.780	1	PARADIGM
MEKK4	0.011	0	0.763	1	0.500	0.5	0.161	0	PARADIGM
MK2	0.314	0	0.352	0	0.566	1	0.428	0	PARADIGM
MKK3_6	0.285	0	0.285	0	0.661	1	0.638	1	PARADIGM
MKK4	0.597	1	0.677	1	0.597	1	0.597	1	PARADIGM
MKK7	0.677	1	0.744	1	0.596	1	0.839	1	PARADIGM
MKPs	NA	NA	NA	NA	NA	NA	NA	NA	PARADIGM
MLKs	NA	NA	NA	NA	NA	NA	NA	NA	PARADIGM
MSK	NA	NA	NA	NA	NA	NA	NA	NA	PARADIGM
mTOR1	0.775	1	0.500	0.5	0.323	0	0.854	1	PARADIGM
mTOR2	0.775	1	0.500	0.5	0.323	0	0.854	1	PARADIGM
p120RasGAP	0.954	1	0.388	0	0.446	0	0.500	0.5	PARADIGM
p14ARF	1.000	1	1.000	1	0.000	0	1.000	1	PARADIGM
p15	0.981	1	0.856	1	0.691	1	1.000	1	PARADIGM
p21	0.432	0	0.840	1	0.877	1	0.106	0	PARADIGM
p27	0.967	1	0.000	0	0.000	0	0.000	0	PARADIGM
p38	0.238	0	0.164	0	0.323	0	0.581	1	PARADIGM
p53	0.820	1	0.500	0.5	0.153	0	0.640	1	PARADIGM
p90RSK	0.113	0	0.157	0	0.542	1	0.255	0	PARADIGM
PDK1	0.323	0	0.323	0	0.500	0.5	0.628	1	PARADIGM
PI3K	0.794	1	0.794	1	0.794	1	0.677	1	PARADIGM
PIP3	NA	NA	NA	NA	NA	NA	NA	NA	PARADIGM
PP2A	0.863	1	0.577	1	0.125	0	0.376	0	PARADIGM
PTEN	0.700	1	0.644	1	0.786	1	0.644	1	PARADIGM
Ras	0.323	0	0.600	1	0.600	1	0.834	1	PARADIGM
Rb	0.973	1	0.500	0.5	0.101	0	0.101	0	PARADIGM
S6K	0.500	0.5	0.982	1	0.655	1	0.847	1	PARADIGM
Shc	0.893	1	0.927	1	0.295	0	0.753	1	PARADIGM
SHP2	0.201	0	0.932	1	0.432	0	0.724	1	PARADIGM
SMAC	1.000	1	NA	NA	0.000	0	NA	NA	PARADIGM

Smad2_3	0.260	0	0.788	1	0.500	0.5	0.260	0	PARADIGM
Smad2_3_4	0.718	1	0.591	1	0.591	1	0.718	1	PARADIGM
Smad7	0.357	0	0.169	0	0.842	1	0.268	0	PARADIGM
Sos	0.278	0	0.500	0.5	0.677	1	0.500	0.5	PARADIGM
SPRY	0.500	0.5	0.091	0	0.375	0	0.718	1	PARADIGM
Src	0.902	1	0.241	0	0.454	0	0.241	0	PARADIGM
STAT	0.433	0	0.740	1	0.323	0	0.500	0.5	PARADIGM
TAK1	0.174	0	0.794	1	0.500	0.5	0.794	1	PARADIGM
TAO	0.743	1	0.677	1	0.596	1	0.393	0	PARADIGM
TGFR	0.825	1	0.752	1	0.417	0	0.500	0.5	PARADIGM
TSC1_2	0.677	1	0.500	0.5	0.500	0.5	0.270	0	PARADIGM
Wip1	0.677	1	0.937	1	0.500	0.5	0.677	1	PARADIGM
XIAP	0.808	1	0.549	1	0.386	0	0.699	1	PARADIGM

Appendix D

Cell Line Specific Gold Standard Synergies

All cell line specific gold standard synergies are listed in table D.1.

Table D.1. Overview of all experimentally verified drug synergies observed in AGS, COLO_205, HCT_116, SW_48, and SW_620. Abbreviations used as drug identifiers in the pipeline input files are listed.

Model: CASCADE 1.0 Cell line: AGS					
Drug A	**Abbrev.**	**Target A**	**Drug B**	**Abbrev.**	**Target B**
PI103	PI	PIK3CA	(5Z)-7-oxozeaenol	5Z	MAP3K7
PD0325901	PD	MEK	PI103	PI	PIK3CA
AKTi-1,2	AK	AKT	(5Z)-7-oxozeaenol	5Z	MAP3K7
AKTi-1,2	AK	AKT	PD0325901	PD	MEK
Model: Park Cell line: COLO_205					
Drug A	**Abbrev.**	**Target A**	**Drug B**	**Abbrev.**	**Target B**
Navitoclax	NA	Bcl_2	Afatinib	AF	EGFR
Navitoclax	NA	Bcl_2	MK-2206	MK	Akt
Navitoclax	NA	Bcl_2	Taselisib	TA	PI3K
Trametinib	TR	MEK	Taselisib	TA	PI3K
Trametinib	TR	MEK	Saptinib	SA	EGFR
Dabrafenib	DA	BRaf	Saptinib	SA	EGFR
Dabrafenib	DA	BRaf	Taselisib	TA	PI3K
Linsitinib	LI	IGFR	AZD7762	AZ62	CHK1, CHK2

Linsitinib	LI	IGFR	Saptinib	SA	EGFR
Taselisib	TA	PI3K	SB216763	SB21	GSK3beta
Taselisib	TA	PI3K	AZD7762	AZ62	CHK1, CHK2
SCH772984	SC	ERK	Taselisib	TA	PI3K
Model: Park Cell line: HCT_116					
Drug A	**Abbrev.**	**Target A**	**Drug B**	**Abbrev.**	**Target B**
Navitoclax	NA	Bcl_2	AZD7762	AZ62	CHK1, CHK2
Navitoclax	NA	Bcl_2	Nutlin-3a(-)	NU	MDM2
Navitoclax	NA	Bcl_2	BMS-754807	BM	IGFR
MK-2206	MK	Akt	AZD7762	AZ62	CHK1, CHK2
MK-2206	MK	Akt	Dabrafenib	DA	BRaf
AZD8055	AZ55	mTOR1, mTOR2	Linsitinib	LI	IGFR
AZD8055	AZ55	mTOR1, mTOR2	Taselisib	TA	PI3K
Trametinib	TR	MEK	AZD7762	AZ62	CHK1, CHK2
Trametinib	TR	MEK	MK-2206	MK	Akt
Trametinib	TR	MEK	Dabrafenib	DA	BRaf
Trametinib	TR	MEK	Taselisib	TA	PI3K
Trametinib	TR	MEK	Saptinib	SA	EGFR
Dabrafenib	DA	BRaf	AZD7762	AZ62	CHK1, CHK2
Dabrafenib	DA	BRaf	Linsitinib	LI	IGFR
Dabrafenib	DA	BRaf	Taselisib	TA	PI3K
Linsitinib	LI	IGFR	AZD7762	AZ62	CHK1, CHK2
Linsitinib	LI	IGFR	MK-2206	MK	Akt
Taselisib	TA	PI3K	SCH772984	SC	ERK
SCH772984	SC	ERK	Navitoclax	NA	Bcl_2
SCH772984	SC	ERK	MK-2206	MK	Akt
SCH772984	SC	ERK	Dabrafenib	DA	BRaf
SCH772984	SC	ERK	Linsitinib	LI	IGFR
SCH772984	SC	ERK	Saptinib	SA	EGFR

BMS-754807	BM	IGFR	Trametinib	TR	MEK
BMS-754807	BM	IGFR	Saptinib	SA	EGFR
Model: Park Cell line: SW_48					
Drug A	**Abbrev.**	**Target A**	**Drug B**	**Abbrev.**	**Target B**
Afatinib	AF	EGFR	Trametinib	TR	MEK
AZD7762	AZ62	CHK1, CHK2	Afatinib	AF	EGFR
BMS-754807	BM	IGFR	MK-2206	MK	Akt
BMS-754807	BM	IGFR	Trametinib	TR	MEK
MK-2206	MK	Akt	SCH772984	SC	ERK
Navitoclax	NA	Bcl_2	Afatinib	AF	EGFR
Navitoclax	NA	Bcl_2	Linsitinib	LI	IGFR
Navitoclax	NA	Bcl_2	MK-2206	MK	Akt
Navitoclax	NA	Bcl_2	Saptinib	SA	EGFR
Navitoclax	NA	Bcl_2	SB216763	SB21	GSK3beta
Navitoclax	NA	Bcl_2	SB505124	SB50	TGFR
Navitoclax	NA	Bcl_2	SCH772984	SC	ERK
Navitoclax	NA	Bcl_2	Taselisib	TA	PI3K
Nutlin-3a(-)	NU	MDM2	MK-2206	MK	Akt
Nutlin-3a(-)	NU	MDM2	Taselisib	TA	PI3K
Saptinib	SA	EGFR	Trametinib	TR	MEK
SCH772984	SC	ERK	Afatinib	AF	EGFR
SCH772984	SC	ERK	Saptinib	SA	EGFR
Taselisib	TA	PI3K	SCH772984	SC	ERK
Trametinib	TR	MEK	Saptinib	SA	EGFR
Trametinib	TR	MEK	SB216763	SB21	GSK3beta
Trametinib	TR	MEK	Taselisib	TA	PI3K
Model: Park Cell line: SW_620					
Drug A	**Abbrev.**	**Target A**	**Drug B**	**Abbrev.**	**Target B**
AZD8055	AZ55	mTOR1, mTOR2	MK-2206	MK	Akt
Dabrafenib	DA	BRaf	Taselisib	TA	PI3K
Linsitinib	LI	IGFR	AZD8055	AZ55	mTOR1, mTOR2

MK-2206	MK	Akt	Afatinib	AF	EGFR
MK-2206	MK	Akt	Saptinib	SA	EGFR
MK-2206	MK	Akt	SB216763	SB21	GSK3beta
MK-2206	MK	Akt	SB505124	SB50	TGFR
Trametinib	TR	MEK	SCH772984	SC	ERK
Model: Lu et al. Cell line: COLO_205					
Drug A	**Abbrev.**	**Target A**	**Drug B**	**Abbrev.**	**Target B**
Navitoclax	NA	BCL2	MK-2206	MK	AKT
Navitoclax	NA	BCL2	Taselisib	TA	PI3K
Trametinib	TR	MEK	Taselisib	TA	PI3K
Taselisib	TA	PI3K	SB216763	SB	GSK3B
SCH772984	SC	ERK	Taselisib	TA	PI3K
Model: Lu Cell line: HCT_116					
Drug A	**Abbrev.**	**Target A**	**Drug B**	**Abbrev.**	**Target B**
Crizotinib	CR	ROS	Navitoclax	NA	BCL2
Navitoclax	NA	BCL2	Nutlin-3a(-)	NU	MDM2
SCH772984	SC	ERK	MK-2206	MK	AKT
SCH772984	SC	ERK	Navitoclax	NA	BCL2
SCH772984	SC	ERK	Taselisib	TA	PI3K
Taselisib	TA	PI3K	Trametinib	TR	MEK
Trametinib	TR	MEK	MK-2206	MK	AKT
Trametinib	TR	MEK	Taselisib	TA	PI3K
Model: Lu Cell line: SW_48					
Drug A	**Abbrev.**	**Target A**	**Drug B**	**Abbrev.**	**Target B**
Crizotinib	CR	ROS	SCH772984	SC	ERK
MK-2206	MK	AKT	SCH772984	SC	ERK
Navitoclax	NA	BCL2	MK-2206	MK	AKT
Navitoclax	NA	BCL2	SB216763	SB	GSK3B
Navitoclax	NA	BCL2	SCH772984	SC	ERK
Navitoclax	NA	BCL2	Taselisib	TA	PI3K
Nutlin-3a(-)	NU	MDM2	MK-2206	MK	AKT
Nutlin-3a(-)	NU	MDM2	Taselisib	TA	PI3K
Taselisib	TA	PI3K	SCH772984	SC	ERK
Taselisib	TA	PI3K	Trametinib	TR	MEK
Trametinib	TR	MEK	SB216763	SB	GSK3B
Model: Lu Cell line: SW_620					

Drug A	**Abbrev.**	**Target A**	**Drug B**	**Abbrev.**	**Target B**
Navitoclax	NA	BCL2	Trametinib	TR	MEK
Navitoclax	NA	BCL2	Taselisib	TA	PI3K
Navitoclax	NA	BCL2	SCH772984	SC	ERK
Crizotinib	CR	ROS	Trametinib	TR	MEK
Trametinib	TR	MEK	Taselisib	TA	PI3K

Appendix E

Degree Z-score and DP Calculations

Table E.1. Degree Z-score calculated for all nodes in CASCADE 1.0, Park-model and Lu-model

Degree Z-score					
CASCADE 1.0		Park-model		Lu-model	
Node	Score	Node	Score	Node	Score
ERK_f	3.956	Akt	3.302	P53	2.950
AKT_f	3.523	ERK	3.092	NFKB	1.960
MAPK14	3.090	PP2A	2.883	AKT	1.960
GSK3_f	2.656	p53	2.673	P21	1.960
LRP_f	1.790	GSK3beta	2.044	CASP3	1.465
RSK_f	1.356	c_Myc	2.044	JUN	1.465
TSC_f	1.356	p38	1.625	GSK3B	0.970
IKBKB	0.923	JNK	1.625	MOMP	0.970
MAP2K4	0.923	Bax	1.416	CERAMIDE	0.970
MAP3K7	0.923	E2F1	1.416	STAT3	0.970
S6K_f	0.923	MDM2	1.416	BCL2	0.970
TCF7_f	0.923	Src	1.206	PTEN	0.475
JNK_f	0.490	ATM	0.997	MDM2	0.475
MEK_f	0.490	Bcl_2	0.997	IAP	0.475
mTORC1_c	0.490	AP_1	0.997	PP2A	0.475
PDPK1	0.490	CyclinE	0.787	CYCLIND1	0.475
RAF_f	0.490	FOXO3	0.787	BAX	0.475
RTPK_f	0.490	MKK4	0.577	ERK	-0.020
TP53	0.490	CyclinD	0.577	ROS	-0.020
BTRC	0.056	S6K	0.368	CASP8	-0.020
CTNNB1	0.056	EGFR	0.368	SMAD	-0.020
DUSP1	0.056	CyclinA	0.368	JNK	-0.020
FOXO_f	0.056	p90RSK	0.368	CASP9	-0.020

GAB_f	0.056	p27	0.368	TBID	-0.020
IRS1	0.056	Smad2_3	0.158	SPHK1	-0.515
KRAS	0.056	Ras	0.158	IKK	-0.515
MDM2	0.056	IGFR	0.158	JAK	-0.515
MSK_f	0.056	MKPs	0.158	MEK	-0.515
mTORC2_c	0.056	PI3K	0.158	SMAD7	-0.515
MYC	0.056	Rb	0.158	SOD	-0.515
NFKB_f	0.056	p21	0.158	TGFR	-0.515
PIK3CA	0.056	MKK3_6	0.158	ASK1	-0.515
PTEN	0.056	beta_catenin	-0.051	MEKK1	-0.515
RAC_f	0.056	ATM	-0.515	TSC1_2	-0.051
BAD	-0.377	Smad2_3_4	-0.051	BCATENIN	-0.515
CASP3	-0.377	Shc	-0.051	IKB	-1.010
CCND1	-0.377	p14ARF	-0.051	IL6	-1.010
CFLAR	-0.377	MDMX	-0.051	SMAC	-1.010
CHUK	-0.377	MKK7	-0.051	CFLIP	-1.010
CYCS	-0.377	CREB	-0.051	GP130	-1.010
DKK_g	-0.377	GAB1	-0.261	RAF	-1.010
DUSP6	-0.377	mTOR1	-0.261	S1P	-1.010
DVL_f	-0.377	PTEN	-0.261	SMASE	-1.010
FZD_f	-0.377	Wip1	-0.261	SOCS	-1.010
GRAP2	-0.377	Grb2	-0.261	CYTC	-1.010
GRB2	-0.377	CyclinB	-0.261	PI3K	-1.010
MAP2K3	-0.377	TAK1	-0.261	FOS	-1.010
MAP2K7	-0.377	Cdc25	-0.261		
MDM2_g	-0.377	IRS	-0.261		
NLK	-0.377	XIAP	-0.470		
RHEB	-0.377	TGFR	-0.470		
SHC1	-0.377	BRCA1	-0.470		
SOS1	-0.377	CASP9	-0.470		
AKT1S1	-0.810	Sos	-0.470		
AXIN1	-0.810	MEK	-0.470		
BAX	-0.810	CHK2	-0.470		
BCL2	-0.810	BRaf	-0.470		
CASP8	-0.810	CRaf	-0.470		
CASP9	-0.810	MLKs	-0.470		
CK1_f	-0.810	MEKK1	-0.470		
DKK_f	-0.810	GADD45	-0.680		
EGR1	-0.810	SHP2	-0.680		
ITCH	-0.810	p120RasGAP	-0.680		

LEF	-0.810	mTOR2	-0.680		
MAP3K11	-0.810	MK2	-0.680		
MAP3K4	-0.810	CHK1	-0.680		
MAP3K5	-0.810	STAT	-0.680		
MAP3K8	-0.810	APAF1	-0.680		
MMP_f	-0.810	TAO	-0.680		
PTEN_g	-0.810	MEKK2	-0.680		
PTPN11	-0.810	MEKK4	-0.680		
RTPK_g	-0.810	MEKK3	-0.680		
SFRP1	-0.810	ATF2	-0.680		
SFRP1_g	-0.810	ELK1	-0.680		
TAB_f	-0.810	CASP3	-0.889		
		PIP3	-0.889		
		SMAC	-0.889		
		SPRY	-0.889		
		Smad7	-0.889		
		PDK1	-0.889		
		CytC	-0.889		
		p15	-0.889		
		CyclinG	-0.889		
		MSK	-0.889		
		JAK	-1.099		
		AXIN	-1.099		
		AMPK	-1.099		
		Rac1	-1.309		

Table E.2. DP calculated for all nodes in CASCADE 1.0, Park-model and Lu-model

Determinative Power					
CASCADE 1.0		Park-model		Lu-model	
Node	Score	Node	Score	Node	Score
AKT_f	4.059	ERK	3.794	NFKB	2.828
MAPK14	3.193	p53	3.754	GSK3B	2.220
TCF7_f	2.623	Akt	3.155	ERK	2.019
ERK_f	2.262	ATM	2.884	MOMP	2.000
LRP_f	2.008	GSK3beta	2.617	AKT	1.907
RAC_f	2.000	Smad2_3	2.311	CERAMIDE	1.634
MAP3K7	1.999	PP2A	2.245	ROS	1.623
IKBKB	1.690	p38	1.851	P53	1.460

TP53	1.623	Src	1.733	CASP3	1.422
MYC	1.623	S6K	1.448	STAT3	1.390
TSC_f	1.311	Bax	1.311	SPHK1	1.311
FOXO_f	1.311	Ras	1.239	BCL2	1.028
CTNNB1	1.311	GADD45	1.210	PTEN	1.011
GSK3_f	1.278	GAB1	1.139	IKB	1.000
GAB_f	1.138	IGFR	1.118	IKK	1.000
JNK_f	1.032	CyclinE	1.042	IL6	1.000
FZD_f	1.032	beta_catenin	1.001	JAK	1.000
SHC1	1.000	CASP3	1.000	MEK	1.000
CYCS	1.000	PIP3	1.000	SMAD7	1.000
BAD	1.000	TSC1_2	1.000	SOD	1.000
CFLAR	1.000	JNK	0.929	P21	0.826
DKK_g	1.000	CyclinA	0.826	MDM2	0.717
TAB_f	1.000	CyclinB	0.826	IAP	0.687
SFRP1	1.000	c_Myc	0.793	TGFR	0.623
EGR1	1.000	E2F1	0.750	PP2A	0.576
SFRP1_g	1.000	SHP2	0.668	SMAC	0.549
LEF	1.000	mTOR1	0.642	JUN	0.461
PDPK1	0.934	PTEN	0.575	CASP8	0.360
S6K_f	0.917	EGFR	0.552	SMAD	0.330
RSK_f	0.771	SMAC	0.549	ASK1	0.311
mTORC1_c	0.623	SPRY	0.549	CFLIP	0.311
mTORC2_c	0.623	XIAP	0.530	GP130	0.311
PTEN	0.623	Wip1	0.495	MEKK1	0.311
GRB2	0.623	Bcl_2	0.479	RAF	0.311
NLK	0.623	Smad2_3_4	0.441	S1P	0.311
MEK_f	0.530	MKPs	0.422	SMASE	0.311
MSK_f	0.449	Grb2	0.406	SOCS	0.311
CHUK	0.449	FOXO3	0.366	JNK	0.230
GRAP2	0.377	PI3K	0.360	CYTC	0.138
DVL_f	0.319	TGFR	0.358	PI3K	0.138
RTPK_f	0.311	Smad7	0.340	ATM	0.077
PIK3CA	0.311	BRCA1	0.311	CYCLIND1	0.066
MDM2	0.311	CASP9	0.311	FOS	0.066
BTRC	0.311	JAK	0.311	CASP9	0.049
NFKB_f	0.311	p120RasGAP	0.311	BCATENIN	0.030
CASP3	0.311	Sos	0.311	TBID	0.030
CCND1	0.311	MDM2	0.285	BAX	0.011
SOS1	0.311	PDK1	0.276		

DUSP6	0.311	AP_1	0.251		
MAP3K5	0.311	Shc	0.187		
PTPN11	0.311	p14ARF	0.169		
PTEN_g	0.311	CytC	0.157		
BAX	0.311	p90RSK	0.143		
BCL2	0.311	TAK1	0.139		
CASP9	0.311	Cdc25	0.139		
CASP8	0.311	MEK	0.138		
ITCH	0.311	mTOR2	0.138		
MAP2K4	0.276	AXIN	0.138		
DUSP1	0.276	MDMX	0.136		
KRAS	0.203	p15	0.128		
RHEB	0.203	MK2	0.114		
IRS1	0.138	Rb	0.101		
MAP2K7	0.138	p21	0.089		
MAP2K3	0.138	p27	0.089		
AKT1S1	0.138	MKK4	0.084		
AXIN1	0.138	CHK2	0.077		
CK1_f	0.138	CHK1	0.066		
MAP3K4	0.066	MKK7	0.066		
MAP3K11	0.066	CyclinD	0.061		
RAF_f	0.049	CyclinG	0.056		
MDM2_g	0.049	IRS	0.055		
MAP3K8	0.049	STAT	0.049		
DKK_f	0.032	CREB	0.032		
RTPK_g	0.019	APAF1	0.019		
MMP_f	0.019	BRaf	0.019		
		CRaf	0.019		
		MKK3_6	0.019		
		MSK	0.012		
		AMPK	0.004		
		MLKs	0.001		
		TAO	0.001		
		MEKK1	0.001		
		MEKK2	0.001		
		MEKK4	0.000		
		MEKK3	0.000		
		ATF2	0.000		
		ELK1	0.000		
		Rac1	0.000		

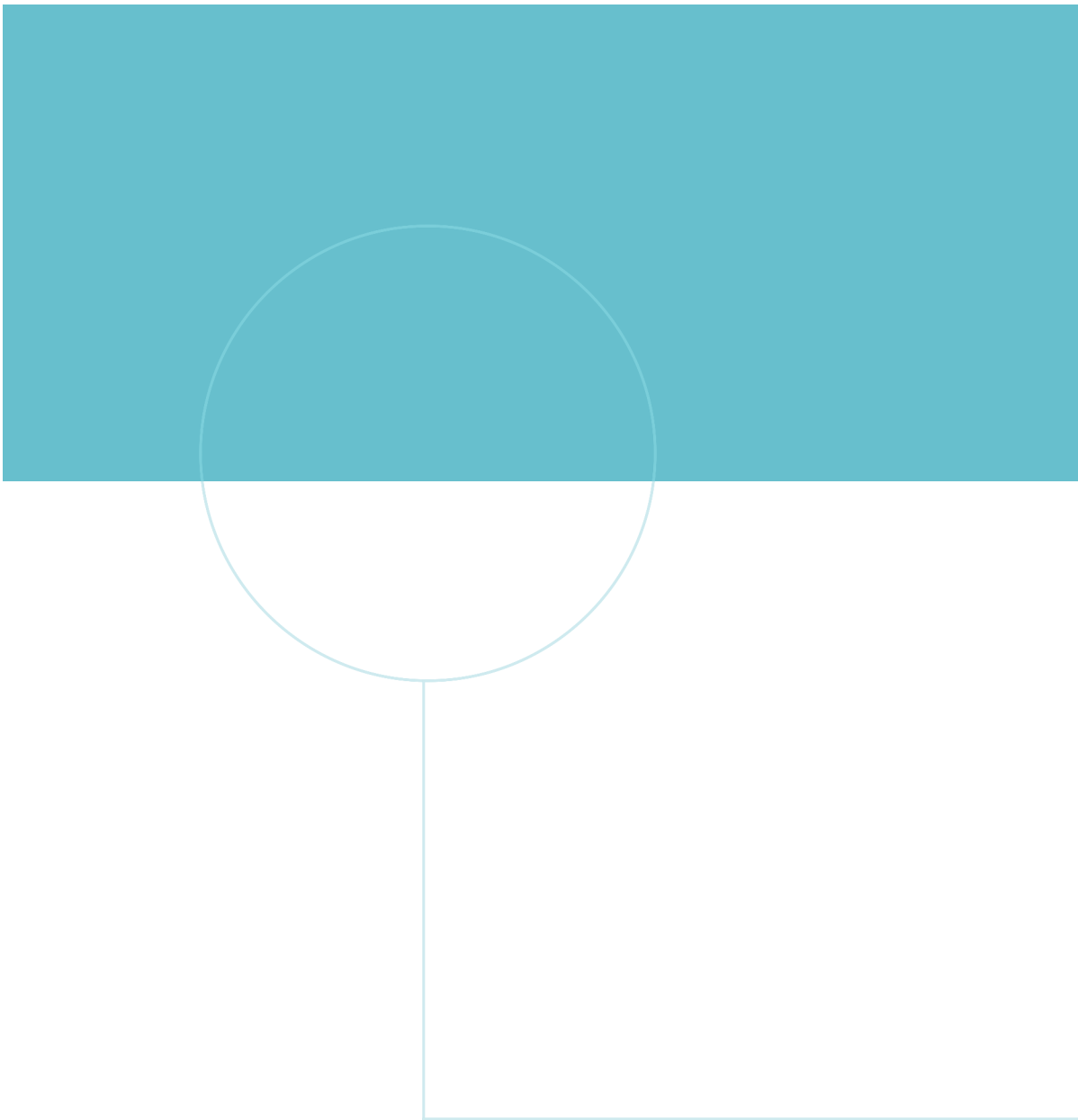

NTNU

Norwegian University of
Science and Technology